



HAL
open science

La génération d'impulsions courtes d'ondes acoustiques de surface sur un matériau piézo-électrique

Anurupa Shaw

► **To cite this version:**

Anurupa Shaw. La génération d'impulsions courtes d'ondes acoustiques de surface sur un matériau piézo-électrique. Other. Université Bourgogne Franche-Comté, 2017. English. NNT : 2017UBFCD063 . tel-01891128

HAL Id: tel-01891128

<https://theses.hal.science/tel-01891128v1>

Submitted on 9 Oct 2018

HAL is a multi-disciplinary open access archive for the deposit and dissemination of scientific research documents, whether they are published or not. The documents may come from teaching and research institutions in France or abroad, or from public or private research centers.

L'archive ouverte pluridisciplinaire **HAL**, est destinée au dépôt et à la diffusion de documents scientifiques de niveau recherche, publiés ou non, émanant des établissements d'enseignement et de recherche français ou étrangers, des laboratoires publics ou privés.

THESE DE DOCTORAT DE L'ETABLISSEMENT UNIVERSITE BOURGOGNE FRANCHE-COMTE
PREPAREE A UNIVERSITE DE FRANCHE-COMTE

Ecole doctorale n° 37

Sciences Pour l'Ingénieur et Microtechniques

Doctorat de Engineering Sciences and Microtechnologies

Par

Anurupa SHAW

Generation of short pulses of surface acoustic waves on a piezoelectric material

Le 14/12/2017

Unité de Recherche :
FEMTO-ST

Composition du Jury :

Bernard BONELLO	Directeur de recherche CNRS, HDR, Université Pierre et Marie Curie	Rapporteur
Omar ELMAZRIA	Professeur, Université de Lorraine	Rapporteur
Andreas MAYER	Professeur, Hochschule für Technik, Wirtschaft und Medien Offenburg	Examineur
Nico F. DECLERCQ	Professeur, Georgia Institute of Technology	Examineur
Franck CHOLLET	Professeur, Université de Franche-Comté	Président du jury
Vincent LAUDE	Directeur de recherche CNRS, HDR, Université de Franche-Comté	Directeur de thèse
Damien TEYSSIEUX	Maître de conférences, Université de Franche-Comté	Co-directeur de thèse

Acknowledgements

I offer my sincerest gratitude to my supervisors, Dr. Vincent Laude and Dr. Damien Teyssieux for accepting me as a student for this project and helping me through it. They have guided and supported me throughout my stay in France and have allowed me the room to work in my own way. I attribute the level of my doctoral degree to their encouragement and effort. Without their motivation this thesis would not have been possible. They have always shown faith in me and have provided me with a very friendly work environment. I would like to thank my committee members, Dr. Bernard Bonello, Dr. Omar Elmazria, Dr. Andreas Mayer, Dr. Franck Chollet and Dr. Nico Declercq for their reviews and their valuable comments and suggestions that helped me improve my work documented in this thesis.

I feel blessed to be a part of a prudent, talented, knowledgeable and supportive group of researchers at FEMTO-ST. I would like to thank Dr. Sarah Benchabane, Dr. Jean-Michel Friedt and the team of Phononics and Microscopy, MN2S, for enlightening discussions and suggestions, and Gilles Martin, Frank Lardet, and Valérie Soumann for their help with the experiments. I would also like to thank Dr. Marc Lamothe for providing the SAW device used as a reference sample in this project and Dr. Laurent Robert, David Raddenzati, Dr. Cyril Millon, Tristan Faure, and Marina Raschetti for their help during the fabrication process and SEM imaging of the SAW devices.

The staff of Femto-ST and école Doctorale (especially, Jocelyne Renaut, Alexandrine Vieillard, and Sandrine Pyon) have been very helpful and considerate throughout. I cannot thank them enough for helping me with all the paperwork required, not just for my thesis, but also my stay in France.

My friends and colleagues, especially, Rayisa Moyisenko, Alexia Bontempi, Guillaume Dodane, Stefania Oliveri, Tintu Kuriakose, Yanfeng Wang, Xavier Romain, Etienne Coffy, Tran Phong Nguyen, Gautier Lecoutre, Raya El Beainou, Séverine Denis, Shan Jiang and Maria Koroteava have my heartfelt gratitude for their support, patience, acceptance, encouragement and all the joyful memories I have of my time with them. I have learnt a lot from them and will always cherish the happy moments we spent together.

I hold my advisors, team members and friends responsible for all the positive changes in me as a researcher and as a person that I have become over the years.

Lastly, I would like to thank my loving family, for having faith in me and always motivating me to do what is right. If it had not been for them, I would have never been able to go this far.

Thank you all for being there for me.

"You can't cross the sea merely by standing and staring at the water." -Rabindranath Tagore.

Dedicated to my loving parents, Dr. Pulak Kumar Shaw and Sabita Shaw, and my inspiring sister, Dr. Surupa Shaw.

Contents

I	THESIS OBJECTIVE AND BACKGROUND STUDY	1
1	Introduction	3
2	State of the art	5
2.1	A brief summary of interferometric techniques	5
2.1.1	Homodyne Interferometry	5
2.1.2	Heterodyne Interferometry	7
2.1.3	Differential Interferometry	8
2.1.4	Sagnac Interferometry	10
2.2	A brief summary of Surface Acoustic Wave (SAW) Devices	11
2.2.1	Piezoelectricity	11
2.2.1.1	Coupling coefficient	12
2.2.1.2	Substrate material	13
2.2.2	Generation principle of Surface Acoustic Wave propagation	13
2.2.2.1	SAW in Inter-digital transducers (IDT)	14
2.2.2.2	Chirped IDT	16
2.2.2.3	Linear Frequency Modulation	16
2.2.3	A brief summary of different models for designing SAW Devices	17
2.2.3.1	The first order model	17
2.2.3.2	Equivalent circuit models	18
2.2.3.3	Coupling of modes (COM) model	20
2.2.3.4	The p-matrix model	21
2.2.4	The MatmixLib program	24
2.2.4.1	Computation of the global admittance matrix	24
2.2.4.2	The Grid	25
2.3	Pulse compression	26
2.4	Conclusion	27

II	CONTRIBUTION	29
3	Chirped inter-digital transducers	31
3.1	Inter-digital transducer modelling	31
3.1.1	Material selection and design parameters	31
3.1.2	The delta function model	34
3.1.3	The p-matrix model	36
3.2	Reference sample	37
3.3	Fabrication	39
3.3.1	Material selection	39
3.3.2	Lithography and Deposition	40
3.4	Results and dicussion	42
3.5	Appearance of band gaps	45
3.5.1	Band gaps within a single period IDT	47
3.5.2	Band gaps within a Chirped IDT	49
3.5.2.1	Experimental results	58
3.5.3	Variation in the height of the electrodes	58
3.6	Conclusion	62
4	A differential optical interferometer	65
4.1	Interferometers for short pulse measurements	65
4.2	Working principle of the differential interferometer	67
4.3	Pulse compression experiment	69
4.4	Measurement characteristics	71
4.5	Pulse compression along the chirped IDT	74
4.6	Conclusion	76
5	Pulse compression and optimization of a short pulse	79
5.1	Short pulse evaluation using simulated Chirps	79
5.1.1	The input chirp	80
5.1.1.1	Filter 1	81
5.1.1.2	Filter 2	82
5.1.1.3	Filter 3	83
5.1.2	Short pulse	85
5.2	Short pulse evaluation for the Fabricated SAW devices	87
5.2.1	Pulse compression experiment	90

5.2.2	Results and discussion	91
5.2.2.1	Optimization of a Short pulse	92
5.3	Conclusion	94

III CONCLUSION 95

6 Conclusion and future work 97

|

THESIS OBJECTIVE AND BACKGROUND STUDY

Introduction

Short acoustic pulse generation can be achieved by several methods like picosecond energetic laser pulses produced by a passively mode-locked laser. Generation of intense short pulses of surface acoustic waves (SAW), either from the absorption of a short laser light pulse or from piezoelectric transduction, has important potential applications. In addition to surface phonon generation [1] and non destructive evaluation [2], it could for instance be used for acoustic soliton generation, higher harmonics generation, and more generally nonlinear acoustical signal processing. Indeed, the mechanical energy transported by SAW is strongly confined at the surface, causing a high density of elastic energy and induced strain in the supporting material. As a result, even a modest initial acoustic power could in principle be capable of inducing substantial nonlinear effects, especially if combined with pulse compression techniques similar to those used to achieve intense ultrashort laser light pulses using the chirped-pulse amplification (CPA) technique [3]. As a pre-requisite, it is also needed to develop the measurement of short SAW pulses in the time domain.

The chirped pulse amplification technique has been studied extensively as it has important applications in various fields like in optical radar and ranging technologies. There are three stages in this process. An initial pulse is stretched, which causes the temporal pulse-width to increase as shown in Fig. 1.1. The peak power decreases as the energy is spread over a longer time period. Several techniques, for example, variation in the dispersion parameters of nonlinear photonic crystal fibers (PCF) [4], prisms [5], or different grating arrangements [6], like, with a set of two gratings arranged anti-parallel to each other with even number of lenses, or arranged parallel to each other with odd number of lenses, etc., have been used to stretch input pulses with negligible distortion. This pulse then passes through a high voltage amplifier. Although the pulse energy is increased, the peak-power remains fairly low producing negligible nonlinearities. Finally, the pulse is compressed back to its limited width. Different grating arrangements have been used as external dispersive elements in the past for this purpose [3]. However, there can be some side effects of this pulse compression technique. The power of the peak pulse can be too high after compression causing a severe spatial deformation of the beam as it passes through any thick optical element. A combination of a double-pass stretcher configuration and a compressor with gratings twice as large in a single-pass configuration can be used to compensate this effect [6].

Inspired by the chirped pulse amplification technique, this work is focused on the study of generation and measurements of short pulses of surface acoustic waves (SAW) in ultra wide band (UWB) SAW devices. In our case, the temporal compression of pulses is achieved with a surface acoustic wave transducer as a dispersive element, emitting surface wave packets, or surface phonons. In order to be able to study the propagation of SAW within the device, an interferometer capable of measuring these short pulses is required, that will allow scanning of

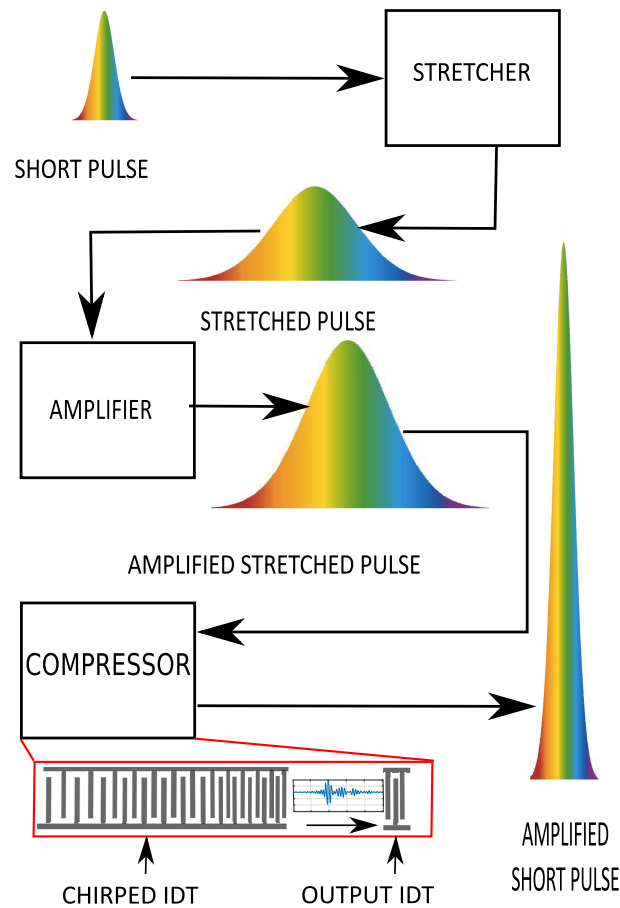


Figure 1.1: A Schematic illustration of the chirped pulse amplification technique.

these devices to investigate amplitude and phase variations at any position within the SAW devices. This measurement tool could also be used to explore acoustic nonlinearities on the piezoelectric substrates and its effects on pulse compression, although this is left for future work. It would allow studies of various IDT designs like IDT rings [7], fabricated to produce focused short pulses. The performance of the SAW devices for generating short pulses designed and fabricated for this work can be used to create better designs for various sensor applications.

In this thesis, following a brief summary of the state of the art relevant to this work, presented in chapter two, we discuss the design and fabrication of the SAW devices comprising two inter-digital transducers, used to generate short pulses in chapter three. Band gap generation within the chirped input inter-digital transducers (CIDT) and its effects on the directionality of the transducer response are investigated. In chapter four, a stabilized time-domain differential interferometer is proposed for short SAW pulse measurements. It is used in an experimental setup designed to employ the principle of chirped pulse amplification (CPA) described above, to measure the pulses and to investigate pulse compression at different positions within the device. Chapter five presents a study on optimization and amplification of short pulses obtained using different SAW devices. Finally, an overall summary of this work is presented with future perspectives in the conclusion.

State of the art

This chapter is devoted to describing and summarizing the basic concepts used to understand SAW propagation in inter-digital transducers, pulse compression, and the use of optical interferometry for study of surface acoustic wave propagation.

2.1/ A brief summary of interferometric techniques

Optical interferometry forms the basis of metrology in numerous high-precision displacement measurement applications by investigating fringe patterns formed due to the interference for two beams. It allows for non destructive evaluation and quantification of wave propagation in various devices with vibrations of varying amplitudes typically ranging from the order of a few nanometers to picometers. Improvements in instrument technology and realization of causes of subtle errors in measurements, have contributed to improvements in the resolution, repeatability and dynamic range of interferometric measurements of ultrasonic vibrations. We begin with a review of different optical interferometers that can be employed to measure vibrations or short pulses in the time domain.

2.1.1/ Homodyne Interferometry

The homodyne interferometers used in ultrasonic wave propagation investigation are typically based on either Michelson or Mach-Zender interferometer configurations. In homodyne interferometry as shown in Fig. 2.1 for a Michelson's interferometer, a linearly polarized laser beam is used as a coherent light source. The laser beam is split into two coherent beams of equal intensity and orthogonally polarized by the polarizing beam splitter with a partially reflecting film oriented at 45° to the beam, one reflected by a mirror, thus forming a reference beam, and the other is reflected by a sample intended to be studied or another mirror placed at a certain path length. On recombining at the beam splitter, both beams with a path length difference interfere. The basic equation for the two beam interference, when both beams are reflected by plane mirrors, is given by

$$I(t) = I_1 + I_2 + 2\sqrt{I_1 I_2} \cos(\phi_2(t) - \phi_1(t)), \quad (2.1)$$

where I_1 and I_2 are the intensities and ϕ_1 and ϕ_2 are the phases of the two respective beams, and $\phi = \phi_2 - \phi_1$, is the phase difference between the two beams along each arm. The polarization of the reflected beams is adjusted to circular using a quarter waveplate QWP. The relative phase of the two beams determines whether the interference will be constructive or destructive. Depending on the path length difference the last term in equation 2.1 is either

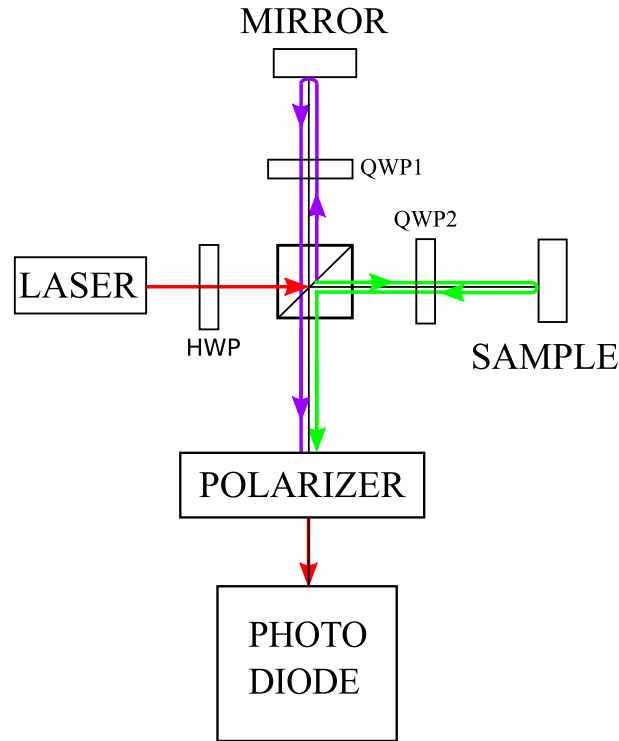


Figure 2.1: Schematic of a homodyne Michelson interferometer

positive or negative. A change in inclination of the mirror, can produce fringes, straight-line fringes, or curved fringes. When one of the beams is reflected back from a vibrating sample surface, the phase difference can be written as

$$\phi(t) = \Psi(t) + \frac{4\pi}{\lambda}u(x, t) \quad (2.2)$$

and the intensity at the photodiode becomes

$$I(\phi) = I_1 + I_2 + 2\sqrt{I_1 I_2} \cos\left(\Psi(t) + \frac{4\pi}{\lambda}u(x, t)\right) \quad (2.3)$$

Equation 2.3 gives the interferometer response when a sample with an ultrasonic displacement u , is placed in the position of a mirror along an arm of the interferometer.

Here, u is the displacement at position x and of time t , λ is the wavelength of the laser beam used for the experiment, and $\Psi(t)$ is a slow phase drift caused due to arbitrary environmental noise and is generally a random number.

The homodyne technique allows for high resolution measurements but the homodyne Michelson's interferometer setup is extremely sensitive to noise, which can be responsible for major errors in measurements when the amplitude of the noise is much larger than that of the ultrasonic displacement intended to be measured. Several stabilization techniques have been proposed over the years to achieve noise stabilization like tuning the second harmonic of the voltage fluctuation applied to a piezoelectric actuator, vibrating piezoelectric actuators in stabilization loops with an amplitude larger than $\lambda/2$ or vibrating them at a frequency higher than the response bandwidth of the stabilization loop [8]. It is also possible to eliminate noise sensitivity of the setup by maintaining the two interfering beams in quadrature by using the output signal to adjust the reference mirror slightly, to compensate for changes in the optical

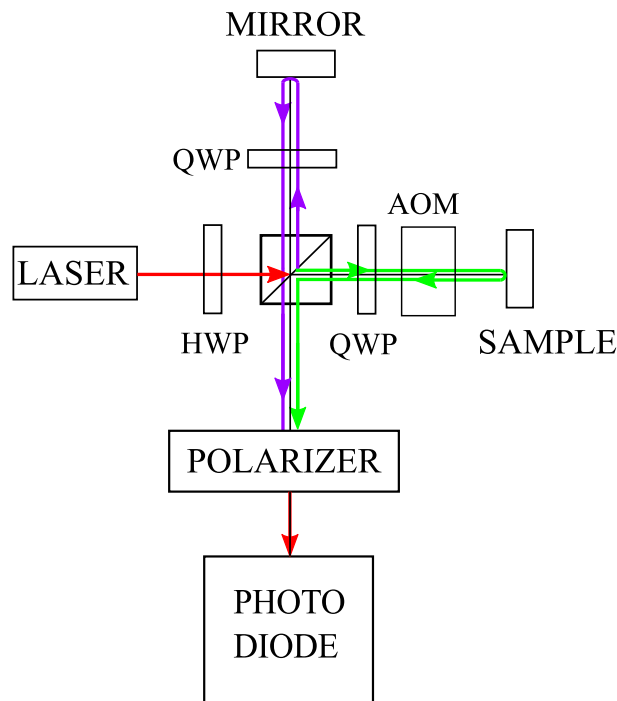


Figure 2.2: Schematic of a heterodyne interferometer

path lengths due to air flows or difference in heights of the features on the sample surface. Quantification and compensation of system gains and variations in optical reflectivity of the sample surface allow phase sensitive detection of the ultrasonic vibrations and acquisition of absolute amplitude data [9].

2.1.2/ Heterodyne Interferometry

In contrast to the homodyne technique, in Heterodyne laser interferometry as shown in Fig. 2.2 for a Michelson's interferometer, the wave incident on the specimen has a frequency offset, created using an acousto-optic modulator (AOM), with respect to the reference wave. The use of this modulator allows measuring of the zero order term and it uses it to cancel slow mechanical vibrations as it shifts the original frequency in one arm from f to $f + f_m$, where $f_m \ll f$, and the response obtained due to the interference of the reference and frequency-shifted beams is given by equation 2.4. A half wave plate (HWP), and two quarter wave plates (QWP) used to adjust the polarization of the travelling beams, in order to produce a plane polarized beam at the output

$$I(t) = I_1 + I_2 + 2\sqrt{I_1 I_2} \cos[\Psi(t) - \frac{4\pi}{\lambda}u(x, t) + 2\pi f_m t] \quad (2.4)$$

where I_1 and I_2 are the intensities of the two beams, f_m is the frequency offset added by the AOM, $\Psi(t)$ is the slow drift due to minor variations in the setup environment caused by temperature, airflow, etc., u is the surface displacement and λ is the wavelength of the laser beam used as the light source. equation 2.4 can be expanded using the trigonometric identity given by equation 2.5 to equation 2.6

$$\cos(A - B) = \cos A \cos B + \sin A \sin B \quad (2.5)$$

$$I(t) = I_1 + I_2 + 2\sqrt{I_1 I_2} \left[\cos(\Psi(t) + 2\pi f_m t) \cos\left(\frac{4\pi}{\lambda} u(x, t)\right) + \sin(\Psi(t) + 2\pi f_m t) \sin\left(\frac{4\pi}{\lambda} u(x, t)\right) \right] \quad (2.6)$$

The signal spectrum in the frequency domain consists of a modulation peak at f_m and two side peaks at $f_m \pm f_s$. The side peak with the higher frequency is the signal peak and it is detected simultaneously with the modulation peak. The absolute amplitude of the surface vibration can be acquired from their amplitude ratio. Also, by comparing the phases of the two signals, the phase of the surface vibration can be acquired, and any slow variations in the optical path lengths cancel out.

Several nonlinearities due to frequency mixing, polarization mixing, ghost reflections, etc., are not included in equation 2.6, but have been observed in heterodyne interferometry. They are found to arise due to imperfections of optical components and anisotropic laser sources, limiting the accuracy of displacement measurements at the nanometer level, according to Wu and Deslattes [10]. However, in recent years, heterodyne setups are capable of detecting vibration amplitudes down to ≈ 1 pm [11].

Both homodyne and heterodyne techniques used for the Michelson's interferometer are very effective for making accurate and high precision measurements but are not suitable for measuring short pulses. This is because the homodyne setup is extremely sensitive to noise and for the heterodyne setup, for short pulses, the frequency bandwidth is large and there is a possibility of mixing between the side peaks and the modulation peaks which would make the extraction of the signal difficult. Even if mixing is not present, a demodulation step is necessary to remove the modulation at the frequency f_m and recover the pulse $u(x, t)$.

2.1.3/ Differential Interferometry

In the past, two-beam differential interferometric techniques implementing space-shearing have been employed to detect and measure surface acoustic waves [12–17]. For example, Turner and Claus used a simple dual interferometer with two pairs of orthogonally polarized optical beams, in 1981, to measure the amplitude and direction of propagation of broadband ultrasonic surface waves [12]. Differential interferometer setups were used to study several models of compressional wave propagation to detect and analyse defects [18]. Picosecond acoustic interferometry [13] was used by Lin et al. to measure the attenuation and velocity of longitudinal acoustic phonons in the Brillouin frequency range. The advantage of optical interferometry, i.e., being sensitive to the amplitude and phase of acoustic signals, was used by X. Jia [14] et al. to study guided acoustic waves in transparent isotropic media. Acoustic pulses as short as 2 picoseconds, were measured using time – resolved plasmonic interferometry by Mante [15] et al. in 2013. Interferometry has found application in non-destructive evaluation of materials, and in different kinds of wave propagation studies in isotropic and anisotropic media.

Differential interferometers have proved to be useful in various fields, like piezoelectric thin film characterization [19], angular measurements of the order of nano-radians and displacement measurements in the picometer range, of acoustic signals [20], etc. A major advantage of a differential or a shearing interferometer is that it eliminates the requirement of a reference surface. The principle behind this setup is to measure the interference of two wavefronts that could be obtained from one single point on the surface illuminated by two distinct beams,

which is also referred to as differential interferometry for in-plane measurement, or, two distinct points, also known as differential displacement interferometry. In case of lateral shearing, the reflections from the test surface are laterally displaced with respect to each other. In case of radial shearing the setup is designed to allow interference between reflected beams of different radii. High sensitivity to the phase and amplitude of the acoustic signals and easy calibration of the setup are the key advantages of a differential interferometer. They are a solution to a common disadvantage of interferometry, i.e., path length sensitivity. An interferometer setup combining the heterodyne technique with differential interferometry allowing both in-plane and out-of-plane ultrasonic displacement measurements has also been described in the past [8, 10, 21, 22].

The differential interferometer setup developed by Palmer and Green could be used to detect a SAW displacement of 6×10^{-14} m, on glass, and was unaffected by focal errors up to ± 1 mm [20]. For a laterally shearing interferometer as shown in figure 2.3 with a laser beam of input intensity I_0 , the horizontal I_h and vertical I_v components of the intensity are given by

$$I_h = \frac{I_0}{2}[1 + \cos(2k(x_2 - x_1)) + \psi] \quad (2.7)$$

$$I_v = \frac{I_0}{2}[1 + \cos(2k(x_2 - x_1)) + \psi - \pi/2] \quad (2.8)$$

where x_1 and x_2 are the two positions between which the lateral shearing occurs, k is the wavenumber and ψ accounts for the slow drifts in phase due to environmental noise. An additional delay of $\pi/2$ in the phase of the vertical component is added by a half wave plate. Assuming that $\Delta x_2 \ll \lambda$ for high frequencies, the change in the horizontal and vertical components are given by

$$\Delta I_h = -I_0 k [\sin(2k(x_2 - x_1)) + \psi] \Delta x_2 I_h = \frac{I_0}{2} [1 + \cos(2k(x_2 - x_1)) + \psi] \quad (2.9)$$

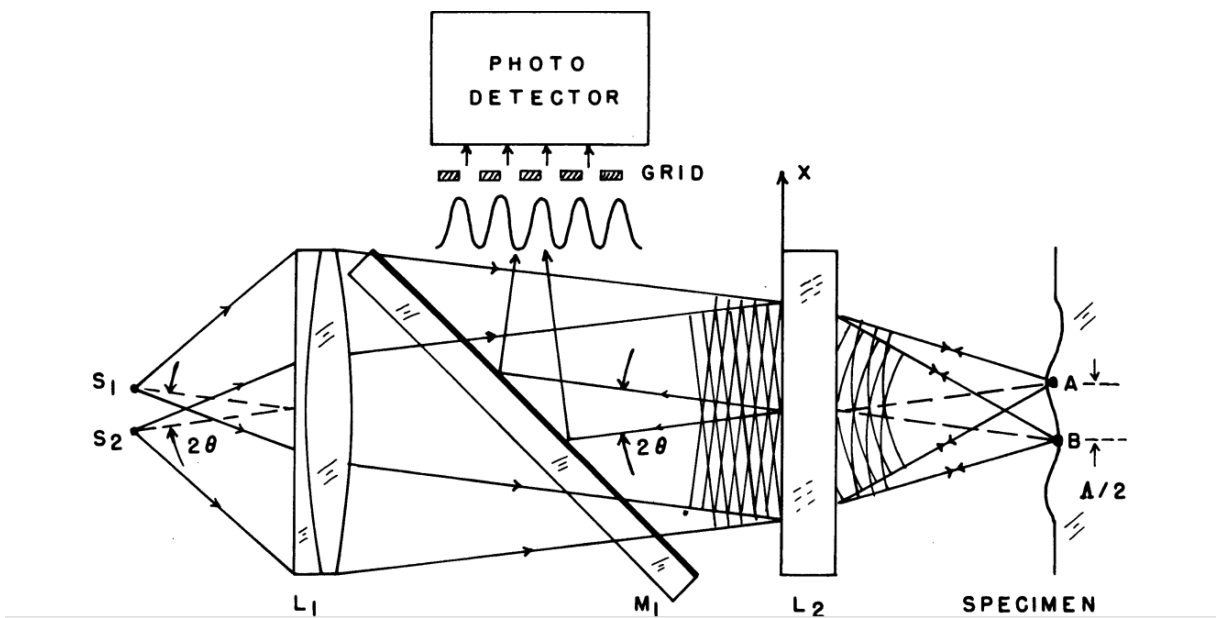


Figure 2.3: A Schematic of a differential interferometer proposed by Palmer and green [20] .

$$\Delta I_v = -I_0 k [\cos(2k(x_2 - x_1)) + \psi] \Delta x_2 I_h = \frac{I_0}{2} [1 + \cos(2k(x_2 - x_1)) + \psi] \quad (2.10)$$

The final output signal is obtained by squaring and adding the two components and is given by

$$V_{output} \propto I_0^2 k^2 (\Delta x_2)^2 \quad (2.11)$$

where V_{output} is independent of x_1 and x_2 . This system has uniform sensitivity for any position of the reference beam mirror but since the phase information cannot be extracted easily it is not very useful.

These spatial shearing interferometer setups are capable of providing very high precision measurements for time harmonic signals but are not suitable for measuring short pulses. However, differential interferometry implementing time-shearing can be used for this purpose as we will show in chapter three.

2.1.4/ Sagnac Interferometry

A Sagnac interferometer, very effective for gravitational wave study [23–25], is a common path interferometer which uses the Sagnac effect, first utilized in an experiment by Georges Sagnac in 1913 [26]. The monochromatic laser beam in this interferometer is split into two orthogonally polarized beams traversing the same path of micro-optical elements, but in opposite directions. This provides setup stability against vibration. The beams recombine at the splitting beam splitter and the resulting beam is detected by a photo-diode, as shown in the schematic of the Sagnac interferometer setup in Fig. 2.4. In a basic setup the two beams travel clockwise and anticlockwise with phases ϕ_{cw} and ϕ_{ccw} respectively. If the ultrasonic vibration is assumed to be normal to the detector plane and is positively polarized, with the displacement $u(x, t)$ (at the position x on the sample), along each interferometer arm being 180 degree out of phase, consequently, clockwise and counterclockwise beams experience time-dependent phase shifts.

This type of an interferometer has been used previously by Hashimoto et al. [27] for visualization of a field pattern on the vibrating surface of an RF BAW resonator operating in the 2 GHz range which could be used for SAW devices operating in the 1 GHz range also. However, the Sagnac interferometer setup proposed by Wright et al. [1], can be used for the selective detection of RF out-of-plane displacement associated with RF SAW/BAW propagation, and is an example of a setup capable of measuring short pulses. They essentially describe an improved two-dimensional optical scanning technique combined with an ultrafast Sagnac interferometer for delayed-probe imaging of surface wave propagation. A two-axis rotating mirror is incorporated in this setup to allow optical generation and detection of SAW by the use of a single objective lens which overcame the limitation of a requirement for oblique incidence for one of the optical beams for setups discussed in their previous work [28, 29]. A differential measurement is presented by comparing the reflectance of the sample at the times of arrival of the two optical probe pulses. By controlling the difference in the length of the arms of the interferometer, time shearing can be achieved, allowing measurement of short pulses. In this setup, the optical phase difference $\Delta\phi$ contains a dominant contribution from the difference in outward surface displacement Δz at the times of arrival of the two probe pulses, where $\Delta z = 4\pi\Delta z/\lambda$, where λ is the central wavelength of the optical probe beams. The common path arrangement of this setup ensures the exact temporal coincidence and interference of the two probe pulses for any coherence length of the light.

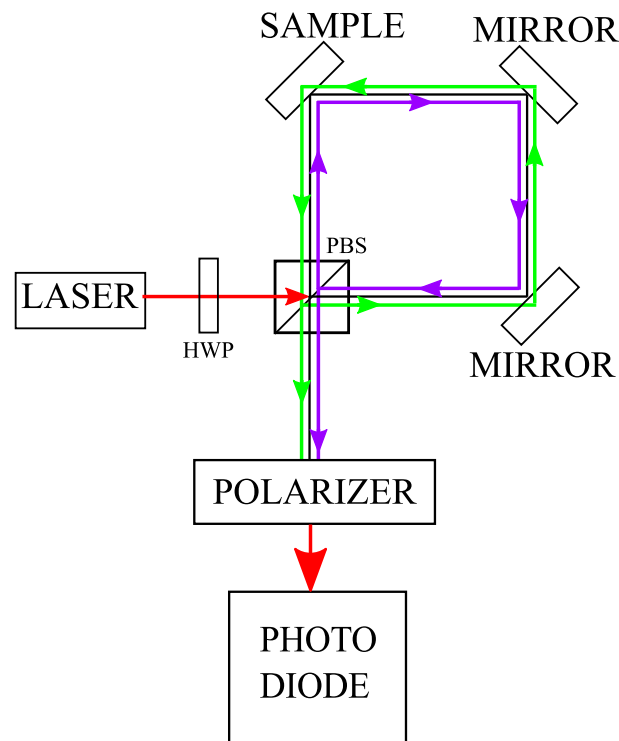


Figure 2.4: Schematic of a Sagnac interferometer

This setup is effective for cases where excitation of SAW is both optical and non-optical provided it is synchronous, for example SAW devices with IDTs. In chapter four, we describe another interferometer setup which is also capable of short pulse measurements.

2.2/ A brief summary of Surface Acoustic Wave (SAW) Devices

Surface acoustic waves, first described by Lord Rayleigh in 1885 [30], are non-dispersive mechanical waves that propagate along the surface of a solid material. The displacement amplitude of these waves decay exponentially along the depth of the material, from the surface. Most of the energy is confined within a depth equivalent to a few wavelengths of the wave. The velocity is typically in the range $1500\text{--}4000\text{ m}\cdot\text{s}^{-1}$ [31]. Among many applications, surface acoustic wave technology, for example, has been used to design devices that can be used as pressure, gas, electrochemical, or temperature sensors and biosensors, and several measures have been proposed to improve them to withstand harsh environments and provide a good performance [32–49].

In this section, we discuss one of the most common ways to generate SAW, that is by applying an electric field to a material exhibiting piezoelectricity where the mechanical and electric fields are coupled at the atomic level.

2.2.1/ Piezoelectricity

Piezoelectricity was discovered in 1880 by Jacques and Pierre Curie during experiments on quartz [50], and on other materials such as tourmaline, topaz, cane sugar and Rochelle salt

that displayed surface charges when they were mechanically stressed. The converse piezoelectric effect was mathematically predicted from the fundamental laws of thermodynamics by Lippmann [51] in 1881, and experimentally confirmed by the Curie brothers.

2.2.1.1/ Coupling coefficient

Piezoelectricity is the coupling between electricity and elasticity, or in other words, is the ability of a substance to produce electric charge when mechanical stress is applied to it, and, conversely, undergo mechanical deformation when an electric field is applied. The piezoelectric effect originates from the anisotropy of the crystalline structure, and occurs due to a non-uniform distribution of charges within a crystal lattice, as shown in figure 2.5. A mechanical stress applied to the material causes a deformation of the crystalline structure, either by re-configuration of ions within the structure or by re-orientation of molecular groups, which results in a change in the direction of polarization of the electric dipoles within the substance. This leads to the generation of electric charge. Piezoelectric materials exhibit electrical behavior below a certain temperature called Curie temperature, above which they don't exhibit any dipole moment.

The piezoelectric coupling coefficient K^2 represents the effectiveness with which a piezoelectric material transforms electrical energy to mechanical energy and vice versa. It is a key parameter in designing SAW devices as it is proportional to the radiation conductance of the IDTs, and is given by equation 2.12.

$$K^2 \approx 2 \frac{\nu_f - \nu_m}{\nu_f} \quad (2.12)$$

where ν_f is the SAW velocity on a free surface of the piezoelectric material, and ν_m is the SAW velocity on a surface with an infinitely thin perfectly conducting layer on it, when the SAW velocities are lower than the bulk acoustic wave (BAW) velocities.

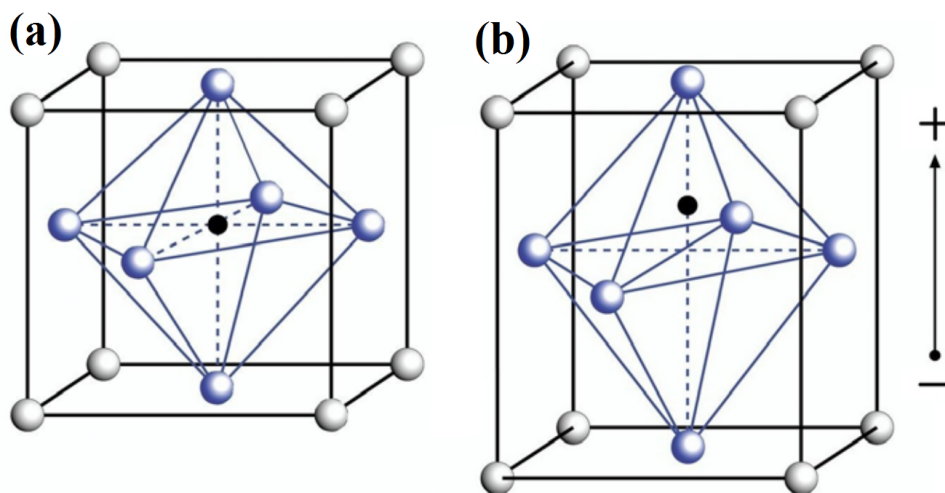


Figure 2.5: Unit Cell of a piezoelectric material with the center ion in black, (a) when the material is not electrically or mechanically excited, and (b) when the material is either mechanically stressed to produce an electric field or is excited by an electric field and physically deformed [52].

2.2.1.2/ Substrate material

There are several piezoelectric substrates used in SAW filter design. For example, YZ-lithium niobate (LiNbO_3), where Y is the cut and Z is the propagation direction, has a relatively high value of K^2 that make it very effective for wideband SAW filters and useful in radar pulse compression filters. As shown in table 2.1, lithium niobate crystals have a nonzero temperature coefficient of delay. The SAW velocity ν depends on the elasticity, density, and piezoelectric properties of the substrate used which are effected by temperature changes. The propagation time τ , between the input and output IDTs separated by distance d is given by $\tau = \frac{d}{\nu}$, which can also be effected by temperature fluctuations. This will normally not be critical in nonrecursive SAW filter applications at ambient temperatures. However, LiNbO_3 Y 128°-rotated X cut is a particular cut designed for reduced bulk wave generation over its Y - Z counterpart with a high K^2 . The attenuation values (α) for each substrate material is also given in the table. The values shown in table 2.1 are subjected to have slight differences as constant improvements are made in the growth processes for these piezoelectric crystals.

2.2.2/ Generation principle of Surface Acoustic Wave propagation

As a SAW propagates along an unbounded elastic surface, the surface undergoes a time dependent elliptical displacement, with one component of this physical displacement parallel to the direction of SAW propagation, and the other normal to the surface as shown in figure 2.6. The amplitudes of both of these SAW displacement components become negligible for penetration depths y greater than a few acoustic wavelengths ($\lambda = \nu/f$) into the body of the solid.

The mechanical equations of motion and Maxwell's equations for electromagnetic wave propagation need to be evaluated to describe the mechanism of elastic wave propagation in a piezoelectric medium. However, SAW waves propagate at velocities in the order of 10^5 less than the velocity of light, hence it may be determined that the mechanical solution will dominate such wave transport processes. The electrical potential Φ (in Volts) induced on the piezoelectric surface is given by [54]

Table 2.1: Piezoelectric materials used for SAW generation, where *SAW* is surface acoustic wave, *R* is Rayleigh wave, *PSAW* is the pseudo SAW waves and *BG* is the Bleusteiu-Gulyaev wave [53].

Crystal	Cut	Direction	Type	ν_m (m/s)	α (dB/ λ)	K^2 (%)
LiNbO_3	Y	Z	R	3390	0	4.5
LiNbO_3	Y+128	X	SAW	3870	0	5
LiNbO_3	Y+128	X	BG	4030	0	2.5×10^{-4}
LiNbO_3	Y+41	X	PSAW	4380	2×10^{-2}	16
LiTaO_3	Y	Z	R	3210	0	0.9
LiTaO_3	Y+36	X	PSAW	4110	3×10^{-4}	5.5
Quartz	Y+42	X	SAW	3158	0	0.11

$$\Phi = \phi(x, t) \approx |\Phi| e^{i(\omega t - k_x x)} e^{-k_y |y|}, \tag{2.13}$$

where x is the direction of SAW propagation, y is the along the depth of the substrate, and k_x and k_y are components of k (rad/m) in the x and y directions, where $k\lambda = 2\pi$, $\lambda = \nu/f$, is the acoustic wavelength at SAW velocity ν . The propagation of a SAW within the substrate in the y direction is minimal as it extends over a depth of a few acoustic wavelengths, hence the SAW propagation is considered to be confined to the surface ($y=0$) along the x axis. The spatial variations of the electric potential at the surface produces an electric field of intensity E ($\frac{V}{m}$). Along the SAW propagation axis, the longitudinal component E_x of electric field is given by $E_x = -\frac{\delta\Phi}{\delta x}$.

Assuming the piezoelectric surface stresses for SAW propagation to be predominantly compressional and the longitudinal component of the electric field E_x (where $E_y = 0$), generated due to the electrical potential Φ , being uniform within a defined penetration depth of the surface, SAW propagation can be defined by

$$E = E_x \approx |E| e^{i(\omega t - kx)} \tag{2.14}$$

with the SAW acoustic velocity $\nu = \frac{\omega}{k}$.

2.2.2.1/ SAW in Inter-digital transducers (IDT)

A simple SAW device consists of inter-digital transducers(IDTs) as shown in figure 2.7 . The first transducer (source) generates an elastic wave by applying a periodic variation of electrical potential and the second transducer (the receiver) receives it with a delay due to the propagation time of the wave on the piezoelectric substrate. This structure corresponds to a transmission delay line. It was first presented by White and Voltmer [57].

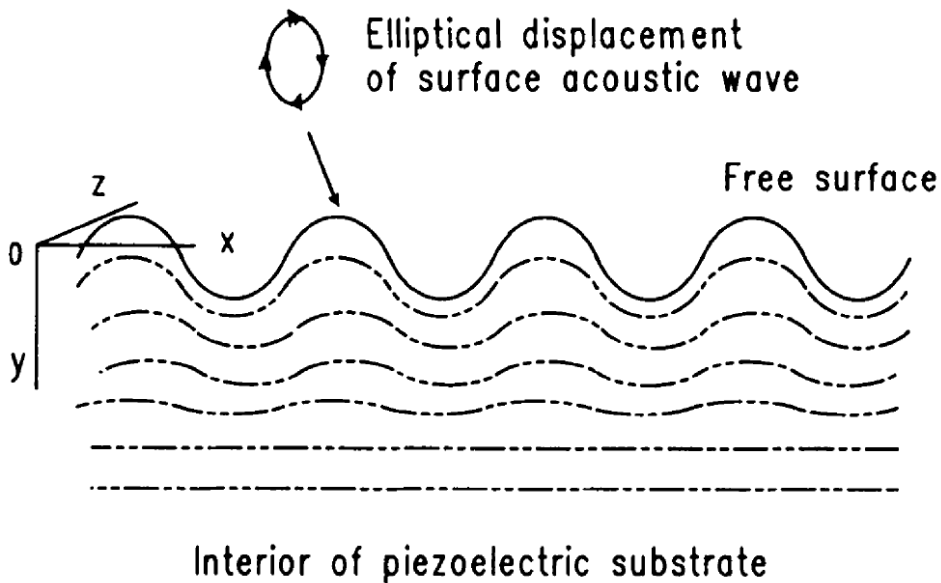


Figure 2.6: A pictorial representation (not to scale) of SAW motion on the surface of an elastic solid. Although the illustration relates to a piezoelectric solid, this is not a requirement for SAW propagation [54].

An IDT consists metal electrodes deposited on a piezoelectric substrate, arranged periodically and connected to metal bus bars. The center-to-center distance between two consecutive electrodes connected to the same bus bar, is called a period p as shown in figure. 2.7. The overlap between the electrodes connected to the two bus bars represent the acoustic aperture w . The simplest form of an IDT where a period p consists of a single pair of electrodes, is called a single-electrode-type IDT. The width a of each strip of electrodes is approximately equal to $\lambda/4$. The metal electrodes connected to the respective bus bars form two combs. When voltage is applied to the bus bars, the potential difference between the two combs generates mechanical stress on the piezoelectric substrate. This oscillating mechanical stress creates SAWs that propagate on both sides of the transducer. The transducer is effective if the spatial period p , of the electrodes respects the conditions of synchronism with the elastic

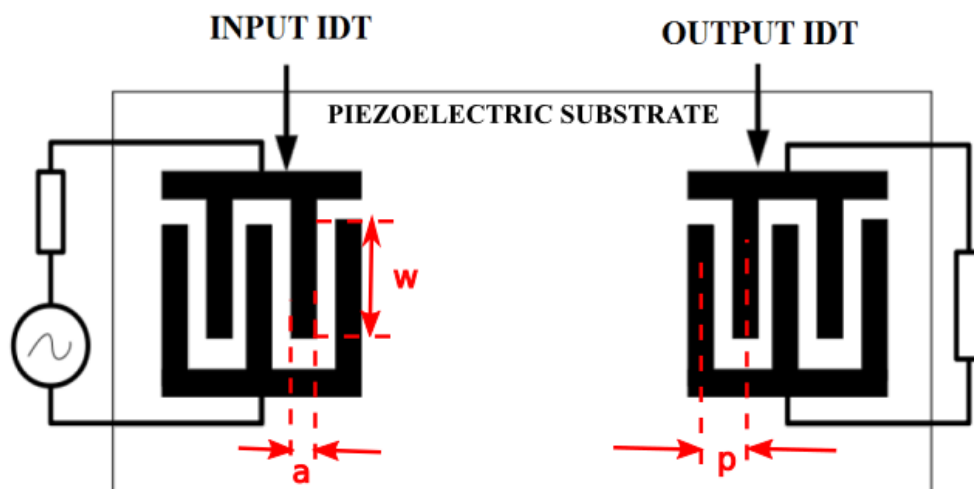


Figure 2.7: A schematic of a basic saw device [55].

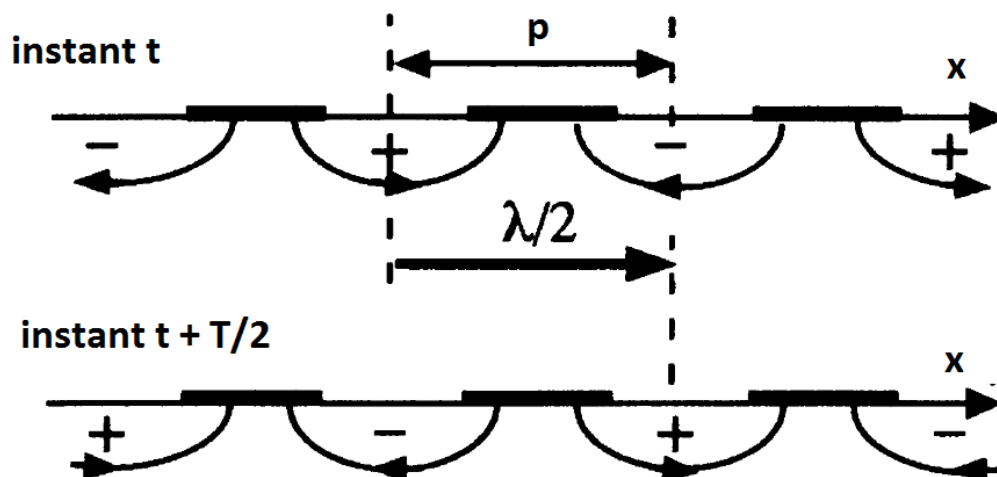


Figure 2.8: A schematic showing voltage applied across the two comb-shaped electrodes produces stresses near the solid surface [56].

wave.

In case of a single-electrode-type IDT, for a sinusoidal supply voltage, the vibrations add constructively if the pitch p is $\frac{\lambda}{2}$. Any stress produced at time t by a pair of fingers, for a given polarity of the voltage, travels the distance $\frac{\lambda}{2}$ during the half-period $T/2$, at the SAW speed ν , as seen in figure 2.8. At time $t + T/2$, when the voltage is of opposite polarity, the stress propagates under the neighbouring finger pair which produces a stress with the same phase. The stress due to the second pair of fingers adds constructively to the first [56]. For an IDT with N finger pairs, when a voltage is applied the electric field is reversed at each interval between the fingers and the transmitted has a frequency response $f = \frac{\nu}{2p}$. If the SAW device uses only one side of the IDT, only half the energy propagates to the output IDT.

2.2.2.2/ Chirped IDT

A chirped IDT (CIDT) is an IDT where the pitch p varies as shown in figure 2.9. When a voltage is applied along the bus bars of such an IDT, a range of frequency are generated. The frequency bandwidth B , of the IDT response ('chirp') corresponds to the pitch variation for a give SAW velocity ν . The limiting frequencies of the bandwidth can be calculated using the simple relation: $f = \frac{\nu}{2p}$, for a single electrode type CIDT. When the pitch varies from a low value to a high value, the CIDT is called an up-chirp IDT and when p varies from a high value to a low value, it is called a down chirp IDT, as shown in figure 2.10.

In chapter 3, a comparison of the responses of an up-chirp and down-chirp CIDTs is presented.

2.2.2.3/ Linear Frequency Modulation

The position of the variable pitch electrodes can follow different types of distributions. One of the most widely known distributions is the Linear Frequency Modulation (LFM) [55]. For 150 pairs of electrodes, a down chirp CIDT, generating a frequency bandwidth of 200 MHz - 400 MHz is shown in figure 2.9. The frequency variation for this case with respect to the position

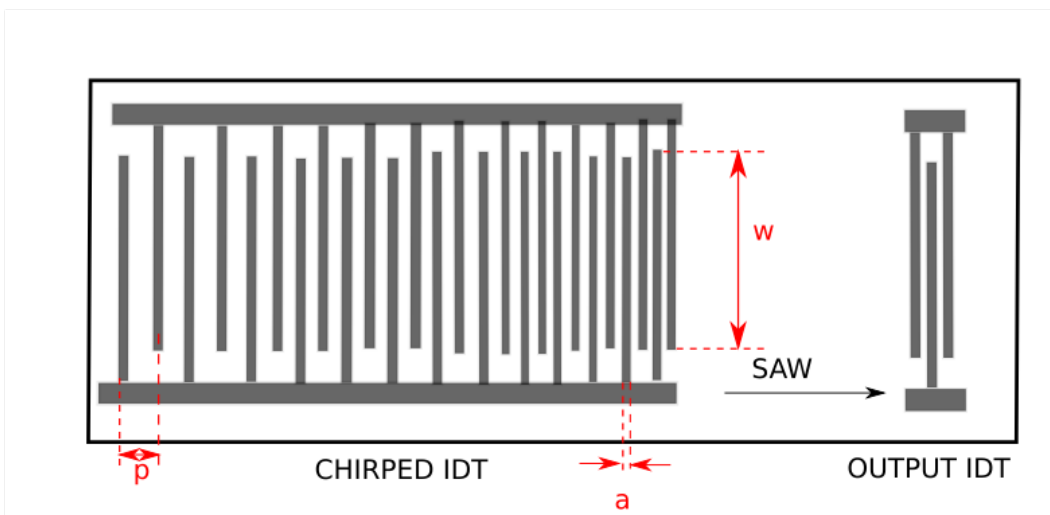


Figure 2.9: A Schematic of a surface acoustic wave device for generating a short pulse where p is the pitch of the IDT and a is the acoustic aperture.

fo electrodes is linear and is defined by the equation 2.15 [55]:

$$\omega = 2\pi \left(f_0 - \frac{B}{T}t \right), \quad (2.15)$$

where B is the frequency bandwidth, T is the signal duration and f_0 is the initial frequency. It must be kept in mind that in the following chapters the linear chirp case described is not the same as the one described in this section and should not be confused.

2.2.3/ A brief summary of different models for designing SAW Devices

Surface Acoustic Wave (SAW) devices, play an important role in today's telecommunication industry and are widely used as passive sensors and filters. Bandwidth and the energy efficiency of a transducer are the key points of a SAW device. Determination of the impulse response of the transducer using several numerical and theoretical models like the first order impulse model, the equivalent circuit models [31], the coupling-of-mode (COM) model, p-matrix model, angular spectrum of waves models and the Scattering Matrix approach, to pre-compensate the electrical excitation applied to the transducer allows emission of short ultrasonic pulses. Among these models, several of them include second order effects like reflections, dispersion, and charge distribution effects. We review their increasing order of complexity.

2.2.3.1/ The first order model

The first order model is simple and fast in estimating both, the mechanical and the electrical behavior of a SAW device. In this model an IDT is designed as an array of N discrete sources. These sources are located on the substrate between the electrode fingers with voltage of opposite polarity, as shown in figure 2.11. These The amplitude of the vertical displacement

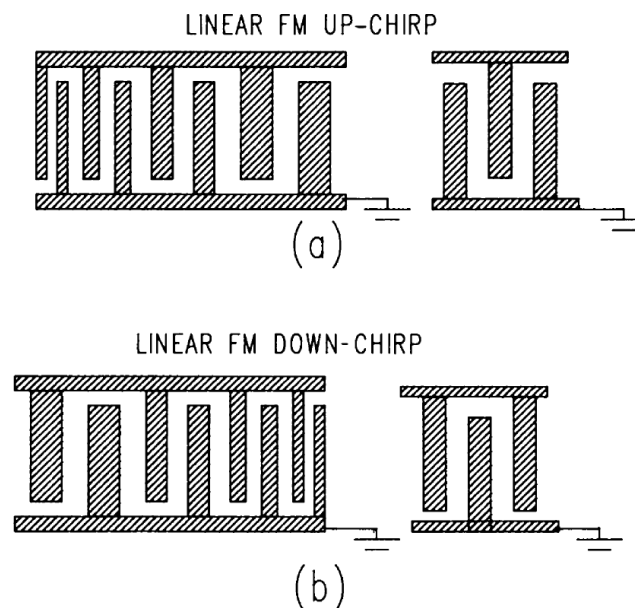


Figure 2.10: A schematic of SAW devices with (a) a linear up-chirp CIDT and (b) a linear down-chirp CIDT [54]

$u(f)$, at the exit of the IDT, on the right is given by the superposition of the response of each source

$$u(f) = \sum_{n=1}^N a_n \exp(-2i\pi f x_n / \nu) \quad (2.16)$$

where ν is the surface wave velocity, f is the frequency, x is the position within the IDT depending on the variation of the pitch, n is the number of fingers with N being the total number of IDT fingers, and a_n is the amplitude parameter (same as A_n in the figure 2.16 proportional to the finger overlap w or in other words, the acoustic aperture).

This model does not take into account second order effects such as reflections from individual electrodes, propagation losses and dispersion, which can be large enough to cause discernible modulations in the response of the SAW device. It does not estimate characteristics like filter input-output impedance levels, circuit factor loading, harmonic operation and bulk wave interference. However, it is a fast method to estimate the transduction between electrodes of an IDT and because of its simplicity, it is an effective tool for preliminary study of SAW devices and is used for a comparative study of SAW devices in chapter three.

2.2.3.2/ Equivalent circuit models

Several extended versions of the first order model, like the impulse response model which is a kind of an equivalent circuit model proposed by Hartmann et al. [58], have been designed to include the second order effects like triple transit echoes that occur when a part of the signal is reflected back and forth between the receiving and transmitting IDTs. An advantage of this

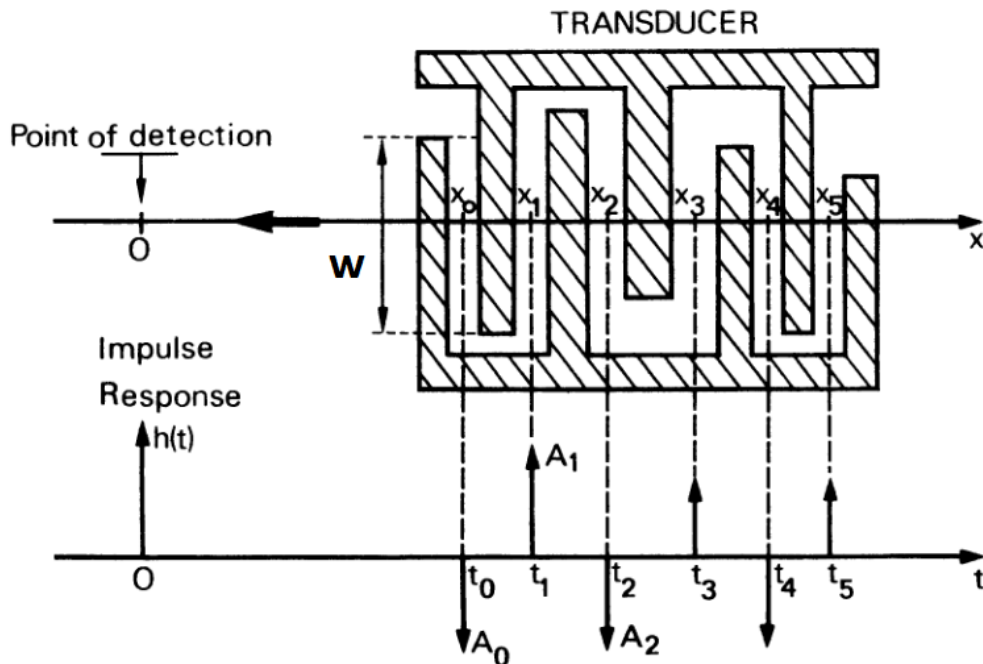


Figure 2.11: A schematic of a first order model of an IDT in which the IDT is modelled by an array of discrete sources at the centres of interdigital intervals, with amplitudes proportional to the finger overlap w [56].

model over the first order model is that it provides information on frequency scaling required for apodization quantities for broadband or chirp SAW filters. For an IDT with N finger pairs, the impulse response $u(t)$ and its frequency response are given by [54].

$$u(t) = \sqrt{4K^2C_s}f_0^{\frac{3}{2}} \sin(2\pi f_0 t) \quad \text{for} \quad 0 \leq t \leq \frac{N}{f_0} \quad (2.17)$$

$$|u(f)| = 2\sqrt{K^2C_s}f_0N \frac{\sin N\pi(f-f_0)/f_0}{N\pi(f-f_0)/f_0} \quad (2.18)$$

where K^2 is the electromechanical coupling coefficient and C_s is the capacitance of an electrode finger pair, $t = x/v$ is the time for the SAW to traverse to a given position along the IDT x at velocity v along the reference x-axis and f_0 is the synchronous frequency appropriate to the pitch of the IDT. This model incorporates the bi-directionality of an IDT.

Equivalent circuit models based on the crossed-field Mason circuit, is described by the basic three port network of an IDT for measuring surface acoustic waves, introduced by Smith et al. in 1969 [59] take into account reflections due to mechanical and electrical loading. This model describes a SAW device with two identical transducers without apodization and operating in transmission. A conventional matrix method proposed by Campbell based on this technique originally developed for microwave circuit analysis using transmission line theory, models an IDT as a single entity with an electrical port, and two acoustic ports. The equivalent current-voltage relations for a single IDT are given by

$$\begin{bmatrix} I_1 \\ I_2 \\ I_3 \end{bmatrix} = [Y] \begin{bmatrix} V_1 \\ V_2 \\ V_3 \end{bmatrix} \quad (2.19)$$

where, I_1 and I_2 , and V_1 and V_2 , are the current intensities and voltages at the two acoustic ports, respectively, and I_3 and V_3 are the current intensity and voltage at the electrical port, respectively. The admittance $[Y]$ is given by equation 2.20

$$[Y] = \begin{bmatrix} Y_{11} & Y_{12} & Y_{13} \\ Y_{21} & Y_{22} & Y_{23} \\ Y_{31} & Y_{32} & Y_{33} \end{bmatrix} \quad (2.20)$$

respecting symmetry and reciprocity relations given by $Y_{11} = Y_{22}$ and $Y_{21} = Y_{12}$, $Y_{23} = -Y_{32}$, and $Y_{31} = -Y_{13}$ for the electrical port 3 to account for the bi-directionality, i.e., SAW being generated in both directions. The other elements of the admittance matrix are given by equation 2.21

$$\begin{aligned} Y_{11} &= -jY_0/\tan(N\theta) \\ Y_{12} &= jY_0/\sin(N\theta) \\ Y_{13} &= -jY_0 \tan(\theta/4) \\ Y_{33} &= j\omega C_T + j4NY_0 \tan(\theta/4) \end{aligned} \quad (2.21)$$

where $Y_0 = 1/Z_0$, is the characteristic admittance (S), $C_T = NC$, is the total IDT capacitance (F), for N electrode pairs with C being the capacitance of one finger pair (F) and $\theta = 2\pi(f/f_0)$, is the electrical transit angle, in radians, through one period [54]. This particular model not only provides information on the IDT input and output impedance levels, it also provides an estimation of the triple-transit interference levels in the filter passband and on the frequency

sensitivity of the electrodes. This method has been further improved to consider the frequency shift due to the mass loading of the metal fingers [60].

This equivalent circuit model based on the Mason's circuit, is an effective tool to estimate the response of an IDT and is used to design the sample used as a reference for this work, described in section 2.2.2.2, which incorporates apodization for weighting the response of the IDT (one of the advantages of this model).

This model takes into account the mechanical and electrical behavior of the SAW device but does not take into account phenomena of the second order, such as parasitic reflections. Other models have been proposed as discussed in section 2.2.3.3 and 2.2.3.4, which consider the second order effects.

2.2.3.3/ Coupling of modes (COM) model

Another well-established mathematical tool for the description of wave propagation in coupled systems is the coupling of modes (COM) theory based on the coupling of forward and backward propagating waves from a resonator with slowly varying complex amplitudes. It is well suited and extensively used to design single phased unidirectional transducers whose unidirectionality is significantly based on the collective effects of internal reflections. In this model, a SAW transducer with internal reflections is considered as a three-port device with one electric and two acoustic ports, and can be used to study the response of different kinds of gratings and resonators as its limiting cases.

For a periodic IDT grating of finite length the COM equations comprising of differential equations accounting for small perturbations, are given in equation 2.22 [61]

$$\begin{aligned} u_+(x) &= c_+ \exp(-j\theta_p x) + R_- c_- \exp(j\theta_p x) + \varepsilon_+ V \\ u_-(x) &= R_+ c_+ \exp(-j\theta_p x) + c_- \exp(j\theta_p x) + \varepsilon_- V \\ I(x) &= \int (-4j\zeta^* U_+(x) - 4j\zeta U_-(x) + jwCV) dx \end{aligned} \quad (2.22)$$

where u_{\pm} , R_{\pm} and ε_{\pm} are mode amplitudes for modes propagating in $\pm x$ directions, reflection coefficients, and transduction coefficients of SAWs propagating left and right, respectively, c_{\pm} account for the unknown boundary conditions in both directions, θ_p is the wavenumber of the perturbed mode coupled with the reflected wave, occurring in accordance with the Bragg condition, and is given by equation 2.23 with $|k_{12}|$ being the coupling coefficient.

$$\theta_p = \begin{cases} -\sqrt{\theta_u^2 - |k_{12}|^2} & (\theta_u < -|k_{12}|) \\ -j\sqrt{|k_{12}|^2 - \theta_u^2} & (\theta_u < |k_{12}|) \\ \sqrt{\theta_u^2 - |k_{12}|^2} & (\theta_u > |k_{12}|) \end{cases} \quad (2.23)$$

The main advantage of this model is that can be used to study several characteristics of SAW devices, like spatial variations in transduction, internal reflections and pitch, with arbitrary magnitude and phase, electrode resistivity and capacitance, spatial variation in SAW velocity and attenuation, and propagation loss within the substrate. A grating is represented as an array of several reflective elements that can be conducting or non-conducting grooves and stripe overlays and the total grating response is a superposition of all the element factors, and depends on the periodicity. Numerical techniques like approximating a transducer as a set of

small discrete sections, using COM theory to solve for each section and simulating the overall response by parallel/cascading of the individual sections can be useful to obtain a more general solution [62].

This model is also very effective in estimating IDT responses with good accuracy. However, a similar model known as the p-matrix model described in section 2.2.3.4, which characterizes the unit cell of an IDT as 3×3 matrix is used to design the IDTs.

2.2.3.4/ The p-matrix model

Tobolka in 1979 introduced another method popularly known today as the p-matrix model for an IDT transfer function. It is a mixed matrix approach where a SAW device is considered as a system of filter elements like transducers and reflectors, etc, each of which is represented as a set of smaller elements uniformly or non-uniformly divided into sub-cells balancing between accuracy and optimum computation time and represented by P matrices. The response of the entire system is obtained by cascading the individual matrices [63, 64]. A SAW transducer represented as a three port device has two acoustic ports described by an S-Matrix, and one electric port described by admittance. This model relates outgoing acoustic surface waves and the electric current to incoming acoustic surface waves and the voltage. In this model, use of Hilbert space transform to evaluate acoustic conductance over a broad band of frequencies allowed the estimation of the imaginary part of the admittance, i.e. susceptance.

The general relations of a p-matrix model for a single period transducer as shown in Fig. 2.12, are given by equation. 2.24, where A_i and A_t are the amplitudes of the waves entering and leaving the ports, subscripts 1 and 2 are the two acoustic ports, I is the current and V is the voltage at the electric port denoted by port 3. P_{33} is the auto-admittance, i.e. admittance observed when no acoustic wave is incident, P_{11} and P_{22} are reflection coefficients, P_{12} and P_{21} are transmission coefficients, and P_{31} , P_{32} , P_{13} , and P_{23} are transduction values for the respective ports [54, 55, 61].

$$\begin{bmatrix} A_{t1} \\ A_{t2} \\ I \end{bmatrix} = \begin{bmatrix} P_{11} & P_{12} & P_{13} \\ P_{21} & P_{22} & P_{23} \\ P_{31} & P_{32} & P_{33} \end{bmatrix} \begin{bmatrix} A_{i1} \\ A_{i2} \\ V \end{bmatrix} \quad (2.24)$$

The electrostatic charge distribution on the electrode section, calculated by a Green's function method [65], is used as excitation source. This has the advantage that the excitation is locally well defined in contrast to models which use stress or electrical fields as excitation sources. This particular model takes into account propagation losses and losses due to ohmic resistance. This model can be used to include bulk wave conversions also by introducing more acoustic ports or simply including it as losses at the finger edges [66]. The direct excitation of bulk waves can be included in post-processing also [67]. However, for the equations presented for this model in this chapter is purely for SAW generation assuming no bulk wave excitation. The amplitude A is usually defined such that the surface wave power is $|A|^2/2$.

The reciprocity relations for a SAW transducer is given by equation. 2.25 and the relations of the p-matrix elements with the scattering coefficients S_{ij} [68], are defined by equation 2.26 where R_s gives the characteristic impedance.

$$P_{21} = P_{12}; P_{31} = -2P_{13}; P_{32} = -2P_{23} \quad (2.25)$$

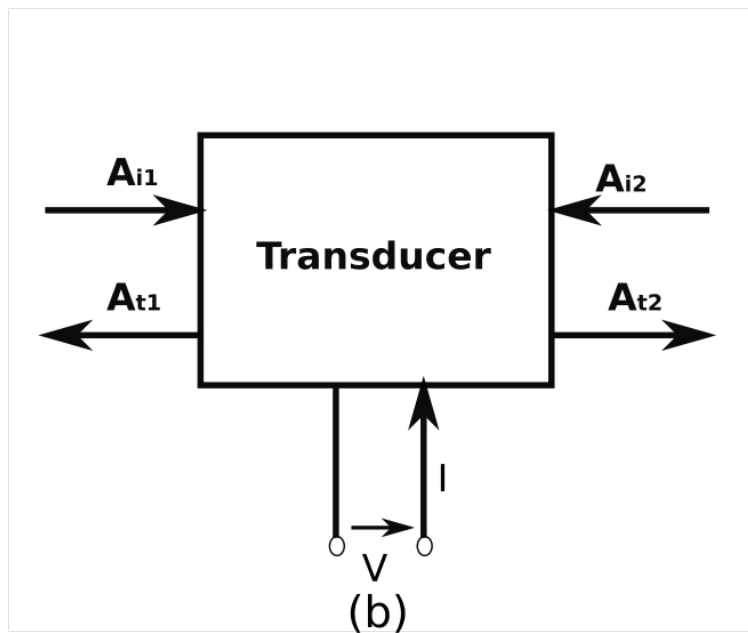
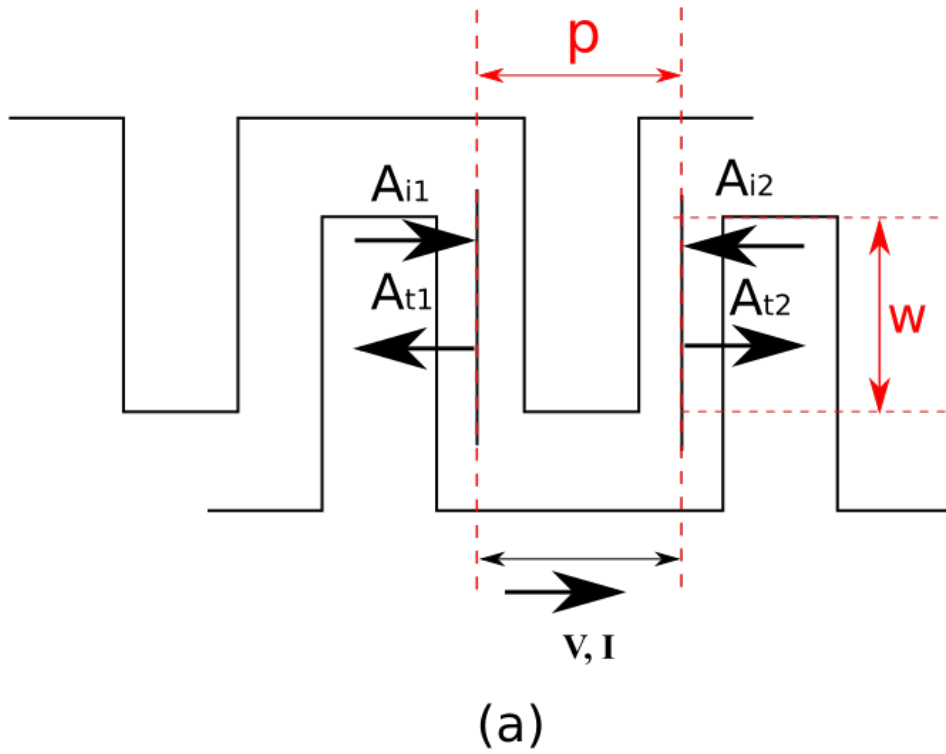


Figure 2.12: A Schematic representation of a single period transducer with the acoustic and electric ports.

$$\begin{aligned}
 P_{11} &= S_{11} - S_{13}^2 / (S_{33} + 1) \\
 P_{22} &= S_{22} - S_{23}^2 / (S_{33} + 1) \\
 P_{33} &= S_{12} - S_{13} S_{23} / (S_{33} + 1) \\
 P_{12} &= S_{13} - \sqrt{2R_s} / (S_{33} + 1) \\
 P_{23} &= S_{23} - S_{13}^2 / (S_{33} + 1) \\
 P_{13} &= R_s^{-1} - (1 - S_{13}) / (S_{33} + 1)
 \end{aligned}
 \tag{2.26}$$

Complex IDT structures for SAW devices can be represented using these p matrix cascading relations recursively. A chirped transducer grating can be represented as a group of small components (smaller transducers) generating different frequencies, each of which has one port facing the adjacent component. This allows the grating to be represented as an assembly of transducer elements with a chain or coincident ports. Two adjacent transducers with common bus bars, considered as two elements with the same aperture, having P matrices P^A and P^B are cascade-connected acoustically and parallel-connected electrically, the overall p matrix is given by

$$\begin{aligned}
P_{11} &= P_{11}^A + P_{11}^B \frac{P_{21}^A P_{12}^A}{1 - P_{11}^B P_{22}^A} \\
P_{12} &= \frac{P_{12}^A P_{12}^A}{1 - P_{11}^B P_{22}^A} \\
P_{13} &= P_{13}^A + P_{12}^A \frac{P_{13}^B + P_{11}^B P_{23}^A}{1 - P_{11}^B P_{22}^A} \\
P_{22} &= P_{22}^B + P_{22}^A \frac{P_{12}^B P_{21}^B}{1 - P_{11}^B P_{22}^A} \\
P_{23} &= P_{23}^B + P_{21}^B \frac{P_{23}^A + P_{22}^A P_{13}^B}{1 - P_{11}^B P_{22}^A} \\
P_{33} &= P_{33}^A + P_{33}^B + P_{32}^A \frac{P_{13}^B + P_{11}^B P_{23}^A}{1 - P_{11}^B P_{22}^A} + P_{31}^B \frac{P_{23}^A + P_{22}^A P_{13}^B}{1 - P_{11}^B P_{22}^A}
\end{aligned} \tag{2.27}$$

The admittance matrix Y_{ij} for a two port device can be calculated using equations 2.28 and 2.29

$$I_A = Y_{11}V_A + Y_{12}V_B \quad I_B = Y_{21}V_A + Y_{22}V_B \tag{2.28}$$

$$\begin{aligned}
Y_{11} &= P_{33}^A + \frac{2P_{11}^B (P_{13}^A)^2}{1 - P_{11}^A P_{11}^B} \\
Y_{12} = Y_{21} &= \frac{-2P_{13}^A P_{13}^B}{1 - P_{11}^A P_{11}^B} \\
Y_{22} &= P_{33}^B + \frac{2P_{11}^A (P_{13}^B)^2}{1 - P_{11}^A P_{11}^B}
\end{aligned} \tag{2.29}$$

Using the admittance matrices, the S parameters accounting for the reflection and transmission of the waves incident on the respective ports can be calculated using equation 2.30

$$\begin{aligned}
S_{12} = S_{21} &= \frac{2Y_{12} \sqrt{R_1 R_2}}{R_1 R_2 Y_{12}^2 - (1 + Y_{11} R_1)(1 + Y_{22} R_2)} \\
S_{11} &= \frac{(1 - R_1 Y_{11})(1 + R_2 Y_{22}) + R_1 R_2 Y_{12}^2}{(1 + R_1 Y_{11})(1 + R_2 Y_{22}) - R_1 R_2 Y_{12}^2}
\end{aligned} \tag{2.30}$$

and the S parameter S_{22} can be calculated using the equation for S_{11} with the indices 1 and 2 interchanged.

This model though robust in terms of accuracy as it includes several phenomena like triple transit echos, internal reflections from neighbouring electrodes, etc, to predict the IDT response, has its limitations. For example, when a voltage is applied to one IDT it generates electric charges along the fingers of this IDT but also along its neighboring fingers and cause

capacitive coupling between neighbouring elements and change the electro-acoustic excitation and detection of forward and backward propagating surface waves. This effect is not taken into account in the basic P matrix model.

2.2.4/ The MatmixLib program

In this section we discuss the program based on the p - matrix model, that is used to generate the CIDT responses, studied, and used to design SAW devices for this work.

The MatMixLib program constructed by C. De Sena, T. Pastureaud and Y. Fusero uses the p -matrix model described in section 2.2.3.4 [69, 70] to analyze responses of synchronous resonators. In addition to the calculation of the admittance matrix, the novelty of this library lies in the fact that it can be used for calculation of the amplitude of the acoustic waves within the device, the energy distribution along the filter, and S-parameters. It also takes into account the chirped periods and several acoustic mode. The application of the ohmic losses in this program allow the determination of the capacitive admittance matrix. The losses in the floating electrodes are assumed to be zero. Each elementary cell for this program is associated to the corresponding p -matrix for an individual cell, the electrode potential, the number of electrical connections of the electrode, This program takes into account different types of cells, and allows us to specify if it is in a transducer part, a reflector array, a chirp or it is a cell describing a metallized gap. It also allows us to specify whether it is a cell adjacent to a free surface gap, and the length of the free surface or the metallized gap, if any. An input file is used to describe the geometry of the transducer by specifying the pitch p , the metallization ratio $\frac{a}{p}$, the metallization thickness h , the acoustic aperture w , the cell type, the chirp type, and the free surface gap. Reduction of bus currents and reduction of the amplitude of the acoustic waves leaving the device are the two effects due to ohmic losses, that are considered in this program.

First the capacitance is calculated using Green's function to solve the electrostatic boundary value problem. The matrices of the bus acoustic admittances Y is calculated at each frequency point and a global admittance matrix is formed. To calculate the amplitudes of the acoustic waves within the device the value of the potentials is provided and this is managed by the routine `initPotPort`. The actual calculation is performed in the `acoustic-pow` routine. MatMixLib can also be used for the evaluation of the distribution of loads along the device. This is only possible when the static capacitance is calculated by BEM method. In this case, it is enough to call the routine `distributionCharges` after having given the value of the potentials imposed to the terminals of the device by the routine `initPotPort`.

2.2.4.1/ Computation of the global admittance matrix

The acoustic admittance matrix is obtained by cascading the elementary p -matrices of each electrode. J. Desbois has shown that this matrix of admittance is entirely determined by the electro-acoustic vectors and by taking into account the condition of conservation of the charge [69–71].

The P - matrix comprising N number of electrodes, given by equation 2.24 previously, in section 2.2.3.4, is written in the notations used by the program as

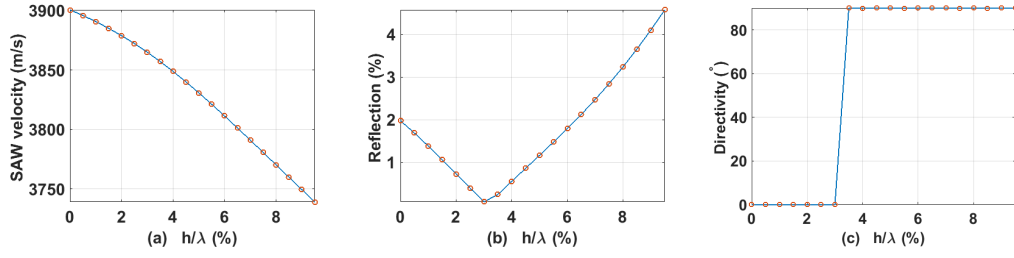


Figure 2.13: Plots showing a variation in (a) the SAW velocity, (b) $|\Delta|$ and (c) the directivity ($^{\circ}$), for a variation in $\frac{h}{\lambda}$ (%), for LiNbO₃ with cut(YXI) 128 $^{\circ}$.

$$\begin{bmatrix} S_G \\ S_D \\ \rho_I \end{bmatrix} = \begin{bmatrix} r_G & t & \rho_{a_G}^t \\ t & r_D & \rho_{a_D}^t \\ -\rho_{a_G}^t & -\rho_{a_D}^t & Y_a \end{bmatrix} \begin{bmatrix} E_G \\ E_D \\ \rho_V \end{bmatrix} \quad (2.31)$$

where E and S are the amplitudes of the waves entering and leaving the ports, subscripts G and D are the two acoustic ports, ρ_I is the current and ρ_V is the voltage at the electric port denoted by port 3. Y_a is the auto-admittance, i.e. admittance observed when no acoustic wave is incident, r_G and $-\rho_D$ are reflection coefficients, t is the transmission coefficient, and $-\rho_{a_G}^t$, $-\rho_{a_D}^t$, $-\rho_{a_D}^t$, and $\rho_{a_D}^t$ are transduction values for the respective ports. The acoustic admittance matrix for the upper triangular part (off diagonal) is deduced from the electro-acoustic vectors by:

$$Y_a = -\frac{1}{t} \rho_{a_D}^t \otimes \rho_{a_G}^t \quad (2.32)$$

with the tensor product \otimes defined by:

$$(\rho_a \otimes \rho_b)_{ij} = a_i b_j \quad (2.33)$$

the lower triangular part by condition of symmetry and the diagonal by conservation of the load is given by:

$$Y_{a,ij} = -\Sigma Y_{a,ik} \quad i \neq k \quad (2.34)$$

The total admittance matrix which is used subsequently to calculate the currents in the electrodes is the sum of the acoustic and capacitive admittance matrices:

$$Y = Y_a + Y_c \quad (2.35)$$

2.2.4.2/ The Grid

Once the geometric dimensions of the IDT are known, it is possible to determine the parameters of the acoustic waves which will propagate under the array of electrodes by means of a grid specific for a substrate material, designed for a semi-infinite structure. The grids used by MatMixLib to extract the values of different parameters for a specific device design geometry, have the format of the grids generated by Y. FUSERO [72]. This grid has nineteen columns that provide the values for a/p , h/λ (%), velocity (m/s), reflection (%), directivity ($^{\circ}$), real and imaginary parts of the conductance G (S), capacitance (pF/ μ m), relative permittivity ϵ , equivalent K^2 (%), $K^2 = \frac{2dV}{v}$ (%), etc. For a given metallization ratio ($\frac{a}{p}$) and the $\frac{h}{\lambda}$ parameter, the MatmixLib program selects the values for the parameters mentioned above to generate the admittance and the power responses for the device. The S-parameters can also be calculated.

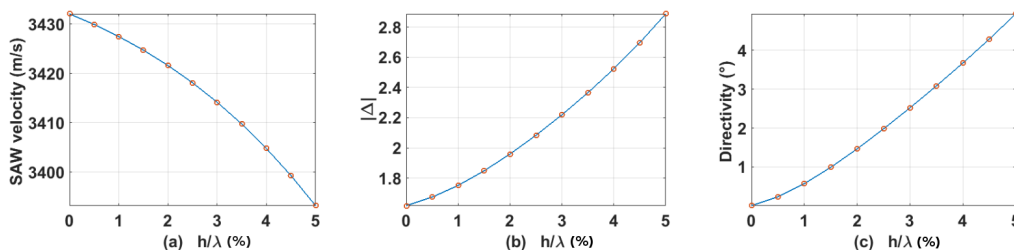


Figure 2.14: Plots showing a variation in (a) the SAW velocity, (b) $|\Delta|$ and (c) directivity ($^{\circ}$), for a variation in $\frac{h}{\lambda}$ (%), for LiNbO₃ with cut(YZ).

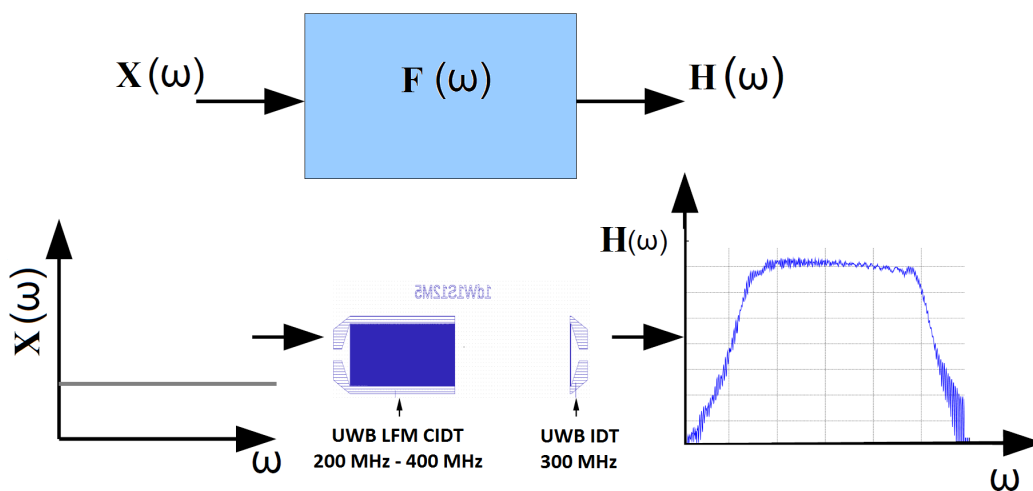


Figure 2.15: Measurement of the transmitted signal of the reference SAW device [74] using a network analyser.

For example, Figures 2.13 and 2.14, show the variation of some of the parameters (the SAW velocity, reflection coefficient (Δ) and directivity ($^{\circ}$), with respect to the variation in the $\frac{h}{\lambda}$, for a metallization ratio of 0.5, from the grid generated for LiNbO₃ with the cut (YXI) 128 $^{\circ}$, and LiNbO₃ with the cut(YZ) respecting the IEEE designation.

2.3/ Pulse compression

Pulse compression has been of interest for several decades in the past, especially in radar systems [73] as transmission of long pulses lead to an efficient use of the average power capability of the radar and reduced vulnerability of the system to interfering signals different from the transmitted signal. The duration of this pulse depends on the bandwidth of the signal. Larger the bandwidth, shorter is the pulse. This short pulse consists several frequency components with a precise phase relationship between them. A phase-distorting filter, can be used to introduce a relative change in phase to stretch a pulse. This expanded pulse is the pulse that is transmitted. A compression filter can be designed to match the phase distortion filter such that the phase of every frequency component is adjusted to produce a narrow pulse.

A SAW pulse compression device consists of an input IDT and an output IDT made of metal electrodes mounted on a piezoelectric substrate that offers the best electromechanical coupling

for the required SAW propagation. The piezoelectric substrate acts as the acoustic medium. The design of the input IDT defines the frequencies generated and determines the bandwidth of the signal. For example, in the SAW device described in section 2.2.2.2, the input IDT is the filter that generates a signal with modulated frequency or in other words, a chirp, when a voltage is applied to it. This transmitted signal is received by an UWB output IDT working in the same bandwidth range as the input IDT, as shown in figure 2.15. This transmission measurement $H(\omega)$, for an input signal $X(\omega)$, is used to design a filter that matches it. The response of this matched filter is fed to the SAW device to produce a short pulse. When the matched filter response $H^*(\omega)$ is a complex conjugate of the chirped IDT response, the short pulse response is given by the inverse Fourier transform of the product of the two signal spectrum $H(\omega)$ and the matched-filter response $H^*(\omega)$

$$P(t) = \frac{1}{2\pi} \int_{-\infty}^{\infty} |H(\omega)|^2 e^{i\omega t} d\omega \quad (2.36)$$

where $P(t)$ is the short pulse, ω is the angular frequency and t is time. $F(\omega)$ is the convolution function of the SAW device. In the time domain, the output signal $P(t)$ is the convolution product of the input signal $h^*(-t)$ and the transmission response $h(t)$ and is given by

$$P(t) = h(t) \otimes h^*(t) = \int_0^t h(\tau) \cdot h^*(\tau - t) d\tau \quad (2.37)$$

2.4/ Conclusion

In this chapter, a summary of different interferometer setups capable of ultrasonic vibration measurements, have been presented, exploring their working principles, advantages and limitations. Next, a discussion on some important ideas like piezoelectricity, SAW generation and propagation, and the concepts of inter-digital transducers and chirped IDTs (CIDTs), required for designing SAW devices, is presented. Different models for designing SAW devices have been reviewed. The program MatMixLib, used to simulate the responses of the CIDTs, and the grid used to obtain the design parameters for the SAW device, have been described, followed by a short discussion on the principle of pulse compression. All these concepts have been used in the following chapters to implement the generation and compression of SAW pulses.



CONTRIBUTION

Chirped inter-digital transducers

3.1/ Inter-digital transducer modelling

A grating structure serves as the most fundamental element of inter-digital transducers (IDTs). IDTs are used for excitation and detection of surface acoustic waves (SAW) in ultra wide band (UWB) SAW devices. Reflections on the metal fingers greatly affect the functionality of IDTs, and thus that of the SAW devices they are used in. Hence, this effect has been studied extensively and several models and theories have been proposed for this purpose. The signal properties of IDT devices can be controlled by varying several parameters like the number of fingers (electrodes) of the IDT or the spatial distribution of the pitch p of the array of fingers. Here, we wish to study the generation and propagation of SAW inside a chirped IDT (CIDT) described in chapter 2, section 2.2.2.2. Two different models are used to estimate the response for each of three differently chirped SAW devices, consisting an input IDT with 300 electrodes and an output IDT with 4 electrodes, both IDTs spaced at a distance $d = 2066 \mu\text{m}$ with a constant acoustic aperture of $800 \mu\text{m}$, a metallization ratio $\eta = 0.5$, and each wavelength is represented by a single pair of electrodes, where $p = \frac{\lambda}{2}$.

The chirped IDTs designed and fabricated are bidirectional and up-chirped, previously described in section 2.2.2.2. A comparison of the responses of these devices, and a reference sample described in section 3.2, which is apodized and down-chirped, is presented in this chapter. Of special interest is the appearance of band gaps inside the CIDT that can enhance the SAW emission in one direction.

3.1.1/ Material selection and design parameters

The SAW propagation in lithium niobate (LiNbO_3) is well studied as this material is one of the most widely used in acoustic applications as it has a very high dielectric constant and piezoelectric coefficient. This material is ferroelectric and is grown by the Czochralski method [75]. LiNbO_3 YX 128° rotated is selected as a piezoelectric material for the SAW device design as it gives a high electromechanical coupling coefficient $K^2 = 0.054$ for surface acoustic wave generation and good temperature sensitivity $70 \text{ ppm}/^\circ\text{C}$ for practical fabrication purposes. It is also cost effective for large scale production of SAW devices.

Every electrode pair converts a portion of the electrical energy into mechanical energy. The contribution of each pair of electrodes is added coherently. A certain number of electrode pairs (N_{max}), given by

$$N_{max} = \frac{\pi Q_t}{2 \frac{\delta v}{v}} = \frac{\pi Q_t}{K^2} \quad (3.1)$$

is required to obtain the best performance of a transducer [55]. If the number of electrode pairs is less than that then the transducer does not operate at optimum capabilities. However, if we have a larger number of electrodes, a cumulative increase in internal reflections can effect the operation of the transducer and its efficiency adversely.

In equation 3.1 Q_t is the normalized quality factor based on the electrode architecture, $2 \cdot \frac{\delta v}{v}$ is the ratio of the relative variation of velocity between free and metallized surfaces. This equation is valid only for IDTs with a single period. For a transducer with a metallization ratio of $\eta = 0.5$, the standardized Q_t factor is about 0.348 [55]. In the case of LiNbO₃ YX-128, the coupling coefficient is $K^2 = 0.054$ and the maximum number of pairs is then calculated to be

$$N_{max} \approx \frac{1}{K^2} = \frac{1}{0.054} \approx 20. \quad (3.2)$$

This is by induction the ideal number of pairs active per frequency in a CIDT. For detection purposes we also need an IDT without dispersion. In order to measure a short pulse we need an ultra wide band transducer. The bandwidth of a standard *UWB* transducer depends on the number of electrode pairs. The number of electrode pairs is inversely proportional to the bandwidth. The standard transducer used as a reference in this work, and for the samples to be designed, has a bandwidth $\Delta f = 200$ MHz and a central frequency $f_c = 300$ MHz, hence the number of electrode pairs N_{UWB} is calculated as

$$N_{UWB} \approx \frac{f_c}{\Delta f} = \frac{300 \text{ MHz}}{200 \text{ MHz}} = 1.5. \quad (3.3)$$

This means that no more than three electrodes should be used. The distance between the electrodes depends on the operating frequency and on the velocity of the waves propagating along the piezoelectric substrate. In order to calculate the distance between the electrodes, i.e., the pitch p , the wave velocity on the free surface of LiNbO₃ YX-128 used is 3979 m/s. Although this speed value of propagation is not accurate because it is modified by metallized surfaces, accuracy remains sufficient for a UWB transducer.

λ is the wavelength, given by

$$\lambda = \frac{c}{f} \quad (3.4)$$

where c (m/s) is the SAW velocity used, and f is the desired frequency. The pitch $p = \frac{\lambda}{2}$ for the CIDT is calculated to be 9.94 μm and 4.97 μm to obtain a chirp with a frequency range of 200 MHz - 400 MHz. The pitch for the output IDT is calculated to be 6.631 μm .

The relative metallization (h/λ), where h is the thickness of the metal electrodes, and the metallization ratio ($\eta = \frac{a}{p}$), where a is the width of each electrode, are the two parameters that influence the reflectivity of the electrodes and consequently affect the final response of the IDT. These two parameters make it possible to minimize the reflectivity of the electrodes in order to limit parasitic reflections in the transducer. The deposition of aluminium electrodes for the SAW devices presented in this thesis is carried out in a single step, hence, there is no variation in the metallization thickness h in the SAW device. To minimize the reflectivity of the transducer electrodes and have a metallization ratio of $\eta = 0.5$ so as not to have a low coupling coefficient, (h/λ) was chosen to be 0.05 and the thickness h was calculated to be

$$h = 0.05 \frac{c}{f_c} = 0.05 \cdot \frac{3979 \text{ m/s}}{300 \text{ MHz}} \approx 640 \text{ nm}. \quad (3.5)$$

An acoustic aperture $w = 800 \mu\text{m}$ was chosen to have an impedance of $\approx 50 \Omega$ for the SAW device.

When an elastic wave propagates on a free surface, its amplitude diminishes during propagation through different loss mechanisms (heat, mechanical effects). These losses are known as propagation losses on the free surface and are represented by the propagation loss factor α in [dB/ μs]. Since most of the propagation loss comes from the transformation of mechanical energy into heat (interactions with thermal phonons), the higher the frequency, the greater the losses. As the waves move the atoms of the piezoelectric substrate, the vibrating atoms transforms some of the acoustic energy to heat. For LiNbO₃ YX-128, at an ambient temperature of 25°C, the losses are estimated from the empirical formula for losses in the LiNbO₃ YZ [55] given by

$$\alpha = 0.19f_0 + 0.88f_0^2 = 0.19(0.3) + 0.88(0.3)^2 = 0.14 \frac{\text{dB}}{\mu\text{s}}. \quad (3.6)$$

where the coefficient 0.19 expresses the attenuation of the amplitude of the wave in air, the coefficient 0.88 expresses the attenuation of the amplitude of the wave by thermal effect and the central frequency f_0 for our design is 0.3 GHz. Propagation loss α_m on the metallized electrodes is calculated using the empirical formula [55] given by

$$\alpha_m = K \cdot f_0^2 \quad (3.7)$$

where, for a standard IDT, the empirical coefficient $K = 5.2$ (%) for the thickness of an aluminium deposition of 200 nm. However, for small transducers, the propagation loss on the metallization electrodes can be neglected.

For a linear frequency modulation (LFM) the phase varies quadratically, allowing the frequency f to vary linearly [55]. In this work, though the chirps are designed differently as described in section 3.1.2, we calculate the required number of electrode pairs N to obtain the optimal signal and use this parameter to design the chirps and study their response. The autocorrelation of the LFM signal makes it possible to obtain a compressed pulse and improves the signal-to-noise ratio. By increasing the processing gain G , defined by

$$G = B \cdot T, \quad (3.8)$$

allows us to obtain a good signal-to-noise ratio.

The greater the product of the bandwidth B and the interrogation time T , the better the signal-to-noise ratio [55] for a certain range of values. In the case of a high piezoelectric coefficient, the processing gain for a SAW device should be ≤ 1000 for the equation 3.8 to be valid [74]. In order to easily realize a prototype and due to technological constraints, a gain of 100 is used with a bandwidth of 200 MHz, which gives an interrogation signal with a duration of 500 ns as calculated in equation 3.9, corresponding to a transducer length of 2 mm on LiNbO₃ YX-128.

$$T = \frac{G}{B} = \frac{100}{200 \cdot 10^6 \text{ [Hz]}} = 500 \text{ ns}. \quad (3.9)$$

The number of electrode pairs N in the IDT depends on the frequency and the duration of the interrogation signal. For a duration of 500 ns and a frequency range of 200 MHz - 400 MHz,

$$N = f_c.T = 300.(10^6)[Hz].500 \text{ ns} = 150. \quad (3.10)$$

The parameter values obtained in this section are used to simulate the responses for different chirps obtained in the following sections.

3.1.2/ The delta function model

The simplest model of an IDT is the delta function model as described in section 2.2.3.1. In spite of several limitations to this model, it is still a very good tool for a preliminary and fast estimation of an IDT response. A major disadvantage of this model is that frequency responses of input and output IDTs cannot be separated when both IDTs are apodized and in-line [54], however, for our chirp IDT designs, we do not use apodization hence this does not affect our results. In this model, each electrode finger pair is considered as a periodic wave source. When voltage is applied to the n^{th} pair, the voltage on all the other finger pairs are assumed to be zero. The superposition of the periodic waves from all the finger pairs forms the final response of the IDT. The charge distribution on the electrodes is approximated by δ -functions located at the center of the spaces in between the electrodes. The spatially-distributed delta function contributions may be summed at a convenient reference point along the x-axis. The frequency response of this model is given by

$$u(f) = \sum_{n=1}^N a_n \exp(-2i\pi f(x_0 - x_n)/\nu) \quad (3.11)$$

where ν is the surface wave velocity, f is the frequency, x_0 is the initial position of the output IDT assuming the starting position of input IDT to be at $x = 0$, x_n is the n^{th} position within the IDT depending on the variation of the pitch, n is the number of fingers per acoustic period (2 for our case) and a_n is the amplitude parameter proportional to the finger overlap or in other words, the acoustic aperture. Matlab is used to simulate different kinds of chirp in order to study the effects on the short pulse waveform of the surface acoustic wave. An input with a source strength of unit amplitude is sent through the input IDT. The delta function model cannot furnish information on harmonic performance and IDT finger reflections, there is no special significance in employing a metallization ratio $\eta = 0.5$ and hence, is not used as a parameter for this model. The bidirectional nature of the IDTs is not taken into account in this model. In case one, the pitch of the chirped IDT is varied linearly along the length of the IDT and is given by

$$p_n = p_{n-1} + \frac{p_{max} - p_{min}}{N} \quad (3.12)$$

where, p_n is the n th pitch value, p_{max} is the maximum pitch, p_{min} is the minimum pitch and N is the total number of IDT fingers. The resulting chirp has an uneven distribution of amplitude along the desired bandwidth, i.e., 200 MHz – 400 MHz .

In the second case the pitch is varied inversely to obtain a hyperbolic chirp and is given by

$$p_n = \frac{1}{\frac{1}{p_{n-1}} + \frac{n-1}{N-1} \frac{1}{p_{max}-p_{min}}} \quad (3.13)$$

In the third case, the pitch is varied as mean of linear and inverse chirps and is given by

$$p_n = \frac{p_{linear} + p_{inverse}}{2} \quad (3.14)$$

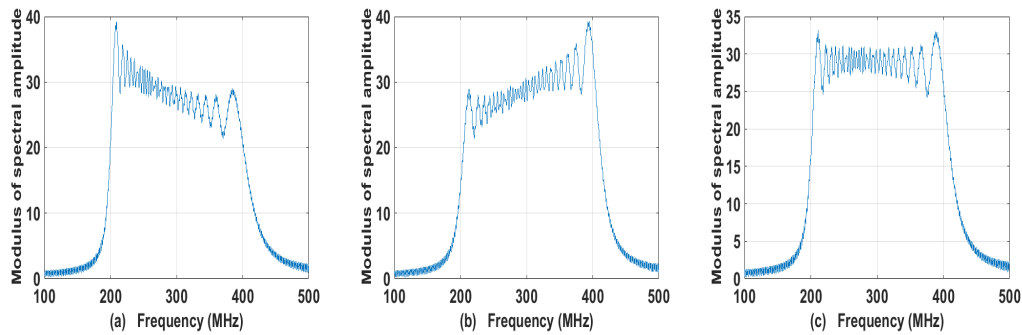


Figure 3.1: Modulus of the spectral amplitude (in arbitrary units) for (a) a linear chirp, (b) a hyperbolic chirp and (c) a mean chirp, obtained using a delta function model.

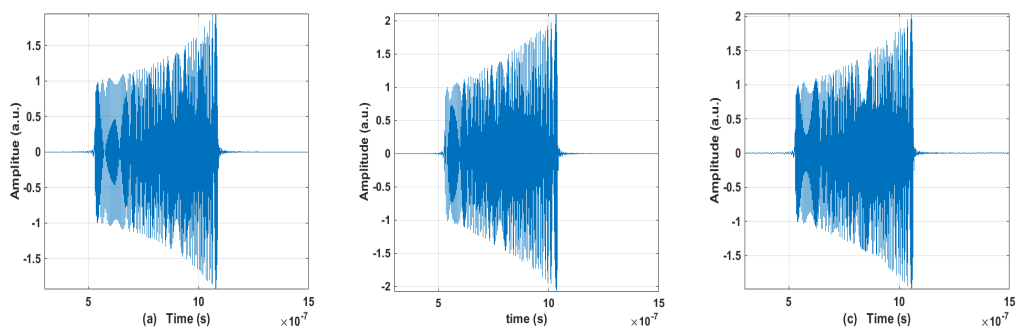


Figure 3.2: Waveforms (amplitude in arbitrary units) obtained for (a) a linear chirp, (b) a hyperbolic chirp and (c) a mean chirp, obtained using a delta function model.

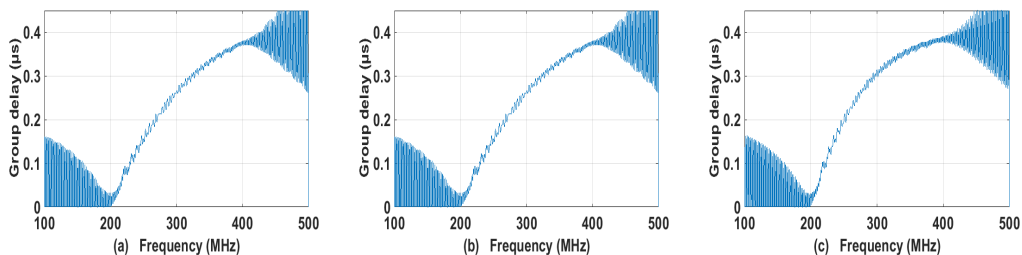


Figure 3.3: Group delay of the CIDT response obtained for (a) a linear chirp, (b) a hyperbolic chirp and (c) a mean chirp, obtained using a delta function model.

The three different types of chirps simulated using this model and the waveforms obtained using Fourier transform for each of them are shown in Fig. 3.1 and Fig. 3.2. For the first case, even though the pitch varies linearly, the amplitude is not observed to be constrained to a flat topped chirp profile. The chirp spectrum as seen in Fig. 3.1(a), is found to have a sloped profile with higher frequencies showing lower amplitude along the desired bandwidth, i.e., 200 MHz - 400 MHz. For the hyperbolic case, the sloped chirp profile is exactly the opposite of what is obtained for the linear case, with higher frequencies showing higher amplitude for the desired bandwidth, as seen in Fig. 3.1(b). In the third case, a flat topped chirp profile is obtained with the amplitude distribution being fairly uniform across the desired bandwidth as seen in Fig. 3.1(c), and hence has the best response among the three cases.

A measure of the group delay (in seconds) is important to evaluate the performance of an

electrical device (in our case, a SAW device). When a chirp is sent through a device and is expected to be the same when received, it is important to ensure that the device it passes through does not cause any distortion of the frequency components, which implies that every frequency component must reach at the same time resulting in the group delay to be constant for the chirp bandwidth. Any form of phase misalignment can affect the output signal hence it is important that all frequency components experience the same amount of delay (in seconds, not phase angle) as they pass through a device. A negative of the rate of change of phase ϕ , with respect to the frequency ω , for each chirp, or in other words, the group delay τ is calculated using equation 3.15

$$\tau = -\frac{d\phi(\omega)}{d\omega} \quad (3.15)$$

Fig. 3.3 shows the calculated group delay for the three different chirps obtained using the delta function model. It is observed that the group delay is not constant for the three chirps.

For this SAW filter design, the maximum attainable time (group) delay is proportional to the separation distance d between the input and the output IDTs. For our devices, the separation distance d is set to 2066 μm , and is expected to give a delay of 500 ns for a SAW velocity of 3979 m/s on LiNbO₃ YX cut 128 degrees rotated. However, the maximum group delay obtained for the three chirps is ≈ 400 ns. This model is fairly limited in its response estimations as it does not take into account internal reflections and dispersion effects, hence a p-matrix model is used to obtain a more accurate response.

3.1.3/ The p-matrix model

The MatMixLib program constructed by C. De Sena, T. Pastureaud and Y. Fusero that employs the p-matrix model described in Chapter 2, section 2.2.3.4, is used to simulate three different types of chirps described in section 3.1.2, for SAW devices with aluminium electrodes on LiNbO₃ YX 128°. The SAW velocity 3979 m/s used in section 3.1.2 with a pitch range 4.97 μm - 9.9 μm , and does not yield a frequency range of 200 MHz - 400 MHz for this model as it takes reflections and other second order effects. The SAW velocity used is 3895.64 m/s and the adjusted pitch range used is 4.6 μm - 9.94 μm . The coupling coefficient is $K^2 = 0.05$. The metallization ratio $\eta = 0.5$ is used. Due to technological restrictions for the fabrication process described in section 3.3, the deposition thickness for aluminium electrodes h , used for simulating the response using this model is 200 nm. The amplitude spectrum in the frequency domain, the waveforms, and the group delay for the respective chirps are plotted in Figures 3.5 and 3.6.

A significant variation in the frequency response for the different chirps can be observed in Figure 3.4 when compared to the simulation results obtained for the respective chirps, using the delta function model described in section 3.1.2. The response for the linear chirp as observed in Figure 3.4(a) is also linear in frequency (flat topped), obtained without incorporating any additional apodization to get amplitude weighting which is essential for a general LFM chirp [55], to obtain a flat topped response unlike the response obtained using the delta function model. The hyperbolic and mean chirps as seen in Figures 3.4(b) and (c), both have sloped chirp profiles with higher frequencies showing higher amplitude for the desired bandwidth. The chirp profile of the mean chirp is less sloped and the energy distribution along the band width is better compared to the hyperbolic chirp. However, total power for the hyperbolic chirp is better than the other two cases.

For our devices, the group delay results shown in Figure 3.6 are obtained at the last electrode of the CIDT, hence d in this case is considered to be the length of the CIDT, and is 2178 μm

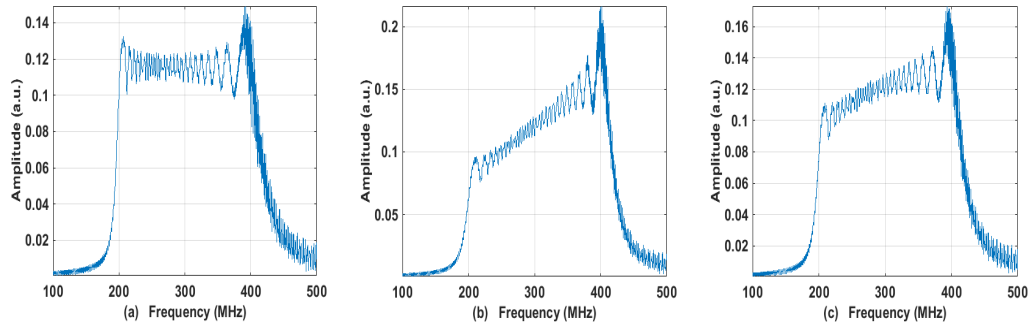


Figure 3.4: Modulus of the spectral amplitude for (a) a linear chirp, (b) a hyperbolic chirp and (c) a mean chirp, obtained using a p-matrix model.

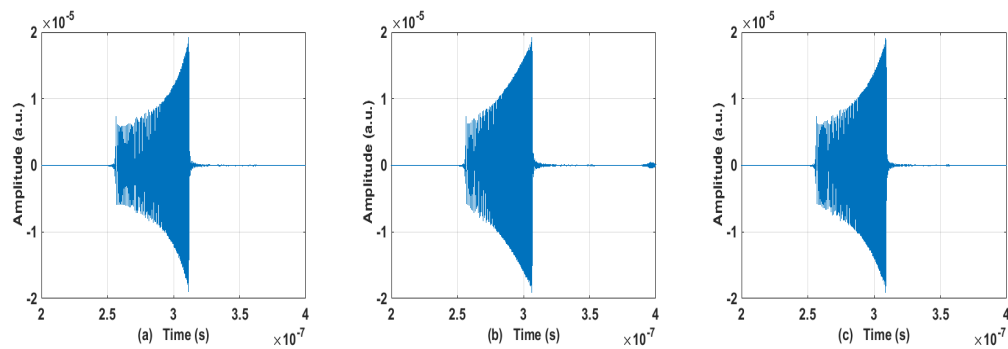


Figure 3.5: Waveforms obtained for (a) a linear chirp, (b) a hyperbolic chirp and (c) a mean chirp, using a p-matrix model.

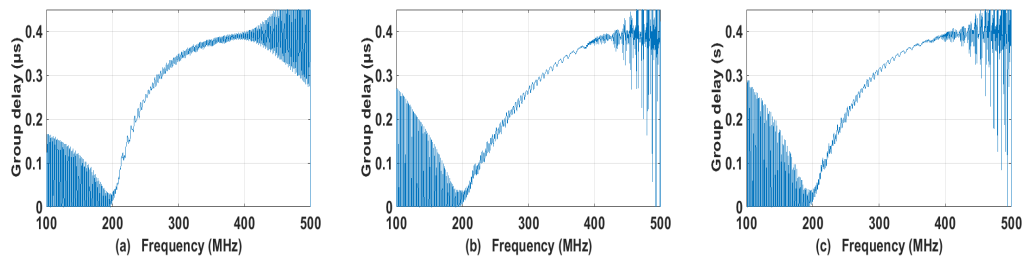


Figure 3.6: Group delay obtained for (a) a linear chirp, (b) a hyperbolic chirp and (c) a mean chirp, using a p-matrix model.

for this model, They are expected to give a delay of 550 ns for a SAW velocity of 3985.64 m/s on LiNbO₃ YX cut 128 degrees rotated. However, the maximum group delay obtained for the three chirps is 400 ns for all three cases.

3.2/ Reference sample

The reference sample was designed and fabricated in FEMTO-ST, Besançon, France, by Marc Lamothe, as described in section 2.2.2.2, according to the design parameters mentioned in section, 3.1.1. To minimize the reflectivity of the transducer electrodes, $\frac{a}{p} = 0.5$ and $\frac{h}{\lambda} = 0.05$ were chosen as optimum values for fabrication of the reference sample. The metallization

thickness used is $h=154.7 \pm 2.8$ nm. The reflection and transmission responses of this sample is shown in Fig. 3.7. This sample has a linear frequency chirp (LFM), with an down-chirp CIDT.

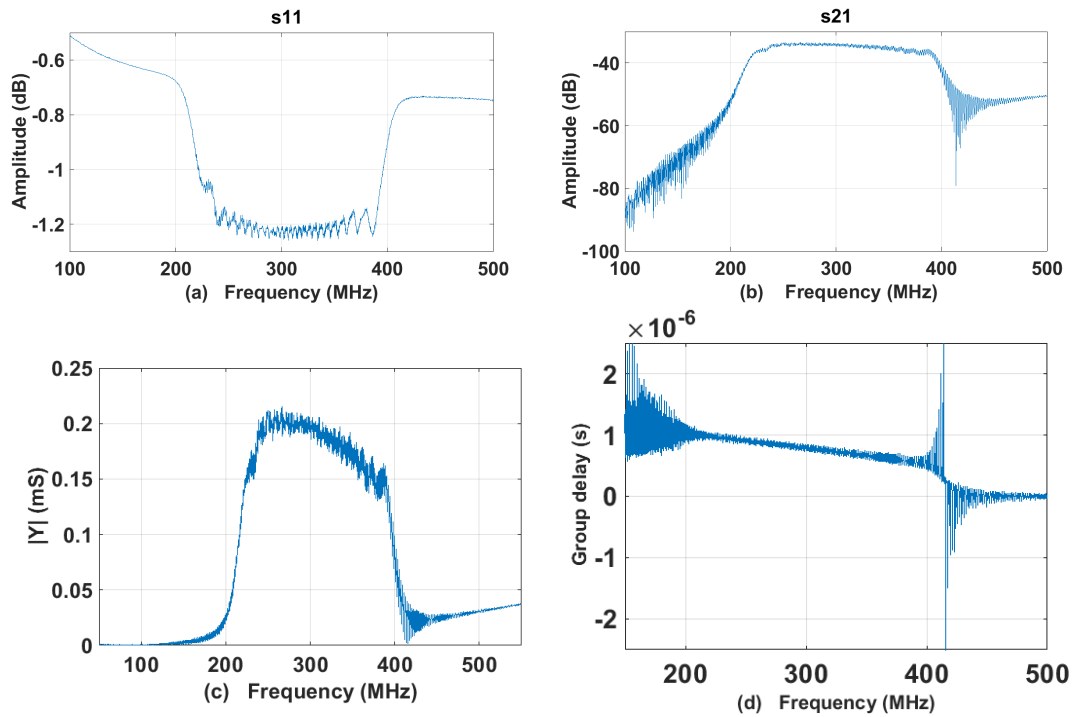


Figure 3.7: (a) S11 measurement (b) S21 measurement (c) admittance measurement and (d) group delay measurement of the reference sample

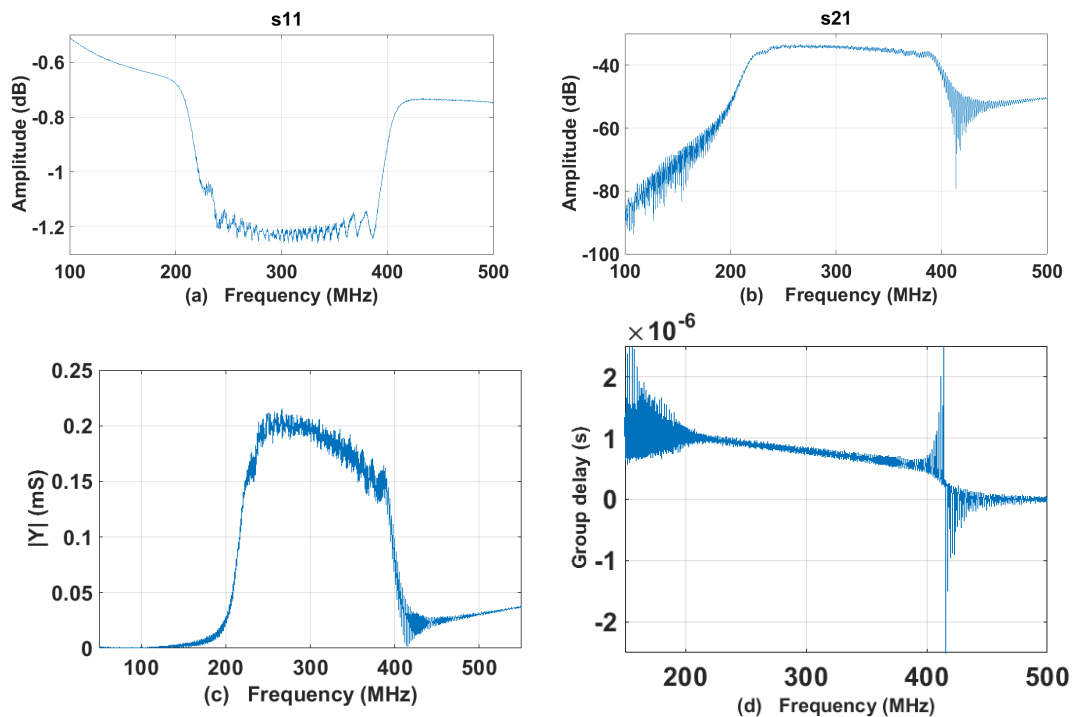


Figure 3.8: (a) S11 measurement (b) S21 measurement (c) admittance measurement and (d) group delay measurement of the reference sample with a metal plate.

Table 3.1: Reference SAW device specifications.

Substrate	Lithium niobate Y 128°
propagation direction	X
Pitch range of the CIDT	4.71 μm – 9.39 μm
Pitch range of the Output IDT	6.4 μm
SAW velocity	3768 m/s
Thickness	178 \pm 2.6 nm
Finger width	$\frac{1}{4}\lambda$
Acoustic aperture	800 μm
Distance between input and output IDT	2066.32 μm
Number of CIDT fingers	300

For a LFM chirp as described in section 2.2.2.2. When the central frequency is larger than 20% of the bandwidth, wave propagation is better for the higher frequencies, hence, apodization, or in other words, variation in the acoustic aperture along the chirp axis, is added to the input IDT to select the active area of the electrodes, which allows us to shape the waveform of the signal generated. This leads to a uniform distribution of the acoustic energy along the entire bandwidth and gives a flat topped chirp profile where the amplitude variation with respect to frequency is minimal. The specifications of the reference sample are given in table 3.1.

The reflectivity of the substrate compared to the metal electrodes is very low hence an aluminium plate with a thickness of 200 nm is deposited between the two IDTs on the SAW device. This allows us to obtain a better signal measurement within the SAW device using the differential interferometer described in section 4.2. The design specifications for this sample remains the same as the reference sample. The reflection and transmission responses of this sample is shown in Fig. 3.8. No significant difference is observed in the responses of the reference SAW device after the deposition of the metal plate on it.

3.3/ Fabrication

The geometric parameters of the SAW device designs for the different chirps, used for simulating the response using the p-matrix model as described in section 2.2.3.4 and 3.1.3, are used for the fabrication process.

3.3.1/ Material selection

Lithium niobate is an anisotropic material which is highly pyroelectric. Repeated heating and cooling of this material results in charge accumulation causing spontaneous electrical discharge during the fabrication process and between metallized electrodes on the substrate. Pyroelectric discharging makes fabrication of wafers and SAW devices extremely difficult. It may even cause substrate damage. This may result in SAW devices generating a noisy response and may even damage other circuit components. In order to avoid these difficulties, black lithium niobate is used for fabricating the SAW devices. Since, black lithium niobate is obtained by chemically treating the wafer at elevated temperature in an environment of nitrogen and hydrogen, it

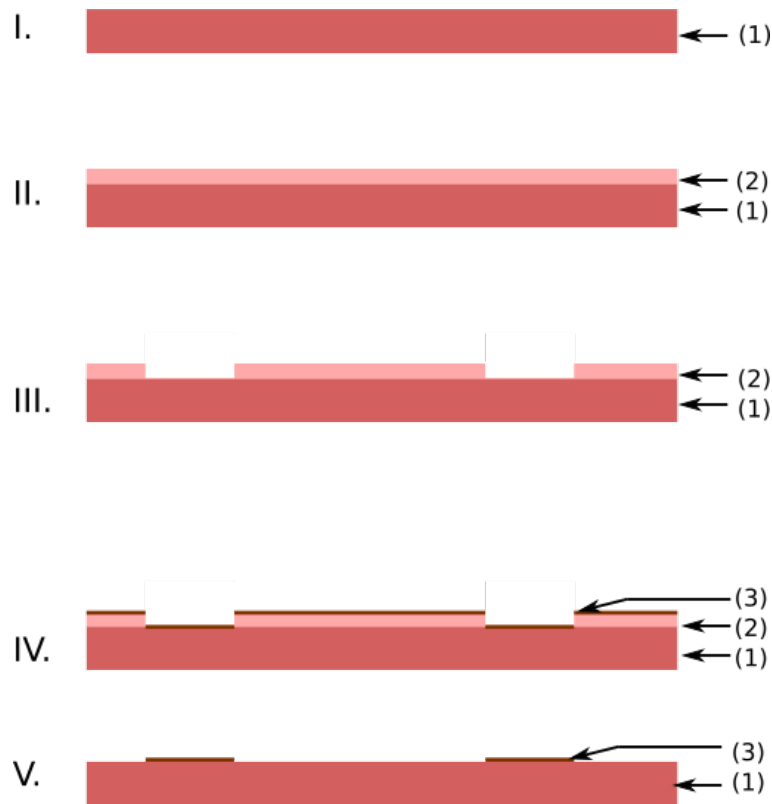


Figure 3.9: A schematic of the lift-off process that is used for fabricating the SAW devices where layer (1) is the substrate (LiNbO_3), layer (2) is the photo resist and layer (3) is the metal (aluminium) deposited on the substrate. Steps of the lift-off process : (I) substrate prepared for lithography, (II) photoresist added on the substrate, (III) the SAW design deposited using photo-lithography with a negative mask, (IV) metal deposited by evaporation, and (V) lift-off completed by cleaning the resist and removing the unwanted metal deposited on the substrate.

substantially increases electrical conductivity, and effectively eliminates the pyroelectric effect. The transducer static capacitance and the SAW transduction coupling strength is the same for both, the black and regular LiNbO_3 . Aluminium is chosen for the metallization because its acoustic impedance matches closely to that of lithium niobate.

3.3.2/ Lithography and Deposition

The lift-off process used for the fabrication of the SAW devices is shown in figure 3.9. A mask design with a negative polarity is prepared using Cadence (a CAD software) for different types of SAW devices with the dimensions of the IDT parameters obtained using the p-matrix model. Each device comprises of a chirped input IDT and an output IDT like the reference sample. For the same pitch values and acoustic aperture, the input IDT is chirped in three different ways (linear, hyperbolic and mean of both) with and without a metal plate between the 2 IDTs. Ti Prime is used as an adhesion promoter on a four inch black LiNbO_3 wafer fabricated by Roditi international. It is spin coated on the substrate to improve resist adhesion. An image reversal photoresist Ti09 is used to perform a lift off photolithography process. The photoresist profile of the design is shown in Fig. 3.10. This is followed by aluminium deposition using the evaporation technique. Details of the lithography process are given in Table 3.2.

Table 3.2: Specifications of the Lithography process

Step 1	Spin coating Ti Prime
	Speed 3500 m/s
	Acceleration 1100 rpm
	Time 30 s
Step 2	Oven baking
	Temperature 100°C
	Time 6 minutes
Step 3	Spin coating TiO ₂
	Speed 1100 m/s
	Acceleration 1000 rpm
	Time 20s
Step 4	Oven baking
	Temperature 100°C
	Time 6 minutes
Step 5	UV exposure
	Energy 80 mJ/cm ²
Step 6	Oven baking
	Temperature 130°C
	Time 6 minutes
Step 7	UV exposure
	Energy 130 mJ/cm ²
Step 8	Photoresist development
	Time 90 s

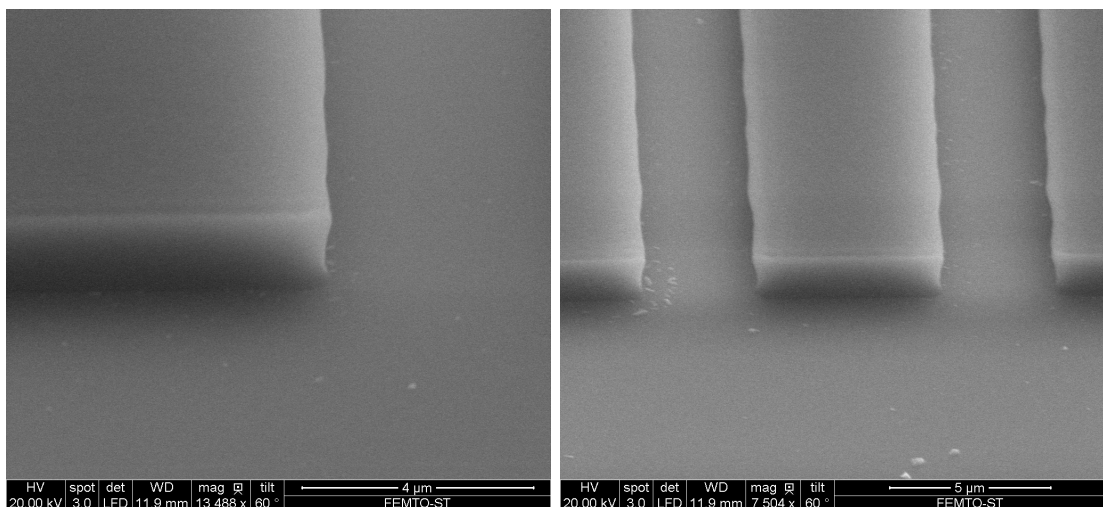


Figure 3.10: SEM images showing the photoresist profile of the designed electrodes at the end of the lithography process.

3.4/ Results and discussion

Unlike the reference sample, in this set of fabricated SAW devices the chirped IDTs do not have any apodization and each wavelength is represented by a single pair of IDT fingers. This allows us to study the effects of the internal reflections within the chirped IDT, on the device response. The geometric parameters of the design, measured for the fabricated devices are given in Table 3.3. SEM imaging is used to characterize the geometry of the fabricated devices. The pitch measurements for the IDTs on the device are shown in Fig. 3.11. The variation in the geometric dimensions of the designs for the three chirps are minimal. Figure 3.12(a) shows one of the fabricated SAW devices with a hyperbolic CIDT. It is wire bonded on a PCB as shown in figure 3.12(b) and is well grounded to minimize the noise in the measured signal.

The S parameters of the different fabricated devices are measured using a probe tester and are shown in figures 3.13, 3.14, and 3.15. The differences in the response for the three different chirps are clearly visible in figures 3.13(a), 3.14(a), and 3.15(a). The hyperbolic chirp profile seen in fig 3.14(a), is better as the energy distribution along the bandwidth is fairly uniform and the chirp profile is less sloped compared to the linear and mean chirp measurements shown in figures 3.13(a) and 3.15(a). Unlike the reflection measurements, we don't observe any significant variation in the chirp profiles of the transmission measurements for the different chirps, shown in figures 3.13(b), 3.14(b), 3.15(b). The amplitude for all three chirps range from -60 dB to -50 dB for the desired bandwidth. The measured transmission responses are not completely consistent with the simulation results. The possible reason could be that the

Table 3.3: Design parameters used for the fabricated SAW devices.

Substrate	Black lithium niobate Y 128°
propagation direction	X
Pitch range of the CIDT	$\approx 4.6 \mu\text{m}$ to $9.9 \mu\text{m}$
Pitch range of the Output IDT	$6.4 \mu\text{m}$
Thickness	$200 \pm 6.4 \text{ nm}$
Finger width	$\frac{1}{4}\lambda$
Acoustic aperture	$800 \mu\text{m}$
Distance between input and output IDT	$2066.32 \mu\text{m}$
Number of fingers	300

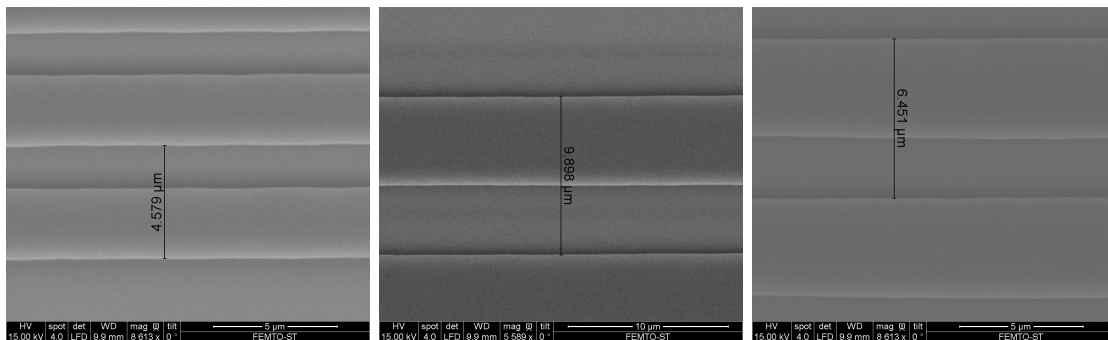


Figure 3.11: SEM images of a linearly chirped input IDT showing (a) the minimum pitch, (b) the maximum pitch, and (c) a SEM image with the pitch measurement of the output IDT.

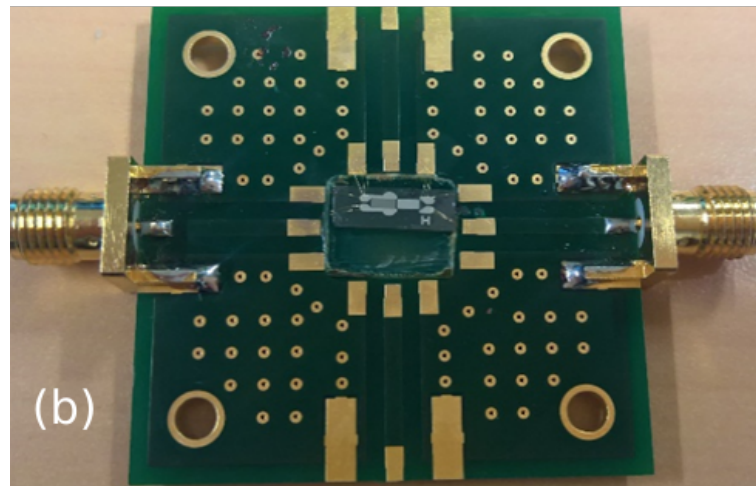


Figure 3.12: (a) An image of a fabricated SAW device with a hyperbolic chirp IDT after dicing and (b) a picture of the SAW device wire-bonded on a PCB.

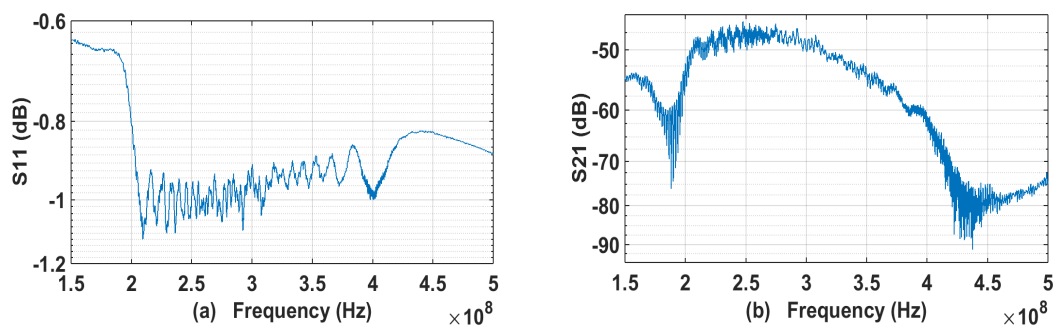


Figure 3.13: (a) S11 measurement and (b) S21 measurement of the SAW device with a linearly chirped IDT fabricated using the specification mentioned in Table. 3.3. The chirp bandwidth is 200 MHz - 400 MHz.

number of electrodes in the output IDT (2 pairs) is not sufficient to measure the response accurately.

Figure 3.16(a), 3.16(b) and 3.17 show a comparison between the conductance, susceptance and admittance measurements for the three chirps. The SAW devices with linear and hyperbolic CIDs, have similar responses in terms of amplitude and signal profile. The response for device with the mean CID is noisy. The maximum admittance amplitude in this case is ≈ 0.01 S, which is much lower compared to that of the other two cases which is ≈ 0.02 S, almost double

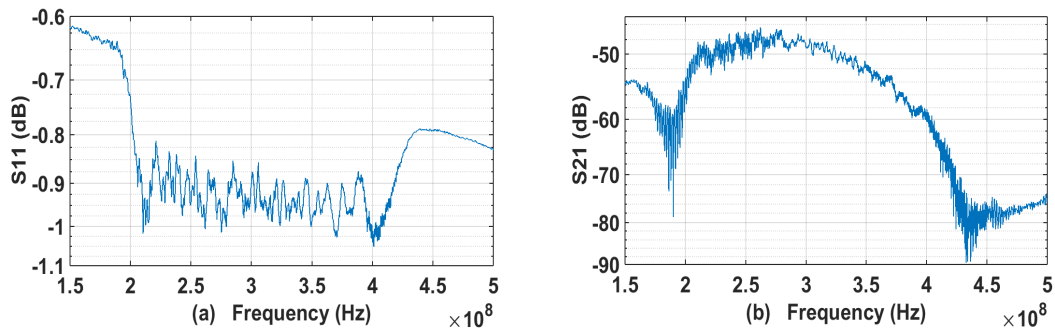


Figure 3.14: (a) S_{11} measurement and (b) S_{21} measurement of the SAW device with a hyperbolically chirped IDT fabricated using the specification mentioned in Table. 3.3. The chirp bandwidth is 200 MHz - 400 MHz.

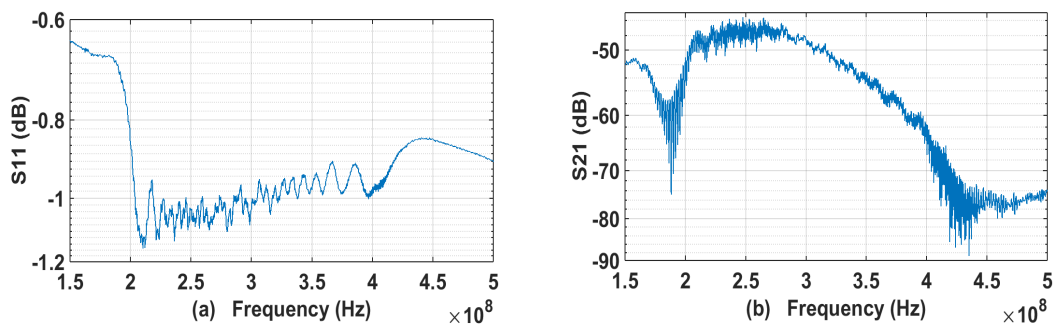


Figure 3.15: (a) S_{11} measurement and (b) S_{21} measurement of the SAW device with a mean chirped IDT fabricated using the specification mentioned in Table. 3.3. The chirp bandwidth is 200 MHz - 400 MHz.

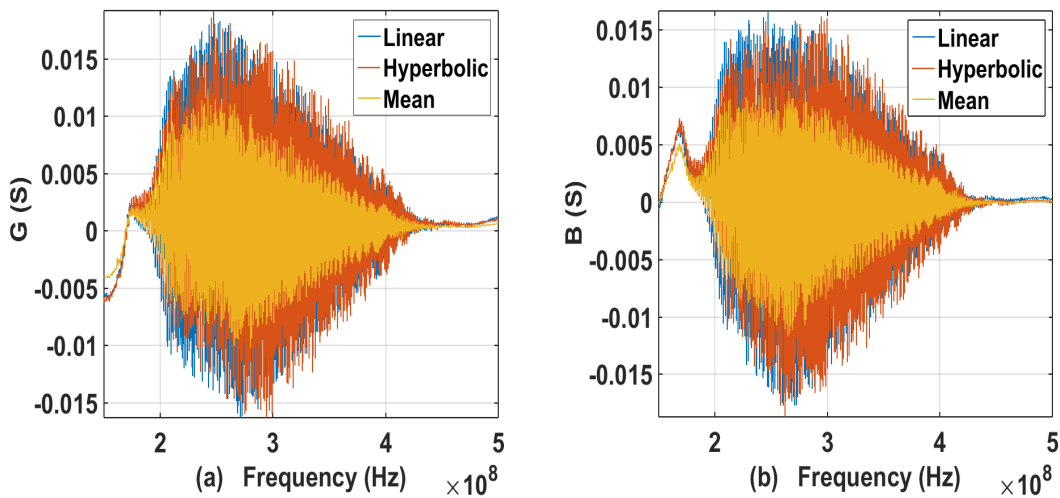


Figure 3.16: A comparison between the (a) conductance and (b) susceptance of the SAW device responses with the three differently chirped IDTs, fabricated using the specification mentioned in Table. 3.3. The chirp bandwidth is 200 MHz - 400 MHz.

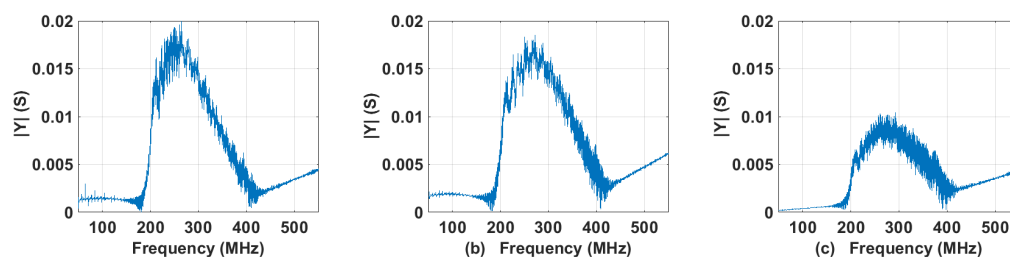


Figure 3.17: Admittance measurements for the transmission, obtained from the fabricated SAW devices with (a) a linear chirp, (b) a hyperbolic chirp and (c) a mean chirp. The chirp bandwidth is 200 MHz - 400 MHz.

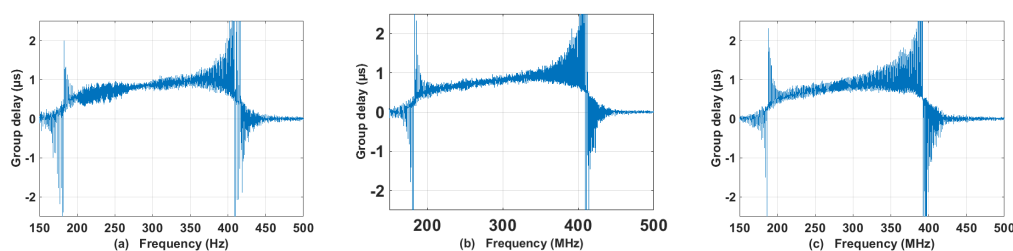


Figure 3.18: Group delay measurements, obtained from the fabricated SAW devices with (a) a linear chirp, (b) a hyperbolic chirp and (c) a mean chirp. Chirp bandwidth is 200 MHz - 400 MHz.

of the amplitude of the mean chirp.

The group delay measured for the three devices is shown in fig 3.18. For all three cases, as the CIDTs are up-chirped, the group delay is larger for high frequencies compared to that of the low frequencies and show an inverse group delay dispersion compared to the group delay of the reference sample shown in figure 3.7 (d). The group delay varies within the desired bandwidth of 200 MHz - 400 MHz by ≈ 550 ns. For a separation distance $d = 2066 \mu\text{m}$, the SAW velocity is calculated to be ≈ 3756.4 m/s. The measurements are consistent with the simulation results obtained using the delta function model, shown in figure 3.3, and the p-matrix model, shown in figure 3.6.

3.5/ Appearance of band gaps

In case of bidirectional IDTs, it is known that, SAWs are excited toward both right and left directions and both responses are expected to be the same by reciprocity, in theory. However, it is not always the case. For a single period grating, strong reflections occur at the Bragg frequency, at which λ is equal to $2p$, assuming no bulk wave excitation. With an increase in the number of electrodes these reflections get stronger, resulting in a band gap formation. Such a phenomenon has been reported previously e.g in grating based Surface Plasmon generation studies [76].

The dispersion [77] relation in the p-matrix theory, for an infinite number of electrode pairs is

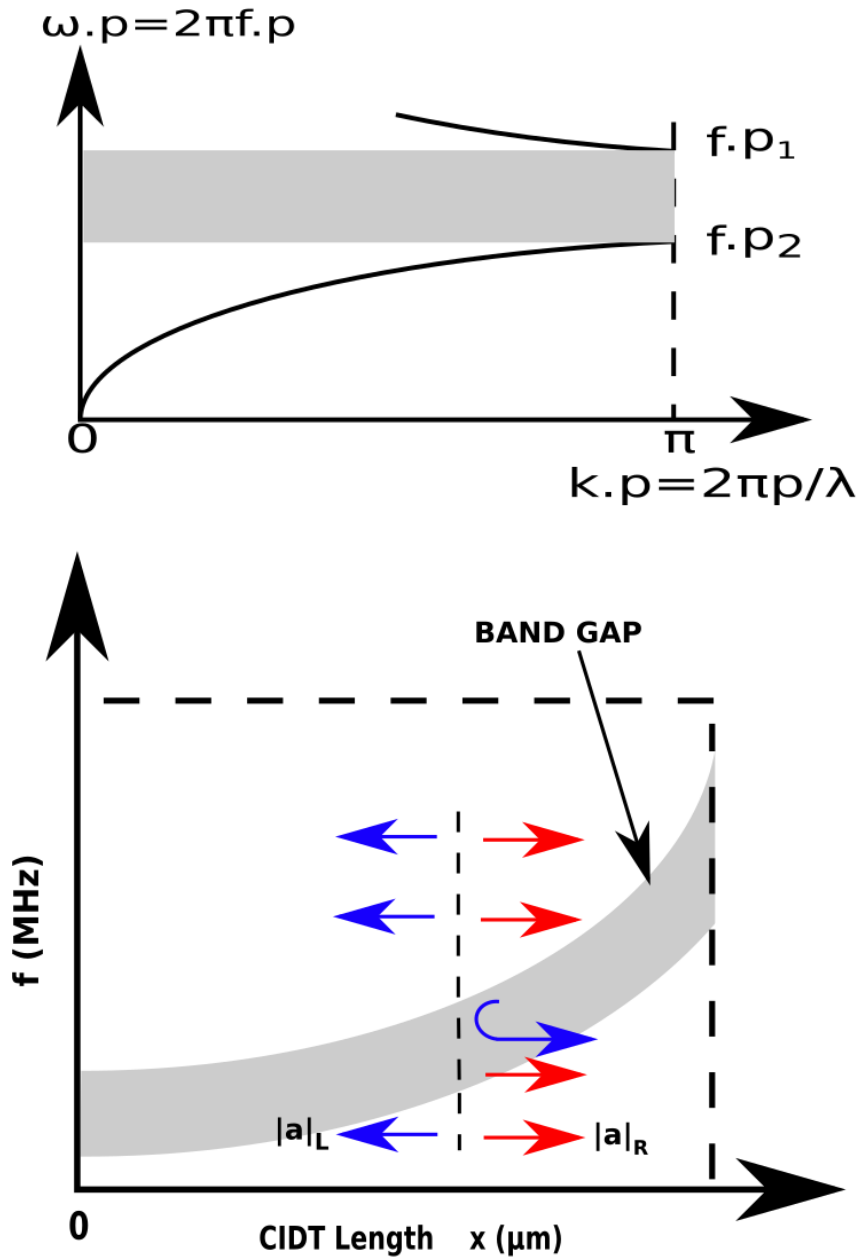


Figure 3.19: Appearance of band gaps for a (a) single period IDT and (b) chirped IDT. (a) shows the dispersion relation of the Rayleigh wave in the periodic grating with the wavenumber k . (b) shows the variation of the band gap frequency range with the position within the CIDT.

given by equation 3.16

$$\cos 2\pi\gamma = \frac{\cos \psi}{\cos \Delta} = \frac{\cos(2\pi f p s)}{\cos \Delta} \quad (3.16)$$

where Δ is the reflection coefficient per electrode, $f p$ is the frequency-period product, s is the slowness of the mode through one period, γ is the normalized wavenumber for the pole

associated to the short-circuited pseudo-mode in the wave number domain. Equation 3.16 is satisfied for an infinite number of electrode pairs. The analysis is restrained in the neighbourhood of the first stop-band and the phase variation of the pseudo-mode through one period is close to π . Figure 3.19(a) shows the dispersion curve and a band gap generated for a single period IDT with infinite number of electrodes. fp_1 and fp_2 are the frequency-period products that show the beginning and the end position of the band gap.

In case of a chirped IDT when an input chirp is sent through the IDT grating with a varying pitch, there is a superposition of forward and backward propagating SAWs. The final response at each position within the IDT is due to interference of these waves and multiple internal reflections, created by the neighboring electrodes. The larger the number of electrode pairs generating a frequency, the stronger the reflections. These reflections cause a large dip in the amplitude for a small range of frequencies within the desired bandwidth, representing the band gap. The band gap at different positions within the IDT acts as a mirror, causing reflections in one direction. The cumulative effect of this phenomena results in a difference in amplitude between the waves exiting on either sides. Depending on the design parameters, these band gaps have a strong influence on the directivity of the device. In this work, the occurrence of these band gaps is investigated in UWB SAW devices working within a frequency range of 200 MHz – 400 MHz. A p-matrix approach, described in section 2.2.3.4 [78], is used to model the response of the three different chirped IDTs described in section 3.1.2, with an array of N strips. The resistivity of the electrodes and the bus bars is ignored. Figure 3.19(b) shows the band gap generation for a chirped IDT.

3.5.1/ Band gaps within a single period IDT

Figures 3.20 to 3.24 show the power response in linear and log scale for the pitch $p = 6.4 \mu\text{m}$ with a resonance frequency of 301.7 MHz. When the resonator is fairly small with 500 electrodes as seen in Figure 3.20 only the resonance frequency is observed with a primary standing mode at 303 MHz which is better visible in the 3.20(b). On increasing the number of electrodes to 1000, an increase in amplitude of the resonance frequency is observed as seen in Figure 3.21. The number of standing modes appearing on both sides of the resonance frequency also increases with the increase in the number of electrodes of the IDT for a given frequency range and a channelled spectrum of standing modes is visible.

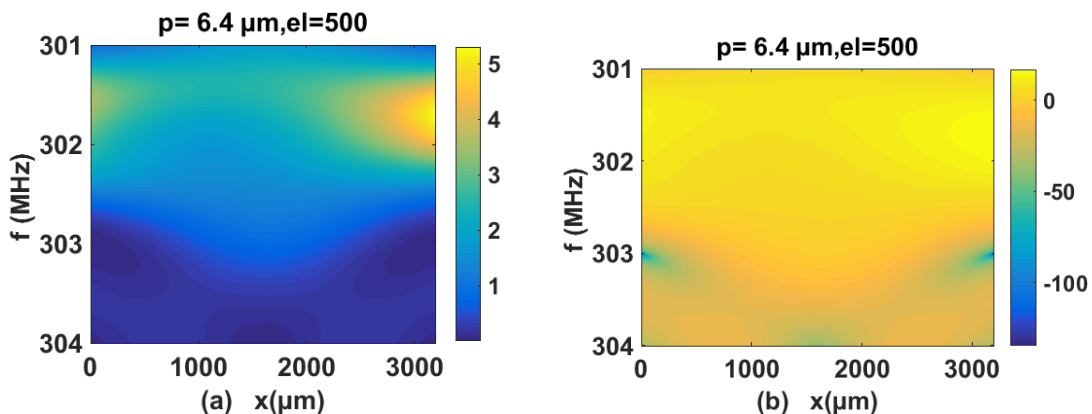


Figure 3.20: The power response at each electrode within the IDT with 500 electrodes (el) for a pitch $p = 6.4 \mu\text{m}$ in (a) linear scale (b) log scale.

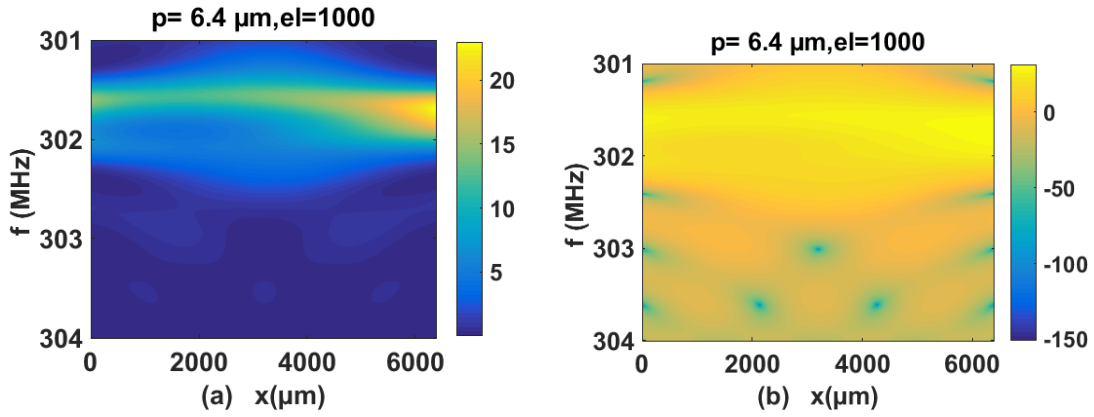


Figure 3.21: The power response at each electrode within the IDT with 1000 electrodes (el) for a pitch $p = 6.4 \mu\text{m}$ in (a) linear scale (b) log scale.

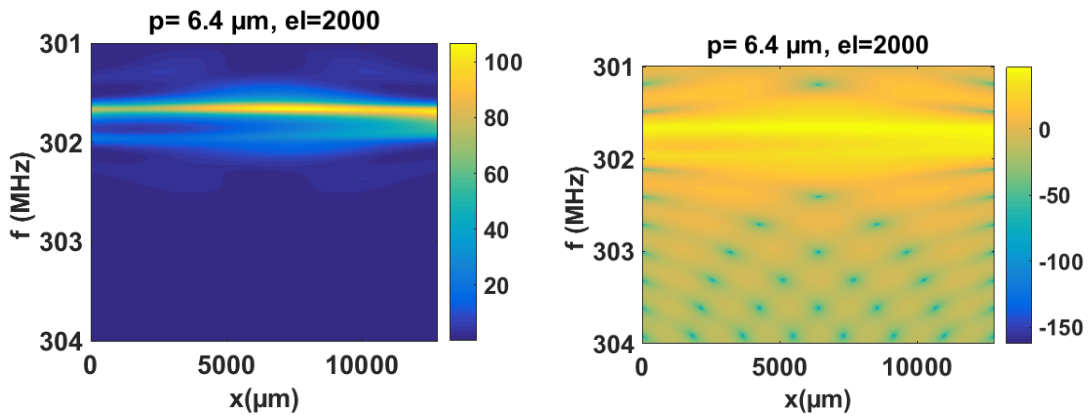


Figure 3.22: The power response at each electrode within the IDT with 2000 electrodes (el) for a pitch $p = 6.4 \mu\text{m}$ in (a) linear scale (b) log scale.

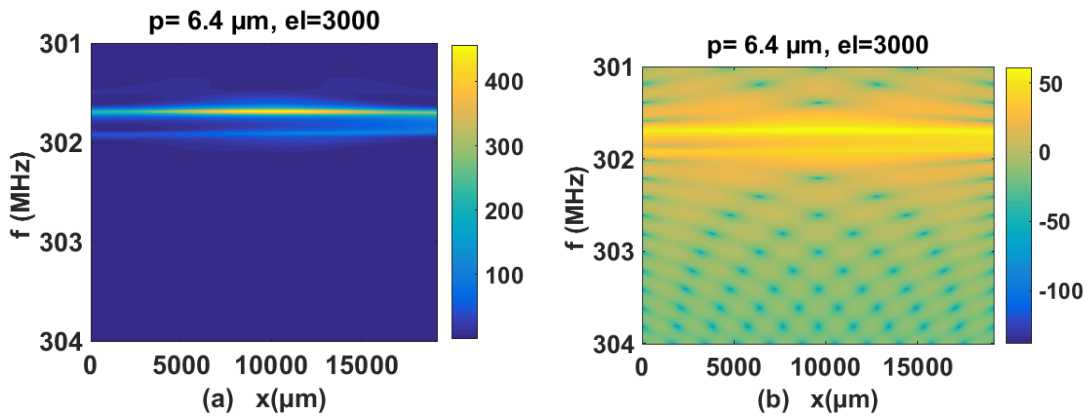


Figure 3.23: The power response at each electrode within the IDT with 3000 electrodes (el) for a pitch $p = 6.4 \mu\text{m}$ in (a) linear scale (b) log scale.

The position of the standing modes can be calculated by

$$f_{sm} \approx \frac{n\nu}{Np} = \frac{2nf_0}{N} \quad (3.17)$$

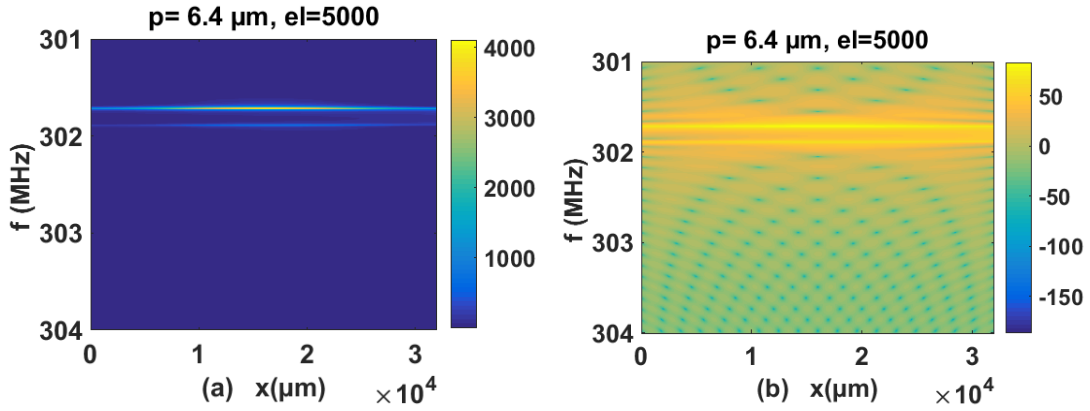


Figure 3.24: The power response at each electrode within the IDT with 5000 electrodes (el) for a pitch $p = 6.4 \mu\text{m}$ in (a) linear scale (b) log scale.

where f_{sm} is the standing mode frequency, n is the order of the standing mode, $v = \lambda \cdot f_0$ is the SAW velocity, f_0 is the resonance frequency, N is the total number of electrodes, $p = \frac{\lambda}{2}$. For $N = 500$ electrodes, a standing mode is visible at 303 MHz, for $N = 1000$ electrodes, three standing modes are visible at a distance of ≈ 0.6 MHz from each other, and for $N = 2000$ electrodes, standing modes with a spacing of ≈ 0.3 MHz from each other.

As the number of electrodes increase, two peaks are observed, one at the resonance frequency of 301.7 MHz and another one at 301.9 MHz. Both peaks mark the beginning and end position of the band gap corresponding to fp_1 and fp_2 in figure 3.19. The amplitude of both resonance peaks are observed to be higher at the center of the CIDT. For $N = 3000$ and $N = 5000$ electrodes, standing modes appear between fp_1 and fp_2 , with a spacing of ≈ 0.2 MHz and ≈ 0.1 MHz from each other for the respective cases.

3.5.2/ Band gaps within a Chirped IDT

The waves exiting on either side of the CIDT with 300 electrodes have similar chirp profiles with a slight difference in amplitudes as seen in figure 3.25. This is valid for all three chirp types. As seen in section 3.1.3, even though for the linear chirp the chirp profile is flat on top, the amplitude is much lower than that of a hyperbolic chirp. For the hyperbolic and mean chirps the slope of the chirp profile is not flat. The amplitude varies as a function of frequency. The amplitude for high frequencies is higher, like that of the hyperbolic chirp but the overall amplitude for the chirp is quite low compared to that of the hyperbolic chirp, like the linear case. The band gap profiles are also quite different for the 3 chirps.

The CIDT responses shown in figures 3.25 and 3.26 are for single period down-chirped IDTs with 300 electrodes and 3000 electrodes respectively. In the linear and mean chirped case shown in figures 3.25 and 3.26(a) and (c), the band gap varies as a parabolic curve along the length of the CIDT. However, for the hyperbolic chirp shown in figures 3.25(b) and 3.26(b), the band gap varies linearly.

The chirp profile for the linear case is no longer flat at the top as seen in figure 3.26(a) and resembles the chirp profiles of the other chirps. However, the amplitude of the waves exiting on the left of the IDT is much lower compared to the amplitude exiting on the right as expected. It is the same for all the three chirps but the difference in amplitude of the waves exiting in the two directions is the largest for the linear chirp. This shows that the band gaps created within

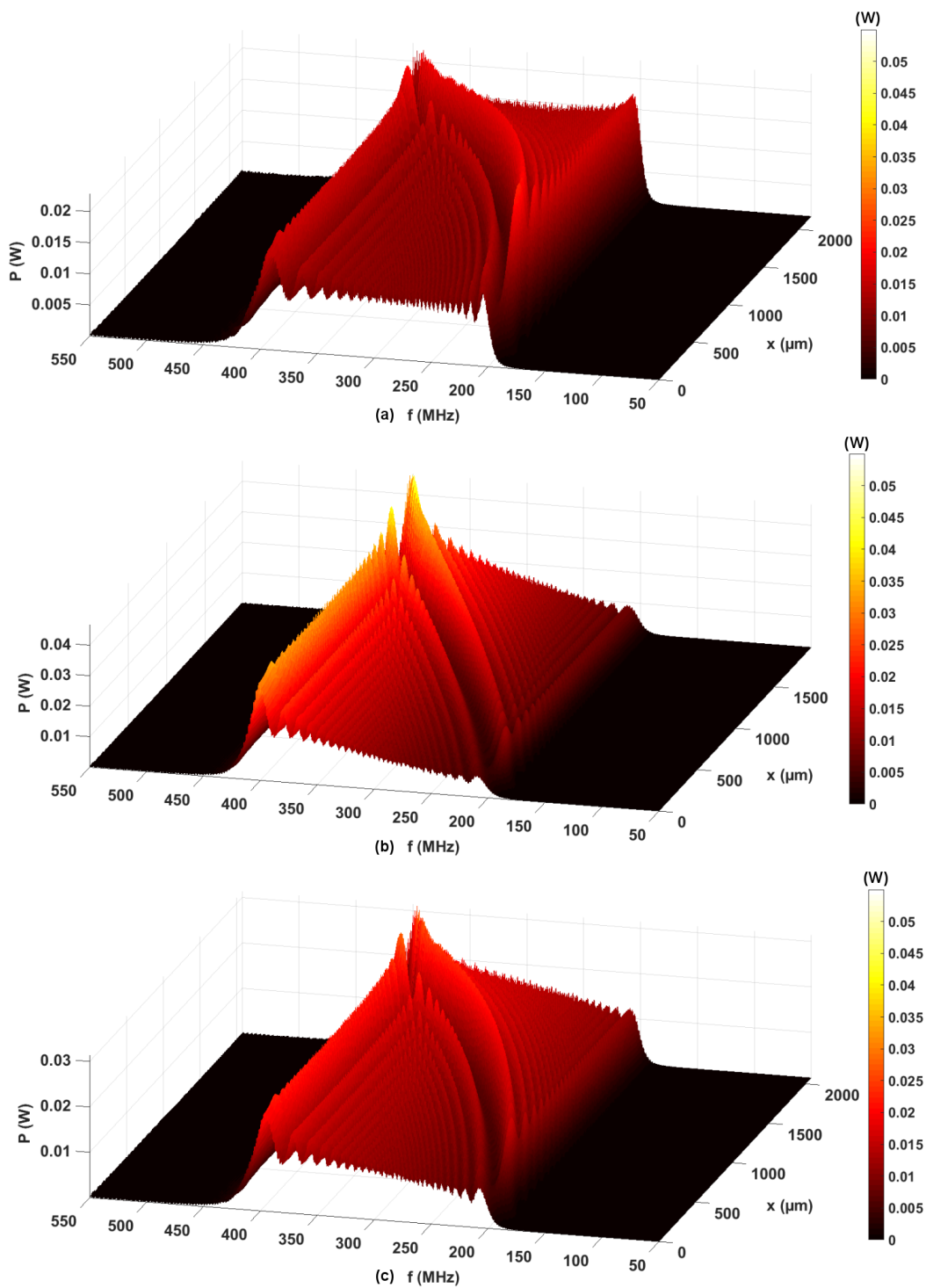


Figure 3.25: 3D plots of the power response at each electrode within the CIDTs with 300 electrodes generating (a) linear (b) hyperbolic and (c) mean chirps respectively.

the device impart a certain amount of directivity to the CIDT, i.e., the CIDTs work better in one direction compared to another. Figure 3.25 shows that for 300 electrodes, the CIDTs are already directional but with an increase in the number of electrodes as seen in figure 3.26, the internal reflections get stronger and the band gaps act as better mirrors thus increasing the

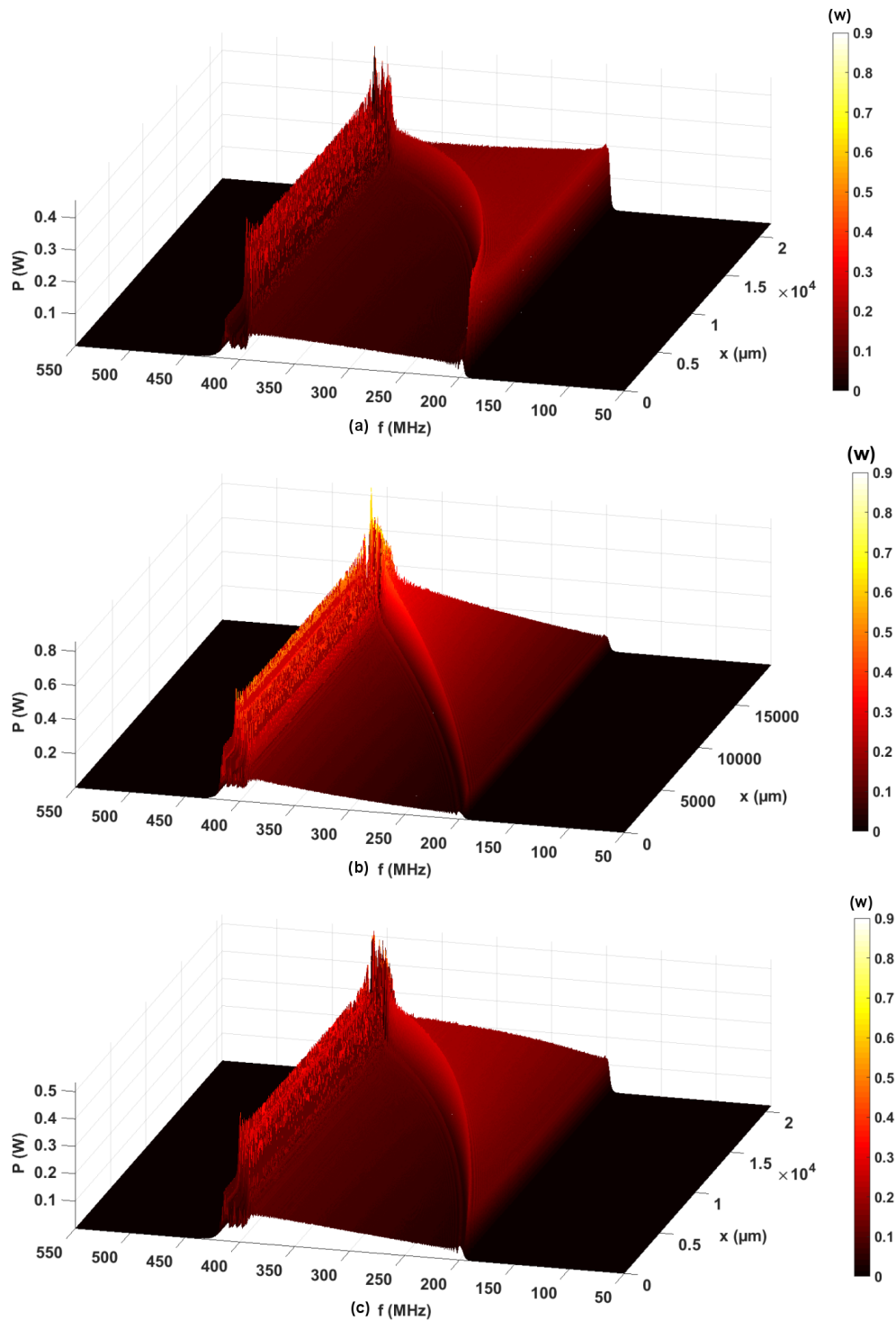


Figure 3.26: 3D plots of the power response at each electrode within the CIDTs with 3000 electrodes generating (a) linear (b) hyperbolic and (c) mean chirps respectively.

directivity of the CIDTs for all the three chirp types. Figures 3.27 and 3.28, show the power response of the waves exiting the CIDT towards the left and the right for a down chirped IDT, for the three types of chirps, for 300 and 3000 electrodes respectively.

In case of up-chirped CIDTs for the three cases, the power response of the chirp signal are

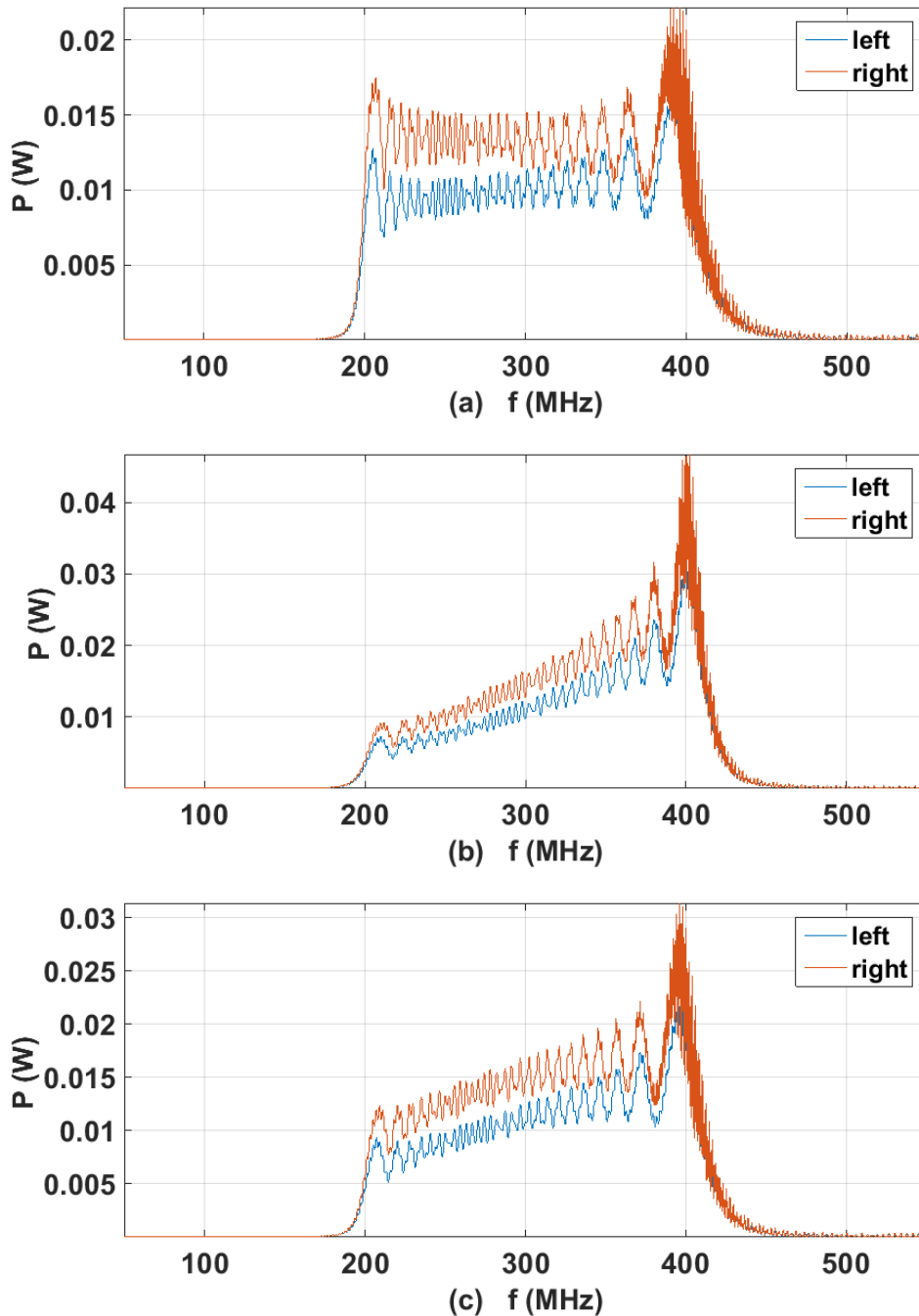


Figure 3.27: Plots of the power response of the waves exiting on the left and the right of the down chirped IDT with 300 electrodes generating (a) linear (b) hyperbolic and (c) mean chirps respectively.

shown in figures 3.29 and 3.30 for 300 and 3000 electrodes, respectively. In Figure 3.29, it is observed that the band gaps propagate within the desired bandwidth of 200 MHz - 400 MHz, linearly along the length of the respective CIDTs, appearing close to the higher frequencies at the beginning of the CIDTs and propagating towards the lower frequencies of the bandwidth along the length of the CIDTs.

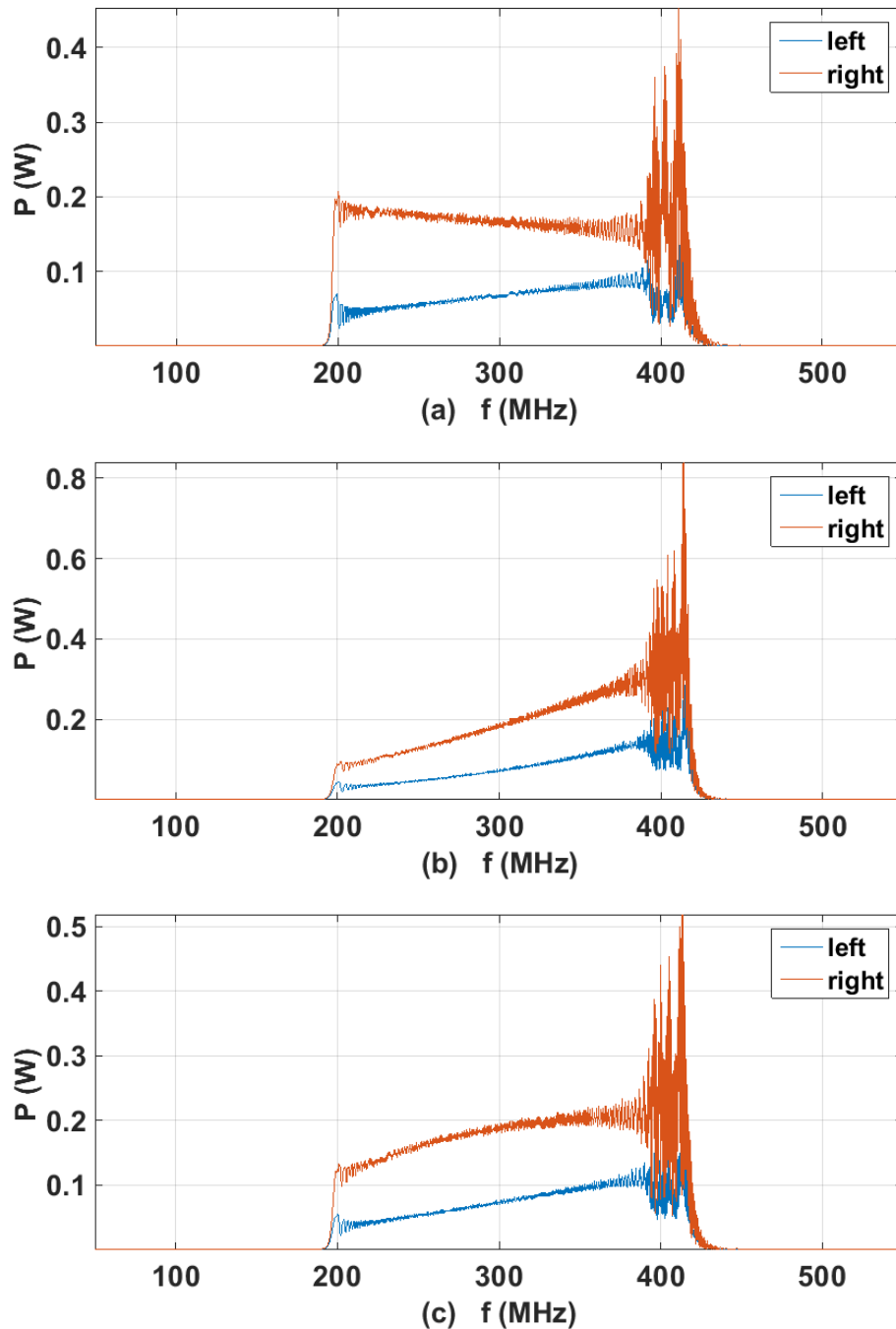


Figure 3.28: Plots of the power response of the waves exiting on the left and the right of the down chirped IDT with 3000 electrodes generating (a) linear (b) hyperbolic and (c) mean chirps respectively.

Figure 3.30 shows that when the number of electrodes is increased to $N=3000$, the wave exiting left has a higher amplitude compared to the wave exiting on the right of the CIDT. The internal reflections are stronger as expected, and the band gap is more efficient as a mirror compared to the case of $N=300$ electrodes as shown in figure 3.29. However, unlike for the case of down-chirp CIDTs, the band gap in this case reflects the energy in the opposite direction. Therefore the directivity of the device increases but towards the left. It is the same behavior

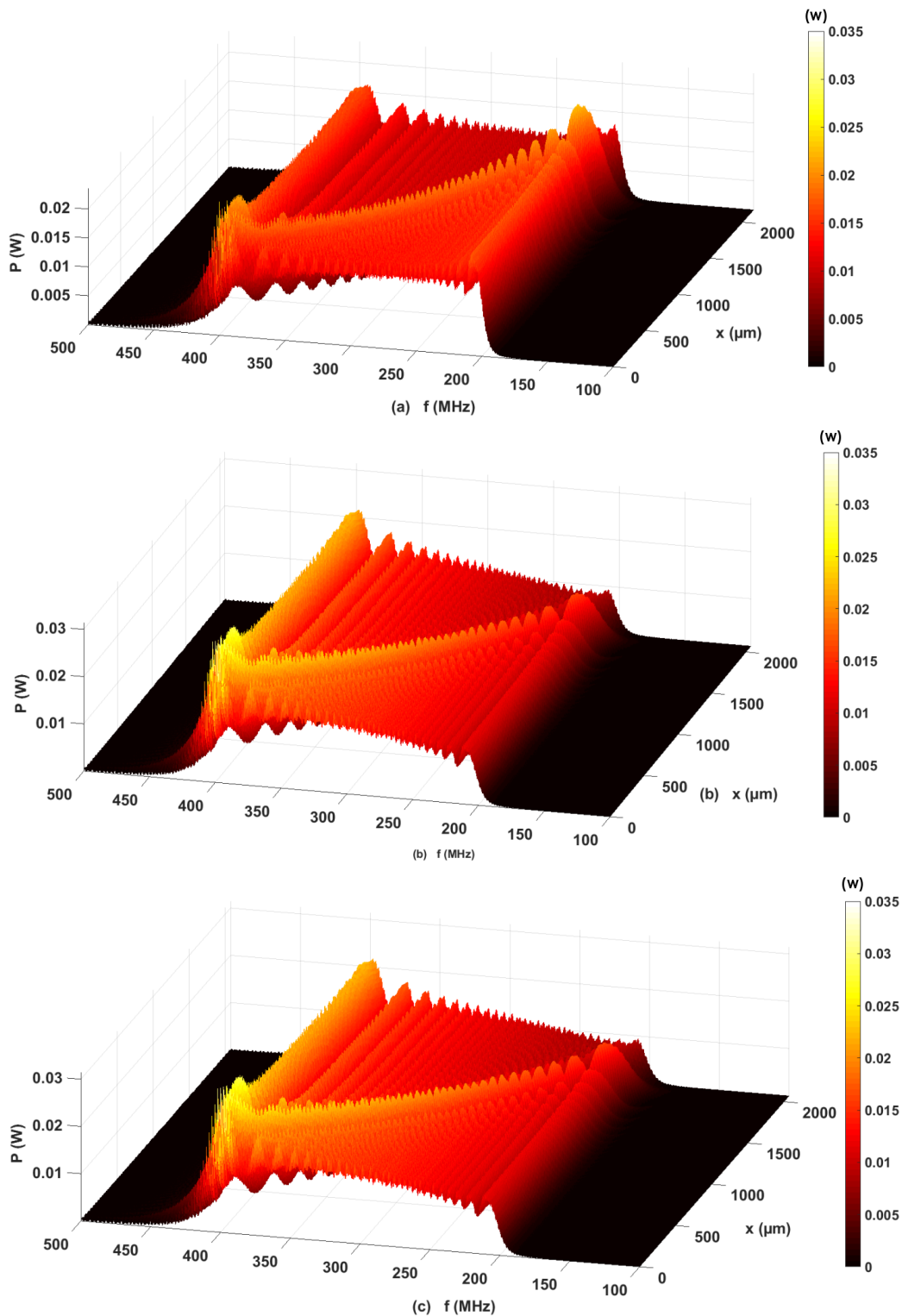


Figure 3.29: 3D plots of the power response at each electrode within the up-chirped CIDTs with 300 electrodes, designed using the p-matrix model, corresponding the fabricated devices, generating (a) linear (b) hyperbolic and (c) mean chirps respectively.

for all three types of CIDTs. This is clearly observed from figures 3.27, 3.28, 3.31 and 3.32.

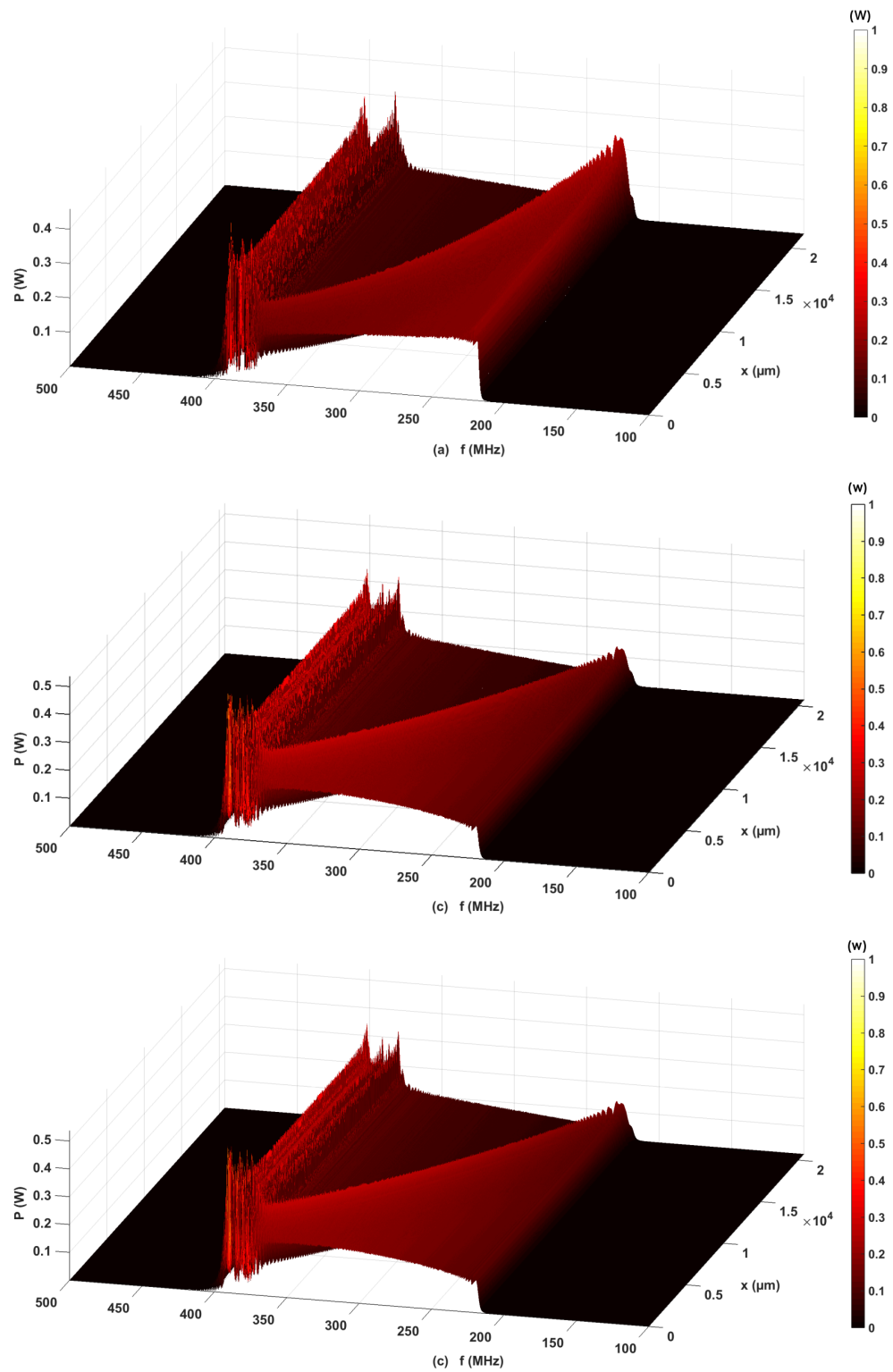


Figure 3.30: 3D plots of the power response at each electrode within the up-chirped CIDTs with 3000 electrodes, designed using the p-matrix model, corresponding the fabricated devices, generating (a) linear (b) hyperbolic and (c) mean chirps respectively.

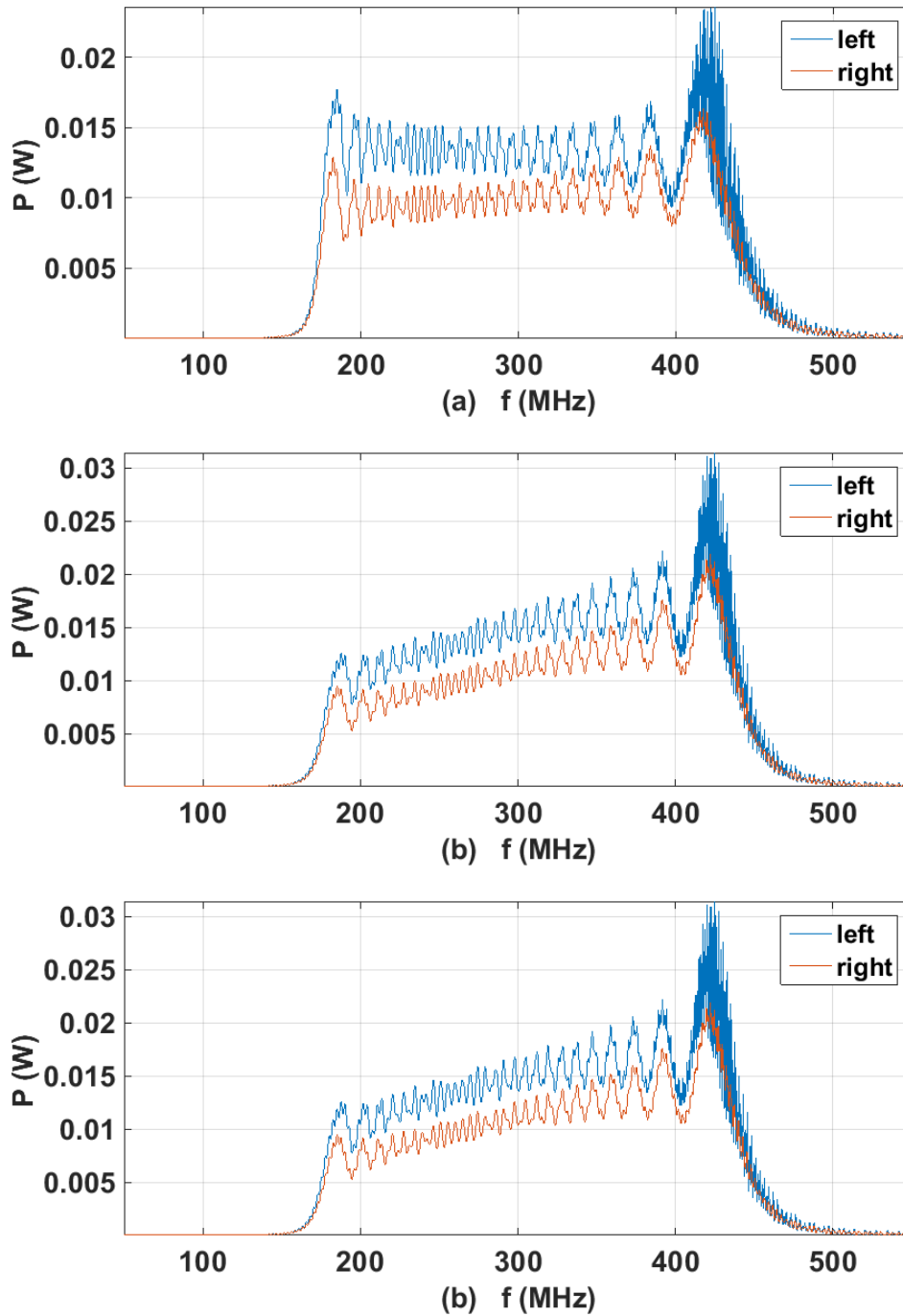


Figure 3.31: Plots of the power response of the waves exiting on the left and the right of the up chirped IDT with 300 electrodes generating (a) linear (b) hyperbolic and (c) mean chirps respectively.

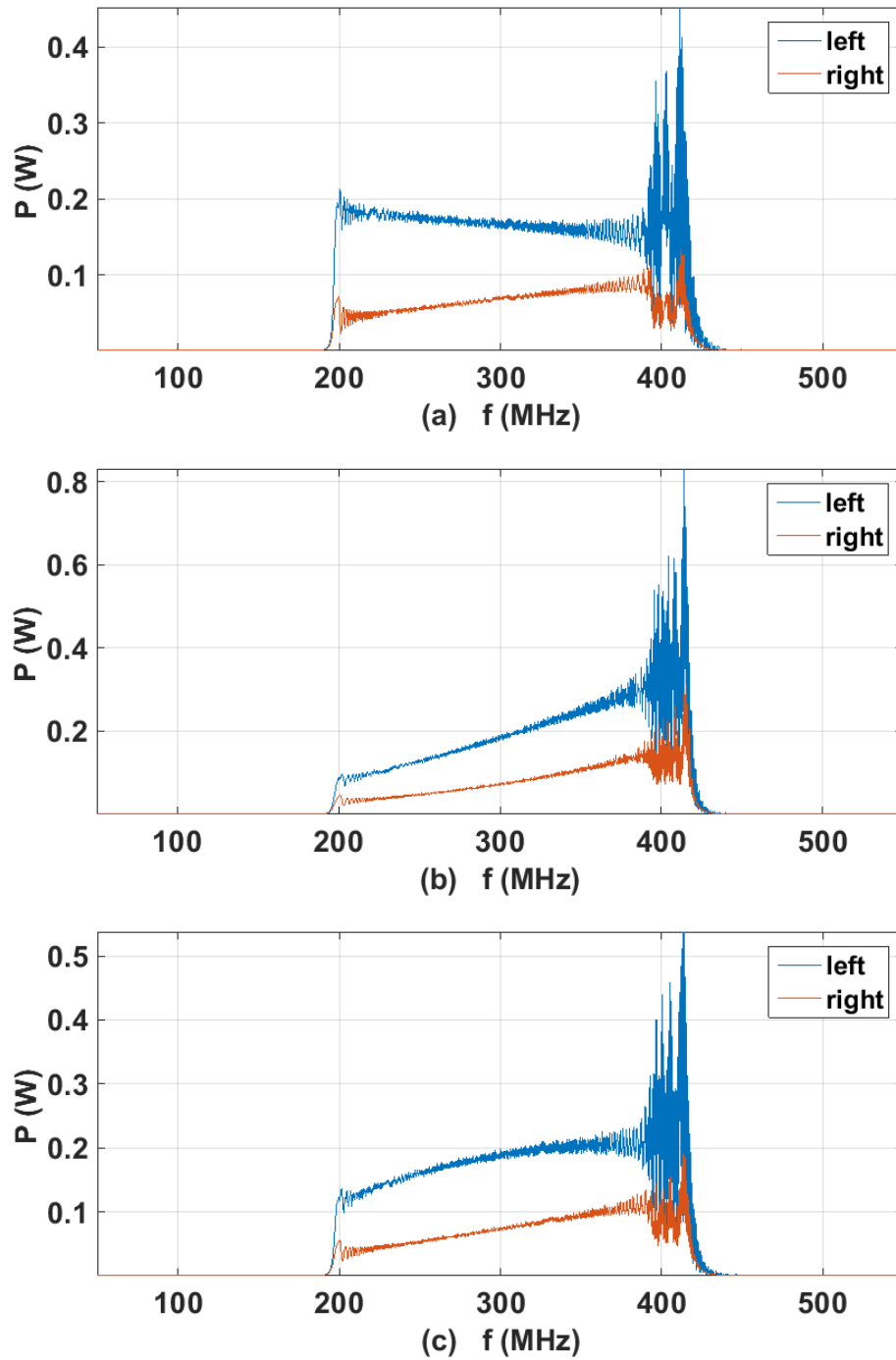


Figure 3.32: Plots of the power response of the waves exiting on the left and the right of the up chirped IDT with 3000 electrodes generating (a) linear (b) hyperbolic and (c) mean chirps respectively.

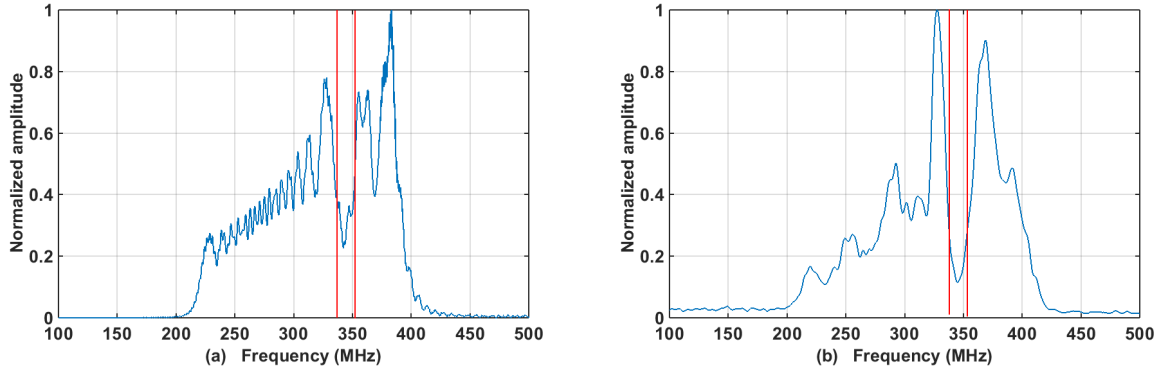


Figure 3.33: (a) Normalized signal response at the center of a down-chirped CIDT shown in figure 3.26 (a), simulated using the p-matrix model and (b) plot of the SAW device response measured using a differential interferometer [79], showing the existence of a band gap at around 350 MHz.

3.5.2.1/ Experimental results

A differential interferometer described in detail in Chapter 4, section 4.2, in an experimental setup described in section 4.5, is used to measure the short pulse generated using the CIDT of the reference sample described in section 3.2, at approximately the center of the CIDT. Figure 3.33 (b) shows a normalized signal response in the frequency domain, obtained by performing a Fourier transform on the measured pulse. This is compared to the normalized response of a linear chirped IDT obtained using the p-matrix model, at the center of the CIDT, as shown in figure 3.26 (a). Though the optical measurement is noisy, it is observed that the band gap exists around approximately 350 MHz for both cases.

3.5.3/ Variation in the height of the electrodes

In theory, the electrode films should be as thin as possible. Experimentally, however, it must be ensured that the electrical resistance of the IDT electrodes is not significant, as this can contribute to circuit-factor loading $C(f)$ and insertion loss. Typical aluminum film thicknesses used in IDT fabrication are in the range 50 nm -200 nm. The fractional velocity decrease $\frac{d\nu}{\nu}$ due to this mass loading in the metallized regions is given by equation 3.18 [54].

$$\frac{d\nu}{\nu} \approx \frac{2\pi Fh}{\lambda} + \frac{0.5K^2}{1 + 0.5K^2 + \frac{1}{\epsilon_r}} \quad (3.18)$$

for thin films with $h/\lambda < 0.01$, where h is the metal thickness, λ is SAW wavelength, ν is the unperturbed SAW velocity and F is a constant for the metal used, with values $F = 0.037$ for lithium niobate [80,81], and ϵ_r is the relative permittivity of the substrate.

In this section, the metal deposition thickness h is varied from 50 nm to 2 μm for a down-chirp CIDT and from 50 nm to 5 μm for an up-chirp CIDT, with a linearly varying pitch, to study its effects on the directivity of the SAW device. Figure 3.34 (a) and (c) show a very perturbed response of the waves exiting on the left and on the right of the CIDT for a metal thickness of 50 nm and 500 nm, respectively. The amplitude of both waves exiting the CIDT is approximately equal. The band gap propagation within the CIDT is fairly irregular. For a metal thickness of 200 nm, i.e., the value used for designing and fabrication of the SAW

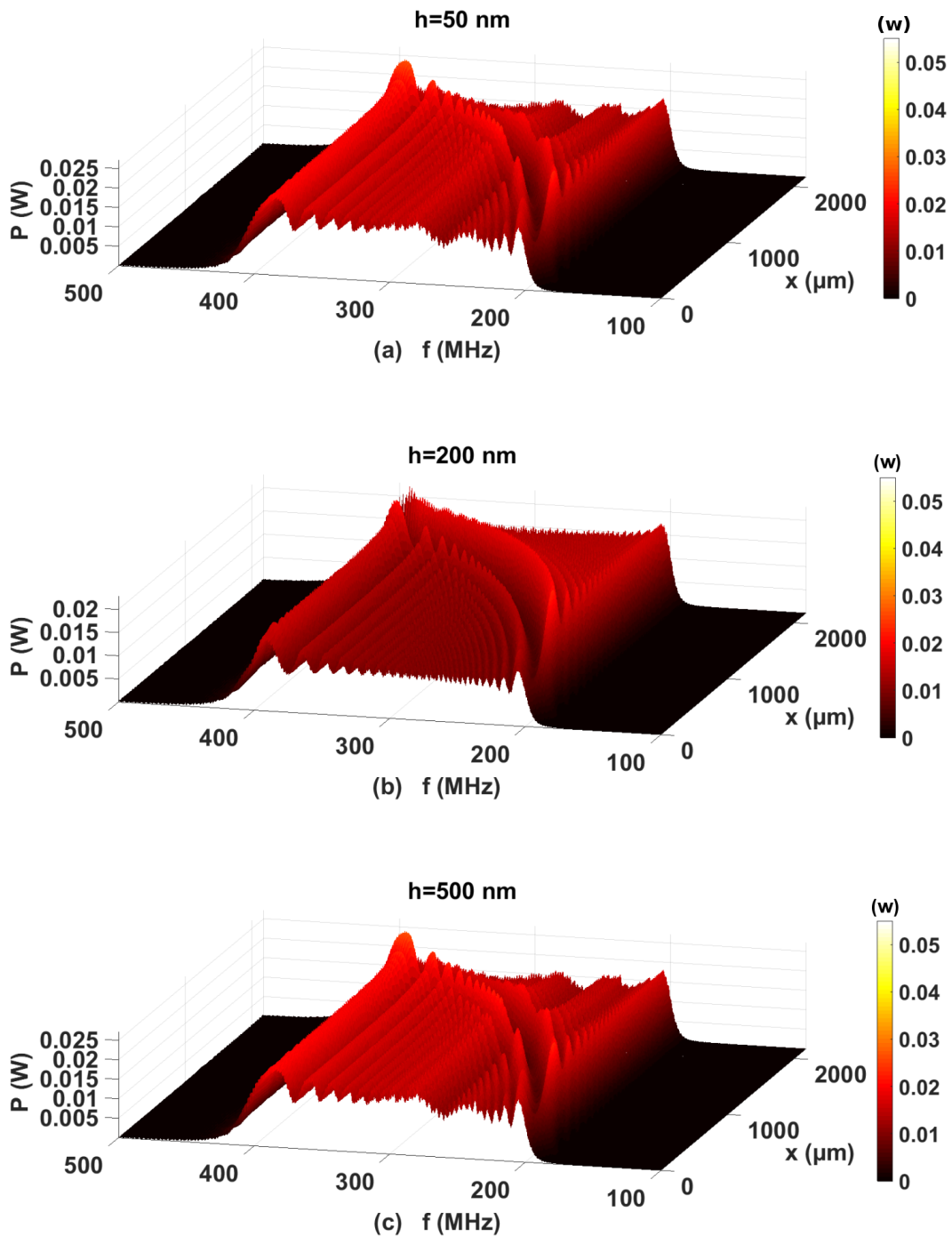


Figure 3.34: Plots of the power response of the waves exiting on both sides of the CIDTs with 300 electrodes generating a linear down-chirp for metallization height (a) $h=50$ nm (b) $h=200$ nm and (c) $h=500$ nm.

devices, discussed in section 3.1.1, as seen in figure 3.34 (b), the band gap propagates without any irregular perturbations and acts as a better mirror, compared to the previous case of $h=50$ nm, as a result, the wave propagating towards the right is larger in amplitude compared to the

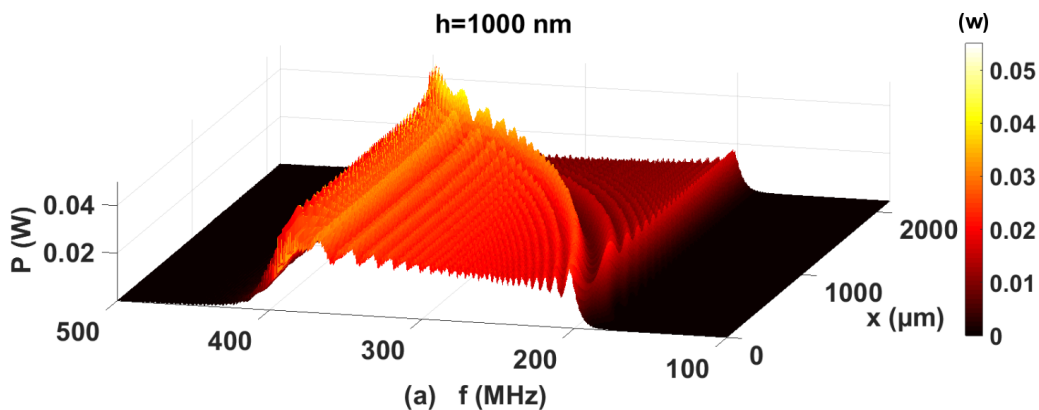


Figure 3.35: A 3D plot of the power response at each electrode within the CIDTs with 300 electrodes generating a linear down-chirp for metallization height $h = 1000$ nm.

wave exiting to the left.

When the thickness is increased beyond 500 nm, the directionality changes as seen in figure 3.35. SAW exiting the CIDT towards the left has a larger amplitude compared to that propagating to the right. The band gap becomes more efficient in the opposite direction. Thus, it is observed that by increasing the value of h , we can reverse the directivity of a linear down-chirp CIDT.

In case of a linear up-chirp CIDT, the variation of h has a different effect on the directionality of the device. In this case, the band gap progresses from high frequencies towards low frequencies within the bandwidth, in the opposite direction of that for a down-chirp CIDT. Figure 3.36 (a) and (c), show a very perturbed response of the waves exiting on the left and on the right of the CIDT as in the previous case of down-chirp CIDTs, for a metal thickness of 50 nm and 500 nm, respectively. The amplitude of both waves exiting the CIDT is approximately equal. The band gap propagation within the CIDT is fairly irregular. For a metal thickness of 200 nm, i.e., the value used for designing and fabrication of the SAW devices, discussed in section 3.1.1, as seen in figure 3.36 (b), the band gap propagates without any irregular perturbations and acts as a better mirror, compared to the previous case of $h = 50$ nm and $h = 500$ nm, as a result, the wave propagating towards right is larger in amplitude compared to the wave exiting to the left.

When the thickness is increased beyond 500 nm, the directionality changes as seen in figure 3.37. For $h = 1000$ nm, SAW exiting the CIDT towards the left has a larger amplitude compared to that propagating to the right. The band gap becomes more efficient in the opposite direction just as it is in case of an down-chirp CIDT.

Figure 3.38 shows the variation in the value of the reflection coefficient $|\Delta|$, and the directivity ($^\circ$) for a metallization ratio ($\frac{a}{p}$) of 0.5, for LiNbO₃ YX 128° rotated. The values of these plots are obtained from the grid described in section 2.2.4.2. As the $\frac{h}{\lambda}$ value varies, the value of $\cos \Delta$ increases, reaches a maximum for zero reflectivity, when $\frac{h}{\lambda} = 3$ (%) and changes sign when $\frac{h}{\lambda} = 6$ (%). This explains the change in directionality observed for both up-chirped and down-chirped IDTs when $h = 1000$ nm, as the $\frac{h}{\lambda}$ value for that is ≈ 7.8 (%) as shown in table 3.4. For this value of $\frac{h}{\lambda}$, the cosine of reflection coefficient is negative.

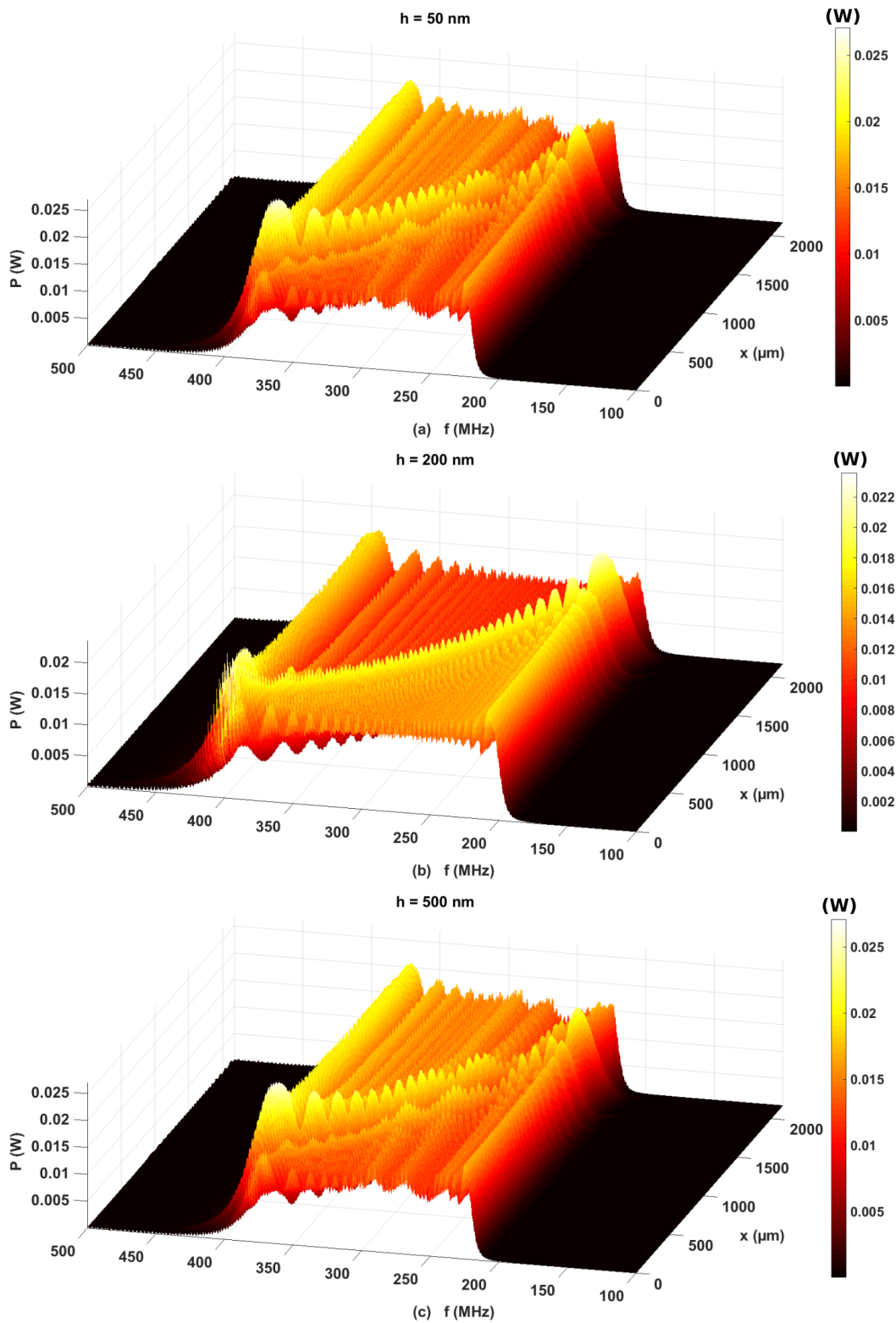


Figure 3.36: Plots of the power response of the waves exiting on both sides of the CIDTs with 300 electrodes generating a linear up-chirp for metallization height (a) $h = 50$ nm (b) $h = 200$ nm and (c) $h = 500$ nm.

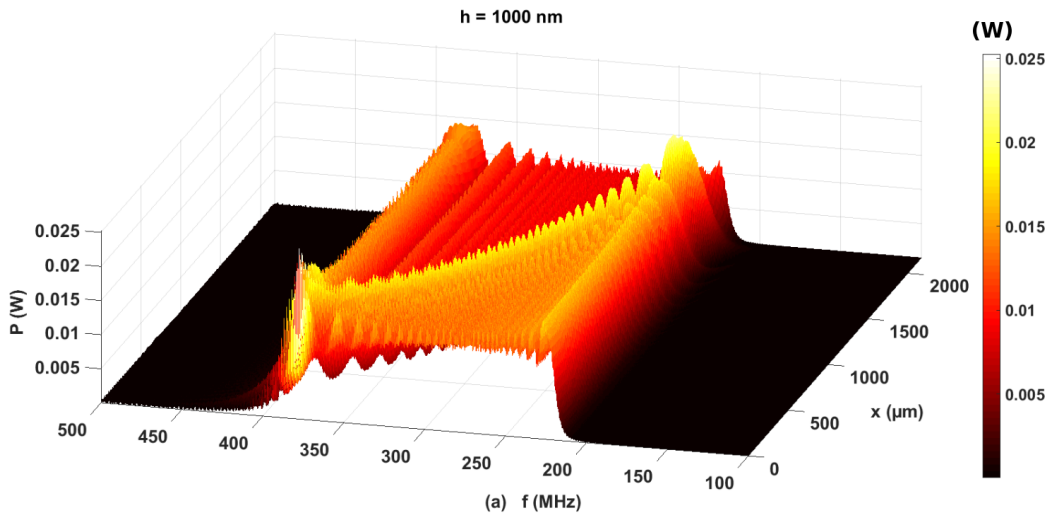


Figure 3.37: A 3D plot of the power response at each electrode within the CIDTs with 300 electrodes generating a linear up-chirp for metallization height $h = 1000$ nm.

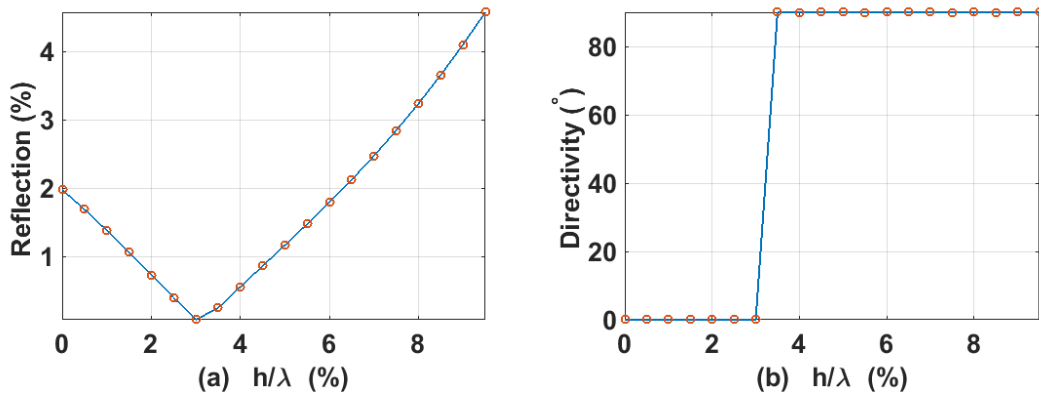


Figure 3.38: Plot showing a variation in (a) the reflection (%), i.e. $|\Delta|$, and (b) the directivity, as the $\frac{h}{\lambda}$ parameter changes. The metallization ratio used $\frac{a}{p} = 0.5$.

Table 3.4: The $\frac{h}{\lambda}$ values for different heights (h) used to study the variation in the directivity of the CIDTs

h (μm)	0.050	0.200	0.500	1.000	2.000
$\frac{h}{\lambda}$ (%)	0.39	1.5601	3.9002	7.8003	15.6

3.6/ Conclusion

In summary, using a p-matrix model SAW devices with three different chirped input IDTs and an UWB output IDT are designed and fabricated. The SAW device with the hyperbolic chirp is found to have the best response in terms of power of the transmitted signal. The variation of the pitch for the three cases show a distinct modulation in the amplitude with respect to frequency, in the reflection measurements.

In section 3.5.2, appearance of band gaps within the CIDTs has been studied and their effect on the directivity due to the variation in the CIDT design parameters have been demonstrated. It is observed that when the number of electrodes is varied, not only does the amplitude of the signals exiting the CIDTs in both directions increase but the band gap are more efficient in reflecting the energy in one direction, making a bidirectional transducer unidirectional to a certain extent. For a given value of the electrode thickness h , the reflection coefficient changes sign. This causes the band gap to reflect the energy in the opposite direction resulting in a directionality flip for the CIDTs.

A differential optical interferometer for measuring short pulses of surface acoustic waves

Optical interferometry is a well-known technique for studying wave propagation and is often preferred over other methods for its high precision in studying wave profiles, amplitude and phase variations, standing wave patterns, or group delays [8]. Various interferometers have been developed and employed to study the ultrasonic motion of SAW. In this chapter, the next step of this work, i.e., the development of a differential interferometer is described and the measurement of the displacements caused by the propagation of a short pulse of surface acoustic waves on the piezoelectric substrate of the SAW device, described in chapter 3, section 3.2, using the differential interferometer, is investigated.

4.1/ Interferometers for short pulse measurements

Both the Michelson interferometer depicted in Figure 4.1(a) and the Sagnac interferometer depicted in Fig. 4.1(b) rely on the principle of interference between divided wavefronts as described in chapter 2. In both case, the SAW device or substrate supporting SAW propagation is placed within the interferometer. The Michelson interferometer compares an optical wavefront reflected on the vibrating specimen with a reference wavefront. It allows one for high resolution measurements but is extremely sensitive to fluctuations in path difference, causing a slow drift of the response over time. Various active stabilization methods [16, 82, 83] and heterodyne techniques [84–88] have been proposed to overcome this problem. In contrast, the Sagnac interferometer compares two time-delayed wavefronts that have traveled the same path of micro-optical elements, but in opposite directions as explained in chapter 2, section 2.1.4. It is naturally immune to slow fluctuations in the lengths of the arms of the interferometer. It has been used for the selective detection of time-harmonic SAW propagation [27], but also for the detection of laser-generated ultrasonic short pulses [89, 90]. One practical difficulty, however, is to manage the beam size difference that appears between the two different paths, as a result of focusing on the sample within the Sagnac loop [90].

The Sagnac interferometer belongs to the more general class of differential interferometers, whereby a wavefront is compared with its replica shifted either in space or time. As discussed by Monchalín [8], various differential interferometric techniques have been proposed to detect and measure surface vibrations. For example, Turner and Claus used lateral-shearing interferometry to measure the amplitude and direction of propagation of ultrasonic surface waves [12]. Such

measurements are suited for time-harmonic waves.

In this chapter, we propose a time-delay differential interferometer in which the sample sup-

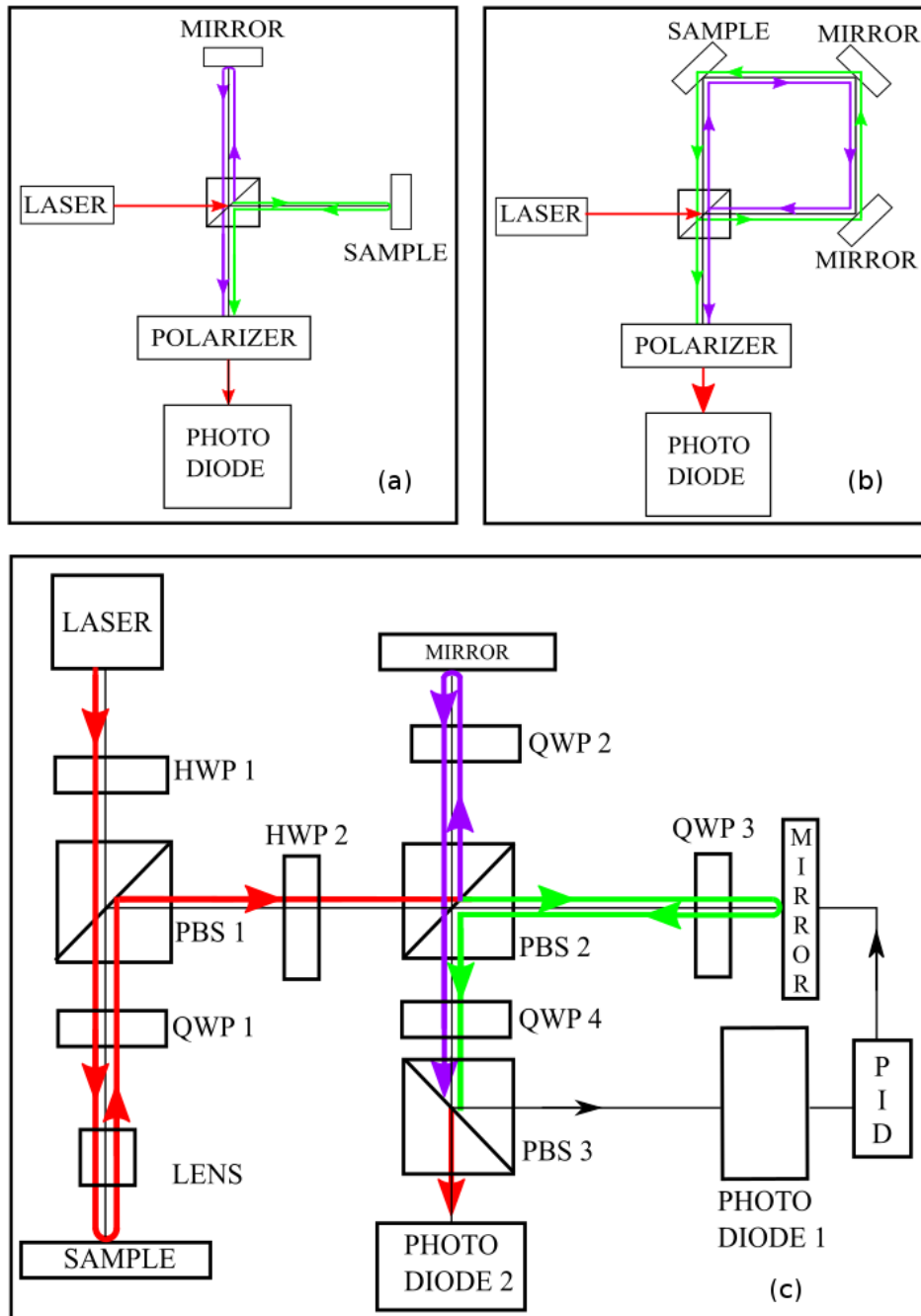


Figure 4.1: Schematic representation of three optical interferometers for the measurement of surface acoustic wave short pulses. (a) Michelson interferometer with the vibrating sample inside one arm of the interferometer. (b) Sagnac interferometer with the vibrating sample inside the loop. (c) Time-shearing, or time-delay, differential interferometer with the vibrating sample before the interferometer [79]. PBS: polarizing beam splitter, HWP: half wave plate, QWP: quarter wave plate, PID: proportional – integral – derivative controller.

porting SAW propagation is placed before and outside the interferometer. As a result, it allows stable maneuvering of the sample, reducing irregular overlap between the incident and reflected beams that might cause a loss in amplitude and then measurement inaccuracies. However, unlike the Sagnac interferometer, it is not immune to slow fluctuations in the differential path length and it has to be stabilized using a proportional–integral–derivative (PID) controller. Using this setup, we investigate the measurement of short SAW pulses, with smallest durations of about 10 ns, generated by a chirped wideband interdigital transducer.

4.2/ Working principle of the differential interferometer

The differential interferometer is depicted in Figure 4.1(c). The interferometer setup [91] is an extended version of a homodyne Michelson interferometer implementing time-shearing. A single-mode narrow-linewidth diode laser (New Focus, model Velocity 6305) with a wavelength of 651 nm and a nominal power of 10 mW is used as a highly coherent light source. The coherence length of the laser exceeds several hundred meters and was not a limitation in our experiments. A half-wave plate (HWP1) is placed before a polarizing beam splitter (PBS1) to adjust the input polarization. The beam is first transmitted to the sample, reflects on it, and enters the interferometric part of the setup after reflection inside PBS1. A quarter-wave plate (QWP1) provides the required polarization rotations. Four mirrors and a reflected light objective (Olympus, ultra long working distance model MSPlan 100 \times) are used to provide an extended path to the laser beam such that the SAW device can be placed horizontal to the optical table and the incident beam is normal to the SAW device. The spot size on the sample surface is smaller than 2 μm . This value must remain significantly smaller than the SAW wavelength in order to resolve pulse propagation. Note that after double pass through the objective the ellipticity of the laser beam is mostly corrected and the beam size inside the interferometer is about 1 mm as shown in Figure 4.2. HWP2 and PBS2 split the laser beam into two beams of equal intensity and orthogonal polarization in the interferometer.

At the exit of the interferometer, the two orthogonally polarized beams are recombined with a quarter-wave plate (QWP4) and a polarizing beam splitter (PBS3) to provide two outputs. The

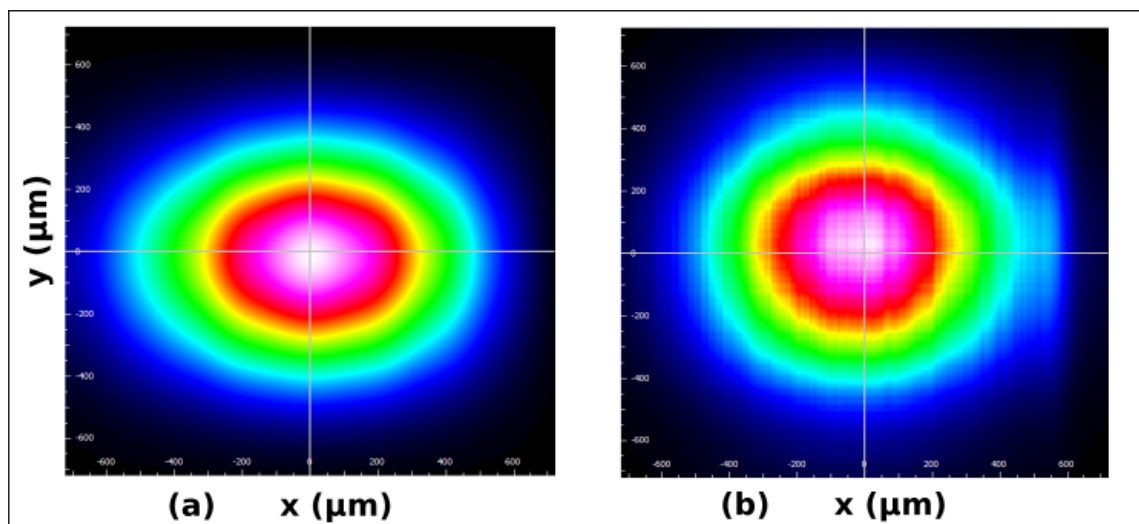


Figure 4.2: (a) The beam profile of the elliptical beam at the exit of the laser. (b) The circular beam profile at the exit of the differential interferometer setup.

interference signal detected by photodiode 1 (Electro-Optics Technology, Silicon pin detector ET-2020) is used to actively stabilize the path length difference to a single quadrature point using a proportional–integral–derivative (PID) controller for the position of one of the mirrors. The position of the mirror is controlled by a piezoelectric actuator (Thorlabs, model KC1-PZ/M, $\pm 4 \mu\text{m}$ linear travel range) receiving the correction signal. Since the SAW signal varies on a time-scale that is much shorter than the PID response time, it remains decoupled from the correction signal. The interference signal detected by photodiode 2 (Thorlabs model DET10A/M, 1 ns rise time) provides the SAW measurement.

The output intensity on photodiode 2 after recombining the wavefronts exiting the two arms of the interferometer is

$$I(t) = I_1 + I_2 + 2m \sqrt{I_1 I_2} \cos(\phi_2(t) - \phi_1(t)) \quad (4.1)$$

with I_i and ϕ_i the intensity and phase in arm i . The visibility m , a number between 0 and 1, is introduced to account for possible reduction of the interference intensity because of loss of either spatial or temporal coherence. The interferometer is operated so that $I_1 \approx I_2$ to maximize interference visibility. The phase variation in either arm can be decomposed as

$$\phi_i(t) = \Phi_i + \frac{4\pi}{\lambda} u(x, t - L_i/c) + \psi_i(t) \quad (4.2)$$

with Φ_i a static configuration phase, independent of time, the vibration-induced deterministic phase $\frac{4\pi}{\lambda} u(x, t - L_i/c)$ where $u(x, t)$ is the displacement at position x that is to be measured, and $\psi_i(t)$ a random phase including all fluctuations. L_i is the optical path length of arm i , so L_i/c measures the wavefront delay, with c the speed of light. In order to provide maximum sensitivity, the stabilized interferometer is operated so that $\Phi_2 - \Phi_1 = \pi/2 \text{ modulo } \pi$. Writing $\Delta u(x, t) = u(x, t - L_2/c) - u(x, t - L_1/c)$ and $\Delta\psi(t) = \psi_2(t) - \psi_1(t)$, we have

$$I(t) = I_1 + I_2 + 2m \sqrt{I_1 I_2} \sin\left(\frac{4\pi}{\lambda} \Delta u(x, t) + \Delta\psi(t)\right). \quad (4.3)$$

The response of the interferometer is thus nonlinear with the out-of-plane displacements $\Delta u(x, t)$. However, assuming that the displacements are small compared to the optical wavelength and that the phase fluctuations are much less than 2π , we have approximately

$$I(t) \approx I_1 + I_2 + 2m \sqrt{I_1 I_2} \left(\frac{4\pi}{\lambda} \Delta u(x, t) + \Delta\psi(t)\right) \quad (4.4)$$

and the intensity changes linearly with respect to the differential displacement. The measurement depends on the path length difference $L_2 - L_1$. Indeed, we can define a delay time $\Delta t = (L_2 - L_1)/c$. If Δt is small compared to temporal variations of the displacement, then

$$\Delta u(x, t) \approx \Delta t \frac{\partial u}{\partial t}(x, t - T) \quad (4.5)$$

with $T = (L_2 + L_1)/2c$, and the interferometer essentially provides a measurement of the temporal derivative of the displacement. If in contrast Δt is large compared to the temporal duration of the pulse, then the same pulse will be observed twice in sequence but with a reversed sign.

The choice of the path length difference in the interferometer depends on the characteristics of the pulses to be measured. In the following section, we will present measurements for pulses with a duration $\Delta\tau$ of about 10 ns, a carrier frequency f_0 of 300 MHz, and a total bandwidth Δf of 200 MHz. First, in order for the interferometer to operate in the proportional regime, we

should impose $\Delta t > \Delta\tau$, which would require $L_2 - L_1 > c\Delta\tau \approx 3$ m. In practice, this value is too large and the proportional regime would be viable only for SAW pulses typically shorter than 1 ns. Second, equations (4.4-4.5) suggest that in the differential regime the value of Δt can be optimized. Indeed, Eq. (4.5) indicates that the measured intensity first increases linearly with Δt ; however this increase must be limited since the range of validity of this equation is limited by the condition that Δt is small compared to temporal variations of the pulse. For a time-harmonic signal at frequency f_0 , it is easily found from Eq. (4.4) that the optimal path length difference is given by $\Delta t = (2f_0)^{-1}$, leading to $c\Delta t \approx 0.5$ m for $f_0 = 300$ MHz. For this setting, if $u(x, t) = u_0 \sin(2\pi f_0 t)$, then $\Delta u(x, t) = 2u_0 \sin(2\pi f_0(t - T))$. For wide bandwidth signals, it should be expected that the optimal value of Δt will be slightly modified but that the order of magnitude will remain the same. This effect is discussed experimentally in the following section.

4.3/ Pulse compression experiment

The operation of the time-delay interferometer is evaluated using the short-pulse experiment depicted in Fig. 4.3. The SAW device used for this work comprise two ultra-wide bandwidth transducers. The substrate used is lithium niobate, Y+128°-rotated cut, X propagation, and

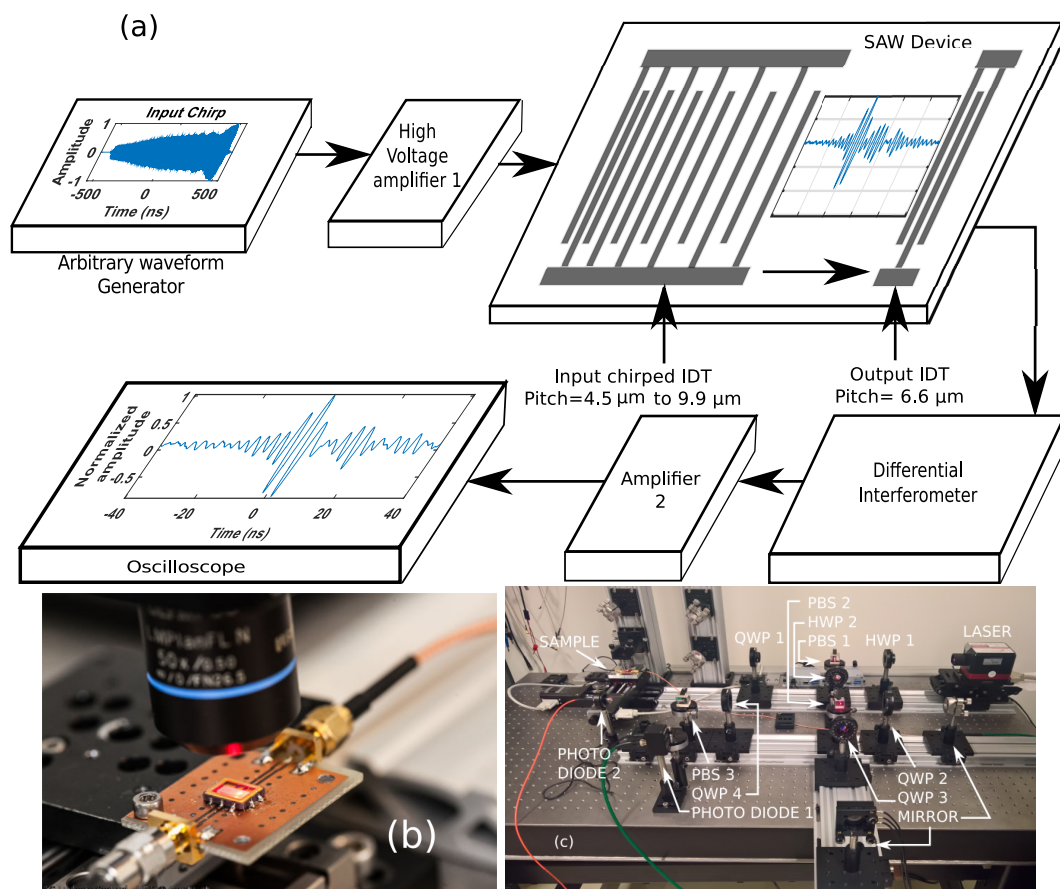


Figure 4.3: (a) Schematic of the short-pulse surface acoustic wave experiment. IDT: inter-digital transducer. (b) Close view at the sample mounting. (c) Photograph of the differential interferometer setup with elements indicated following the schematic in Figure 4.1(c), [79].

the metal used for the electrodes is aluminum.

The input IDT is linearly chirped with a frequency range between 200 MHz and 400 MHz, and comprise 150 pairs of electrodes and a constant acoustic aperture of $800\ \mu\text{m}$. The acoustic aperture value is larger than 20 times the longest SAW wavelength ($\approx 40\ \mu\text{m}$) and is chosen so as to reduce diffraction spreading of the SAW beam as it travels between IDTs. The distance between the input and the output IDT is $2066\ \mu\text{m}$. The output IDT is composed of only 3 electrodes and its central frequency is 300 MHz. The number of electrodes for a periodic IDT is limited by the relative bandwidth of the signal to be measured. Indeed, for a bandwidth $\Delta f = 200\ \text{MHz}$ and a central frequency $f_0 = 300\ \text{MHz}$, the maximum number of electrode pairs N_p is calculated using [55]

$$N_p \approx \frac{f_0}{\Delta f} = \frac{300}{200} = 1.5 \quad (4.6)$$

With this choice, we ensure that the output IDT does not alter significantly the spectral contents of the SAW pulse and that detection is spatially localized.

An arbitrary waveform generator (AWG; Tektronix, model AWG7122B) is used to send an input chirped signal to the input IDT, through a RF high voltage amplifier (Mini-Circuits, model AN-60-008) with a voltage amplification of 40 dBm. The input chirped signal has a dispersion inverse of that of the chirped IDT, as obtained using a network analyzer. Fig. 4.4(a) shows the spectrum of this chirped signal. As a result of dispersion compensation, a short SAW pulse is expected to be produced on the right side of the IDT and to subsequently propagate almost unaltered on the substrate surface. On the left side of the IDT, conversely, the SAW pulse is expected to be extended in time by twice the dispersion introduced by the IDT.

The SAW pulse is detected either using the output IDT or using the time-delay interferometer, with the laser beam focused at an arbitrary point on the surface. The interferometer output is amplified using an RF amplifier (Mini-Circuits, model ZFL-1000+) with a 17 dB gain. Both the electrical and interferometer outputs are measured using an oscilloscope with a 2 GHz bandwidth, 40 GSa/s sample rate and waveform averaging value of 1024 (Agilent, model Infiniium DSO80204B).

The shortest pulse that could be observable with this system is easily obtained from the signal generated by the AWG. Indeed, for a given spectrum the shortest pulse is obtained for a constant spectral phase, i.e. in the absence of dispersion. Taking the inverse Fourier transform of the spectrum in Fig. 4.4(a), the 10-ns pulse shown in Fig. 4.4(b) is obtained. This theoretical pulse is used as a reference for experimental measurements.

The output IDT provides a differential electrical measurement of the strain field accompanying the propagation of the surface acoustic wave. More precisely, it converts the electrical charges appearing at the metal/piezoelectric interfaces into a time-dependent voltage. The strain can be assumed to be proportional to the out-of-plane displacement $u(x, t)$. As the pitch – the distance separating adjacent electrode centers – is equal to half the acoustic wavelength at a frequency of 300 MHz and since the electrodes are alternated, the voltage that is measured can be approximated as

$$V(t) = Z_0 e_{\text{eff}} \frac{\partial u(x_0, t)}{\partial t} \quad (4.7)$$

with Z_0 the IDT impedance, e_{eff} an effective piezoelectric coefficient expressed in C/m, and x_0 the central position of the output IDT. From equations (4.4-4.7), it is apparent that the electrical and the optical measurements should be proportional in case the delay Δt is small.

The amplified electrical and interferometer measurements at the output electrodes are compared in Figure 4.5. The amplification used to obtain both measurements are different and hence both responses are normalized independently. For both measurements, the overall shape of the waveform is conserved and is in good agreement with the theoretical pulse shown in Fig. 4.4(b). However, it is observed that the main pulse is followed by consecutive ripples with diminishing amplitude.

4.4/ Measurement characteristics

The distance between the two IDTs is $2066 \mu\text{m}$ which gives a delay of 550 ns on LiNbO_3 YX cut 128 degrees rotated, with a SAW velocity of 3979 m/s . It can be observed from Fig. 4.5, that every ripple occurs with an interval of 16 ns , which is much less compared to the delay due to the distance between the IDTs. Hence it is safe to say that the ripples are not a consequence of multiple transit. The response of the SAW device was measured using a network analyzer and is presented in Fig. 4.6(a). It can be observed that the frequency bandwidth of interest ($200 \text{ MHz} - 400 \text{ MHz}$) has a uniform flat top and does not show strong modulation. On comparison with the electrical and interferometric measurements shown in Fig. 4.6(b), the number of significant dips are found to be consistent with the number of reflections (repetitions of the pulse). Hence, reflections within the chirped IDT itself can be ruled out. We attribute that to electronic reflections resulting from impedance mismatch between the sample and the

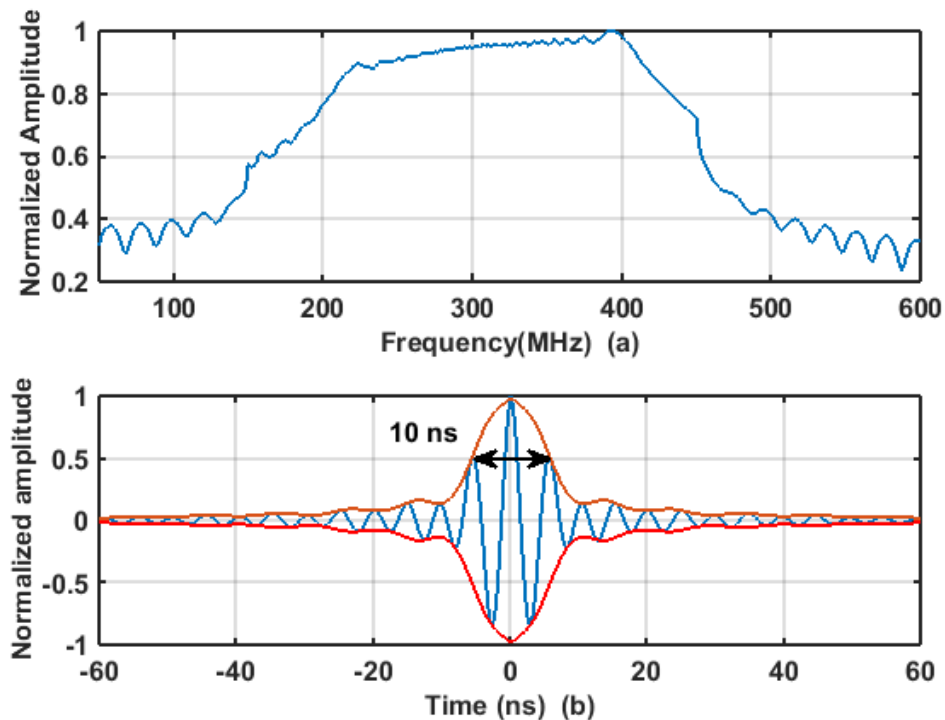


Figure 4.4: (a) Spectrum of the input chirp signal generated by the arbitrary waveform generator. (b) Theoretical shortest pulse, as obtained by Fourier transforming the spectrum of the input chirp signal assuming constant spectral phase. The full-width at half-maximum (FWHM) is 10 ns [79].

input electrical circuitry.

A plane mirror is used in place of the sample and the path length is varied using the phased mirror to obtain the total voltage span (V_{span}) of the interferometer. As the path difference changes, the amplitude of the interferometer signal oscillates within a given voltage range. The measurements are shown in Fig. 4.7. The total V_{span} is given by Eq. (4.8)

$$V_{span} = V_{max} - V_{min} = 1.285V - 0.008V = 1.277V \quad (4.8)$$

$$SNR = \frac{V_{max}}{V_{rms}} \quad (4.9)$$

$$\Delta u = \frac{\lambda V_{max}}{2V_{span}} \quad (4.10)$$

The signal-to-noise ratio (SNR) of the measurements is calculated using Eq. (4.9). The amplitude of the ultrasonic displacement is calculated using Eq. (4.10). Table. 4.1 shows the chirp amplitude measurements for different amplifications. The SNR and the displacement values for these respective measurements are shown in Table. 4.2. The detection limit for each case is calculated assuming $SNR = 1$.

The SNR value for the interferometric measurement is close to 900, while that of the electrical measurement is close to 9000, for the results displayed in Fig. 4.8 and Fig. 4.9. As a result the optical detection is about 10 times less sensitive than the electrical detection. However, optical detection can be performed at an arbitrary location on the surface of the sample, while electrical detection is only possible at the location of the output IDT. Furthermore, electrical

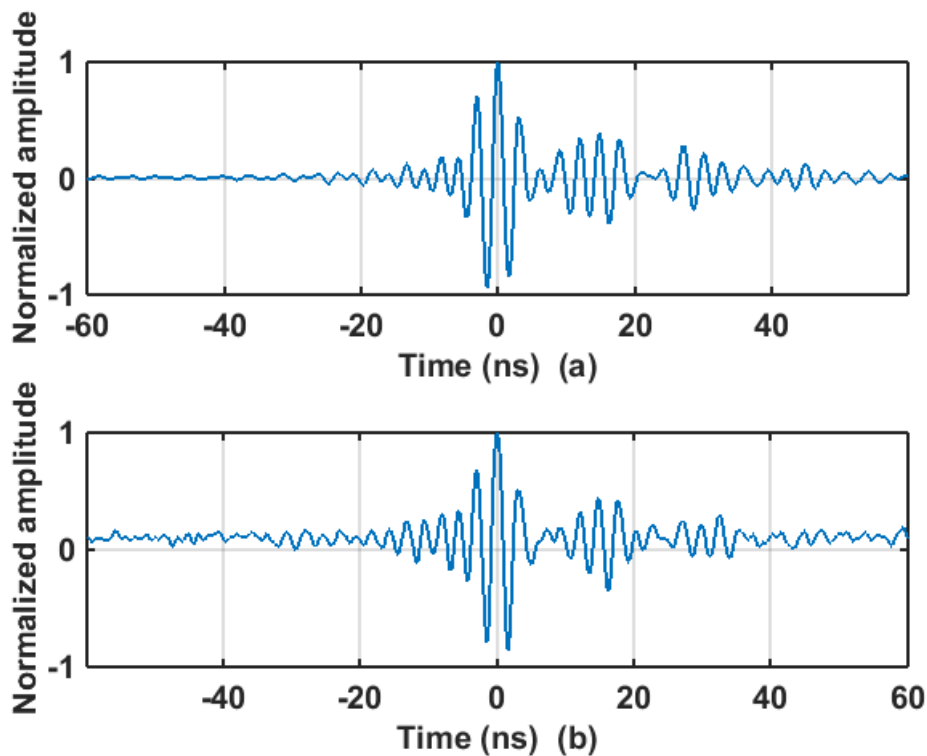


Figure 4.5: (a) Electrical measurement and (b) interferometer measurement, at the location of the output interdigital transducer [79].

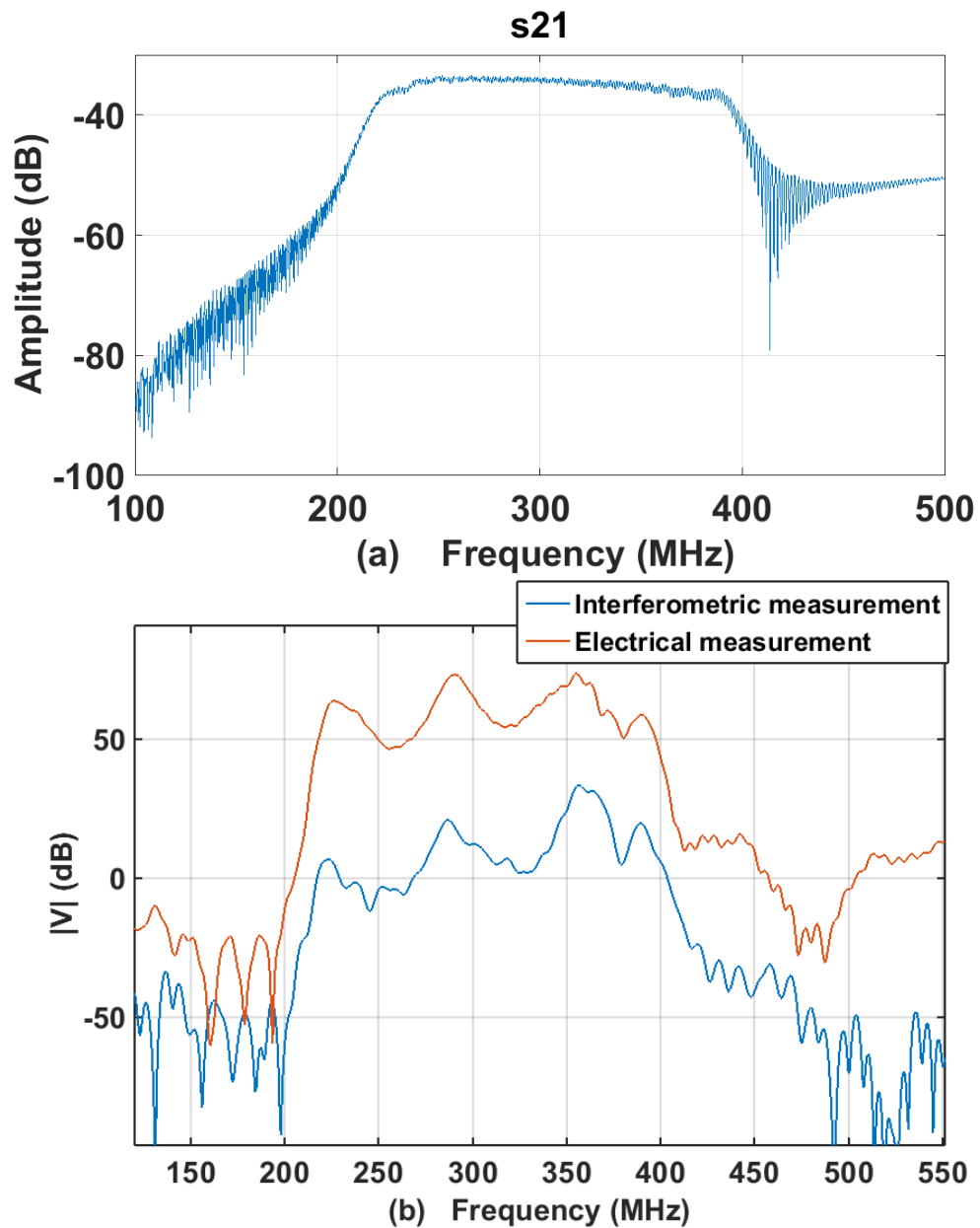


Figure 4.6: (a) S12 measurement of the SAW device obtained using a network analyser and (b) A frequency domain representation of the electrical and interferometric measurements shown in Fig. 4.5

detection involves integration along all the acoustic aperture, or $800 \mu\text{m}$, while optical detection is performed at the laser focus, within an area smaller than $4 \mu\text{m}^2$.

Possible directions of improvement include optimizing the optical power loss in the setup. For the measurements that are presented, the optical beams suffer a 55.8% amplitude loss as calculated using measurements shown in Table. 4.3. Other possible improvements include correction of slight misalignment of the optical components and polarization of laser beams, and compensation of slight differences in the width of the beams passing through the objective.

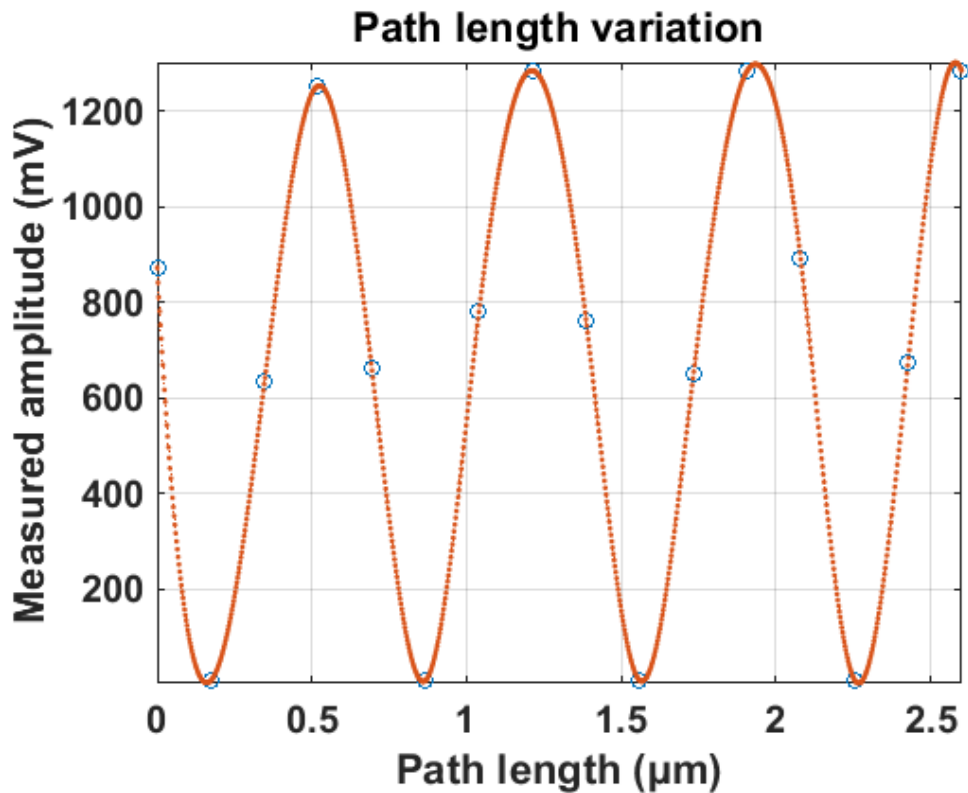


Figure 4.7: A plot showing the total voltage span of the interferometer obtained by varying the path difference between the beams along the two reference arms using a phased mirror.

Table 4.1: Amplitude measurements of the chirp with different attenuations for SNR estimations.

Attenuation (dB)	Input chirp voltage(V)	Measurements with SAW	
		Electrical (mV)	Optical (mV)
15	1.0	1.3e3	145.79
	0.5	715.00	70.87
25	0.5	228.52	21.44
35	0.5	77.50	6.37
45	0.5	23.97	2.25
0	1.0	24.75	2.29

4.5/ Pulse compression along the chirped IDT

Time-delay operation was further checked by repeating the interferometric measurement for different values of the path length difference $L_2 - L_1 = c \Delta t$. The results are presented in Fig. 4.8 and compared with Eq. (4.4) using the theoretical pulse of Fig. 4.4(b). The experimental result is found to be consistent with the theoretical result and shows that the dynamic response of the interferometer can be adjusted depending on the duration of the pulse that is to be measured. For the central 300 MHz frequency that is used here, the path length difference giving the optical measurement was found to be around 30 cm. Clearly, this distance would be reduced in proportion for shorter pulses, i.e. larger SAW carrier frequencies.

Table 4.2: SNR and displacement calculations using measurement values from Table. 4.1.

Attenuation (dB)	V_{rms} (mV)		SNR		Δu (nm)	Detection Limit (pm)	
	Electrical	Optical	Electrical	Optical		Electrical	Optical
15	0.143	0.163	9090.9	894.4	36.98	4.07	41.35
	0.153	0.143	4673.2	495.6	18.06	3.86	36.44
25	0.071	0.117	3218.6	183.2	5.35	1.66	29.20
35	0.071	0.110	1091.5	57.9	1.62	1.48	27.98
45	0.070	0.113	342.4	19.9	0.57	1.66	28.64
0	0.007	0.070	3535.7	32.7	0.58	0.16	17.74

Table 4.3: Amplitude measurements at the output of every optical component of the interferometer.

Optical component	Measured amplitude (mW)
Laser output	6.80
Half wave plate	6.78
Polarising beam splitter 1	6.48
Quarter wave plate	6.41
Sample	5.84
Polarising beam splitter 1	3.00
Half wave plate	2.99
Homodyne part	
Reference arm 1	1.49
Quarter wave plate (arm 1)	1.48
Reference arm 2	1.47
Quarter wave plate (arm 2)	1.45
Polarising beam splitter 2	2.79
Quarter wave plate	2.77
Polarizing beam splitter 3	2.73

For this optimal path length difference, we estimated the maximum amplitude of the surface displacements as follows. The total voltage output was first calibrated with the PID off by sweeping the moving mirror position over a path length difference larger than one optical wavelength. Switching the PID on, it was then determined that the measurement scale in Fig. 4.8 converts to a full range of 36 nm. The actual detection limit was further determined from the root-mean-square (rms) noise value obtained with the PID on but with the SAW signal off. Conversion to amplitude vibration gives a value of 40 pm for the detection limit.

Interferometric measurements were repeated at different locations along the SAW beam path from the exit of the chirped IDT to the output IDT. It was found that the SAW pulse shape showed very little distortion as a function of position. More interestingly, measurements were performed along the chirped IDT, from the left side ($x=0$) to the right side ($x=1800\ \mu\text{m}$), as shown in Fig. 4.8. On the left side, the SAW pulse is so dispersed that its amplitude is very low. As the measurement position is moved to the right, the compressed pulse is seen to emerge as more and more frequency components become synchronized. At the right side of the chirped IDT, all frequency components are in phase and add up to form the final 10-ns pulse.

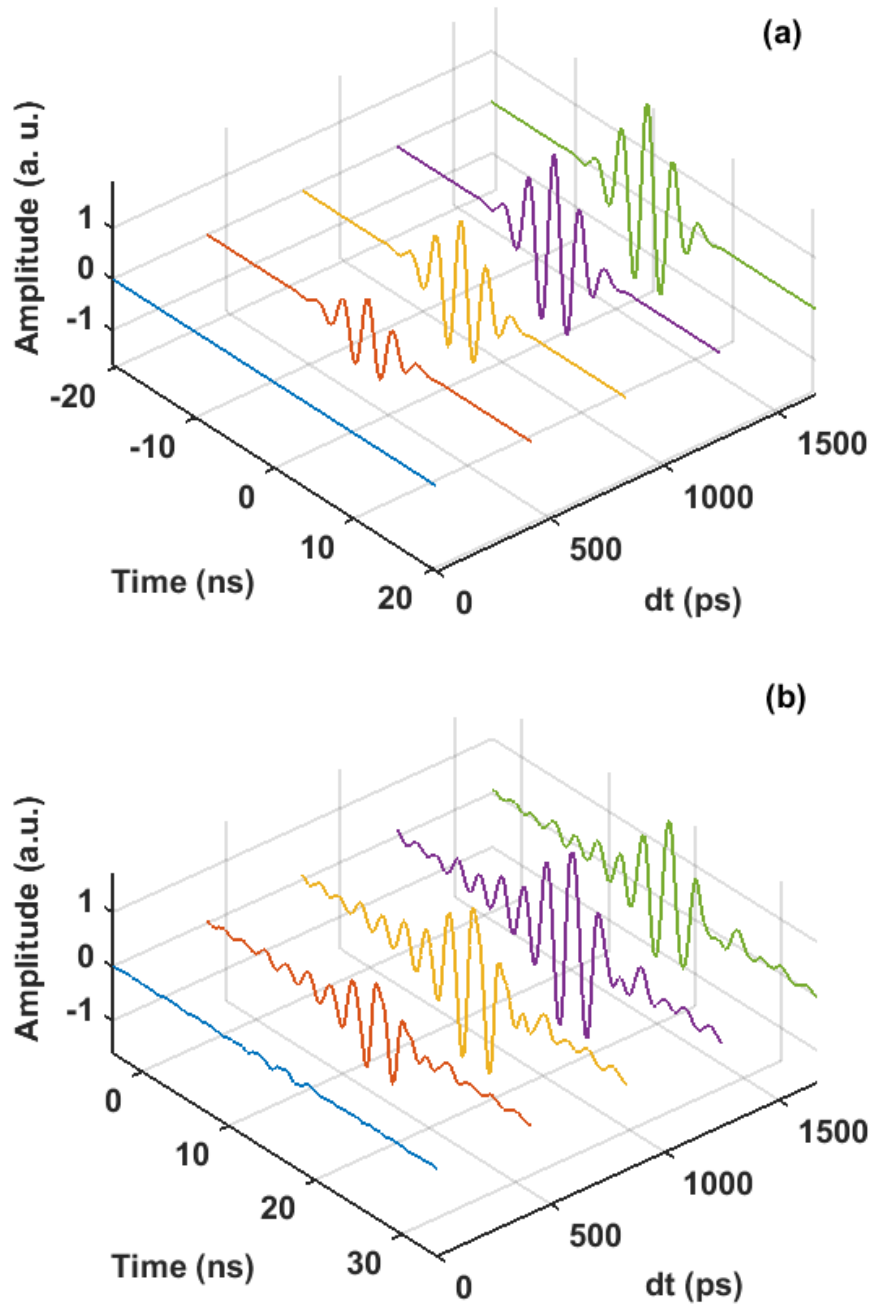


Figure 4.8: Dependence of the pulse measurement with the time-delay Δt . (a) Plot of $\Delta u(x, t)$ at a given position as a function of Δt , for a 10-ns Gaussian pulse. (b) Experimental result as a function of Δt obtained by changing the path length difference in the interferometer [79].

4.6/ Conclusion

In this chapter the working principle of the differential interferometer has been described and a mathematical analysis of the interferometric measurement has been presented. The results of an experiment devised to measure and analyze the operation of this interferometer, have been discussed. A good signal-to-noise ratio for the interferometer setup is obtained that, even

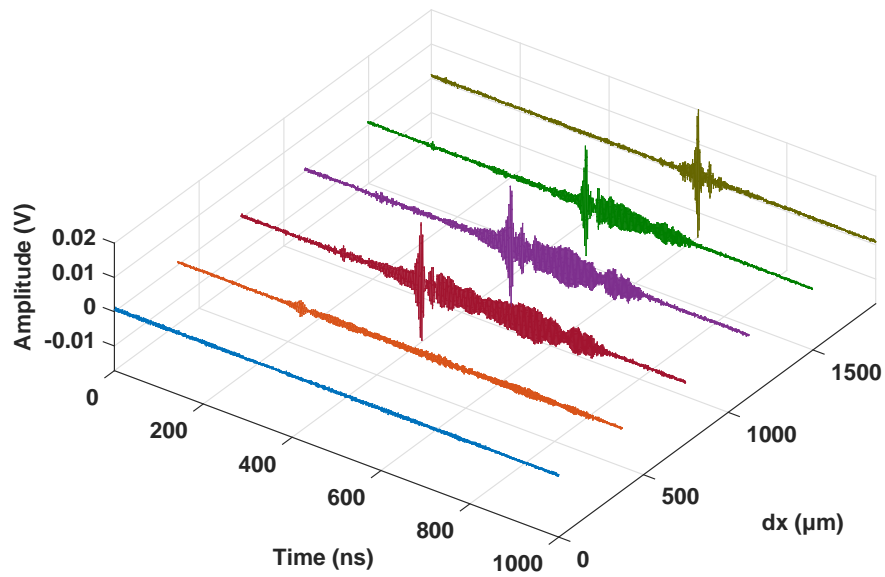


Figure 4.9: Measurement of the SAW pulse at various positions along the chirped interdigital transducer [79].

though is not as high as the electrical measurements, yet, is high enough to measure short pulses with displacements in the order of picometers, with a good accuracy.

Pulse compression and optimization of a short pulse

Pulse compression, as described in section 2.3, involves an implementation of a filter system for a frequency modulated signal which allows to obtain a short pulse. The pulse compression ratio is the ratio of the width of the expanded pulse to that of the compressed pulse. The pulse compression ratio is also equal to the product of the time duration and the spectral bandwidth (time-bandwidth product) of the transmitted signal or in other words, the processing gain as described in chapter 3.

In this chapter we study pulse compression and methods to obtain the optimal pulse using the modelled and measured responses of the fabricated SAW devices described in chapter 3, with an operational bandwidth of 200 MHz-400 MHz. A processing gain value of 100 is used. We present the results for both cases and discuss the possibility of optimization of the short pulse to obtain a better pulse compression ratio.

5.1/ Short pulse evaluation using simulated Chirps

Using the p-matrix model described in section 2.2.3.4, three different types of chirps, as described in section 3.1.2, are generated and shown in Fig. 5.1. The power amplitudes $|a_1|$ and $|a_2|$, of the waves travelling left and right respectively, are obtained for every electrode along the chirped IDT and the total response $H(x, \omega)$ due to the superposition of both waves is given by

$$H(x, \omega).e^{i\omega t} = a_1(x, \omega).e^{i(\omega t - kx)} + a_2(x, \omega).e^{i(\omega t + kx)} \quad (5.1)$$

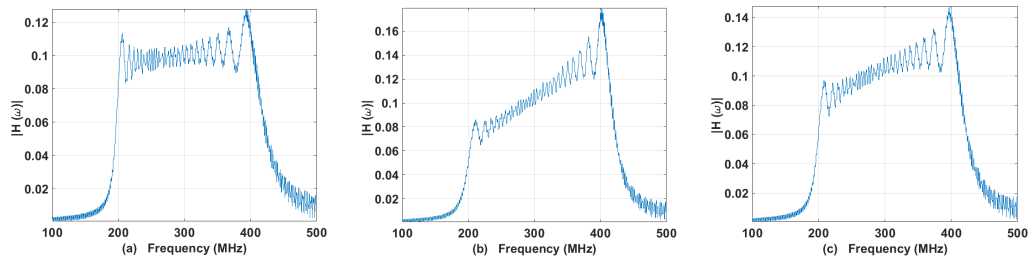


Figure 5.1: $|H(\omega)|$ for (a) a linear chirp, (b) a hyperbolic chirp and (c) a mean chirp, obtained using a p-matrix model.

where $\omega = 2\pi f$, is the angular frequency, k is the wave number, x is the position on an IDT such that $x = 0$ at the first electrode on the left of the IDT and is positive along its length on the right. We use the CIDT response exiting on the right hence we can write $H(x, \omega)$ as $H(\omega)$ since it is independent of x . $H(\omega)$ represents the filtering process by the IDT and hence is chosen to be represented without units. The inverse Fourier transform of this response ($H(\omega)$) gives the waveform $H(t)$, as seen in figure 5.2, for each chirp.

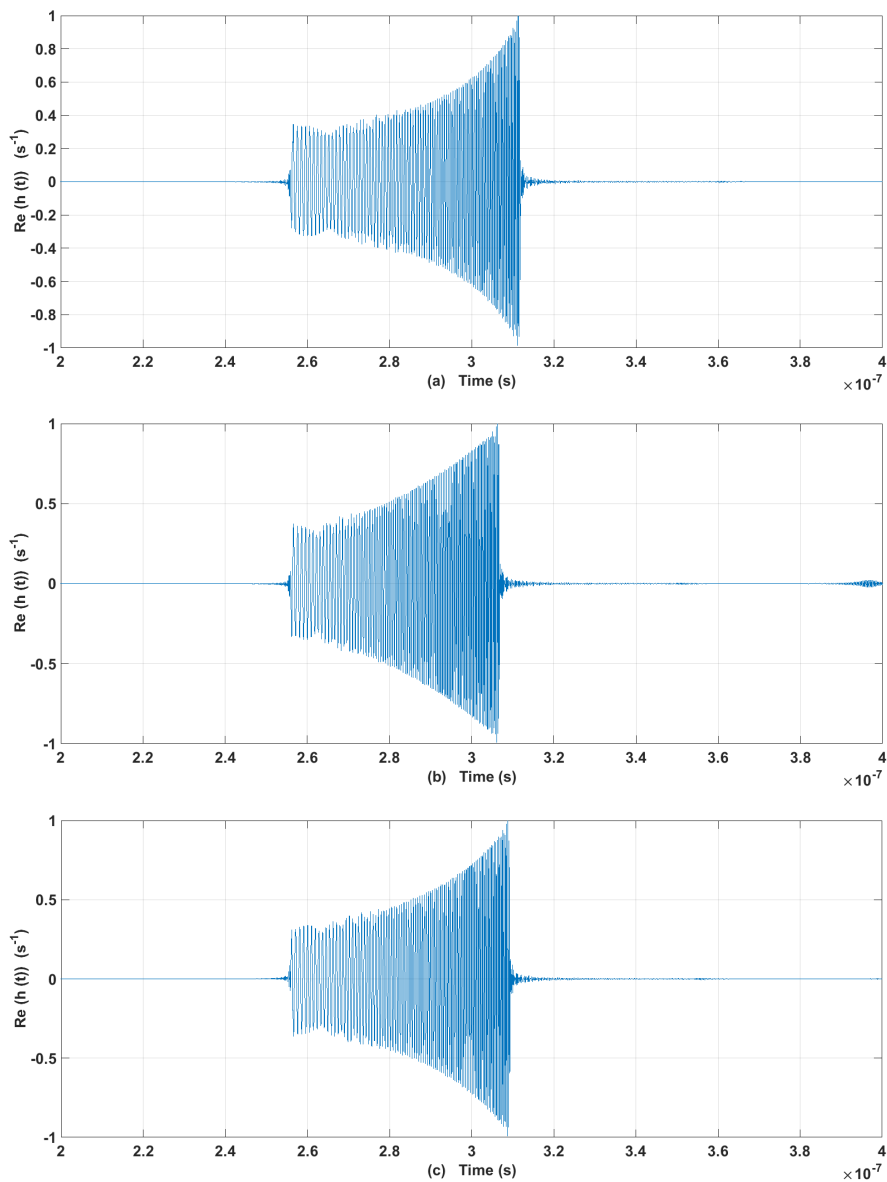


Figure 5.2: Normalized waveforms obtained for (a) a linear chirp, (b) a hyperbolic chirp and (c) a mean chirp, by performing an inverse Fourier transform on the responses calculated using a p-matrix model as shown in figure 5.1.

5.1.1/ The input chirp

In order to obtain a short pulse, an input chirp is sent to the SAW device through an arbitrary waveform generator (AWG) used for the experiments in chapter 4, section 4.3. In this section,

in order to find the optimal pulse, three different types of filters for the input chirp are designed to obtain a short pulse and the results are discussed in the following sections.

5.1.1.1/ Filter 1

A matched filter is designed for each of the three chirped IDTs, by taking the complex conjugate of the transmission response of the CIDTs. A multiplicative factor M , is used to balance the units such that the units of the input filter response is V.s. The response of this filter is

$$H(\omega)_{I1} = M.H(\omega)^* \quad (5.2)$$

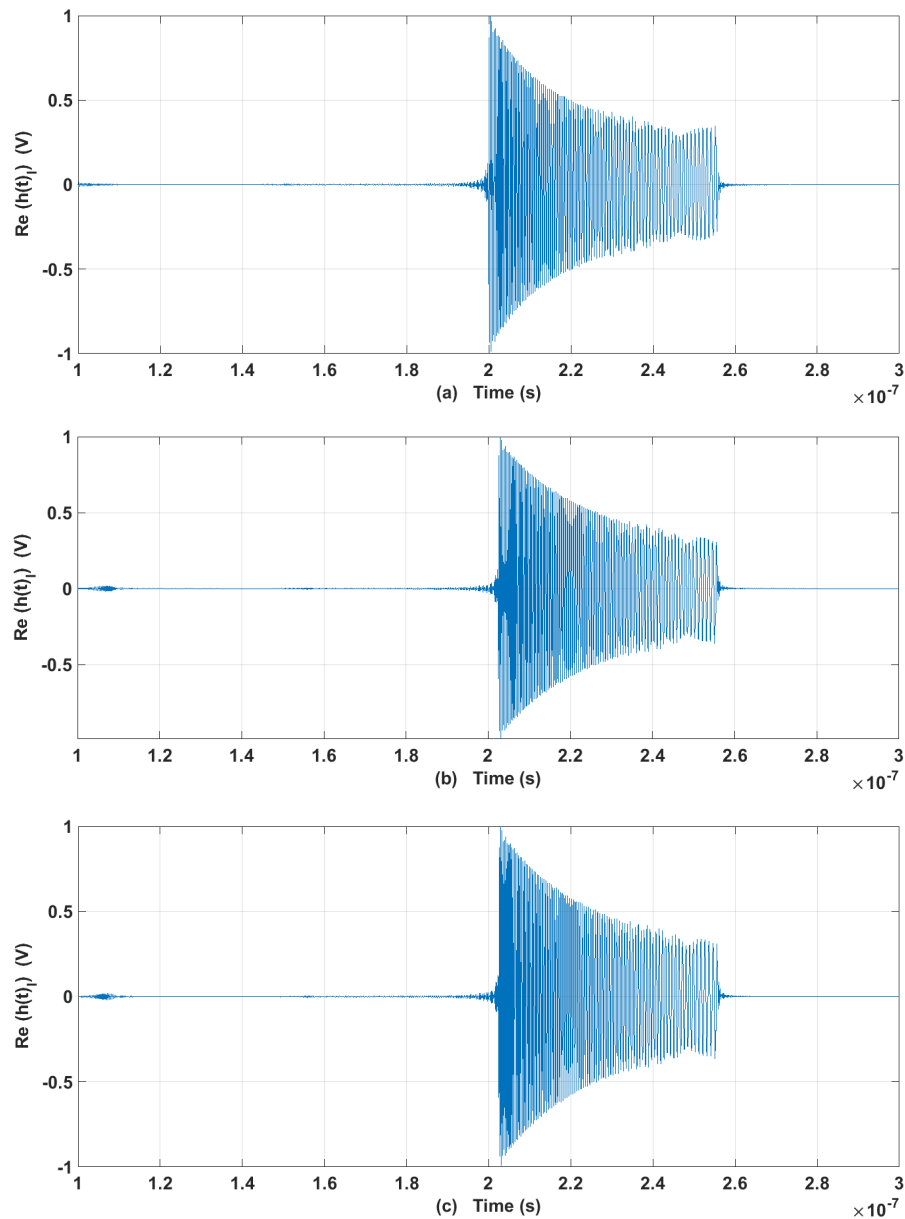


Figure 5.3: Normalized input chirp waveforms obtained by performing an inverse Fourier transform on the response of filter 1 ($H(\omega)_{I1}$) for (a) a linear chirp, (b) a hyperbolic chirp and (c) a mean chirp, obtained using a p-matrix model.

Figure 5.3 shows the normalized input chirp waveforms obtained by performing inverse Fourier transform on the filter response generated using equation 5.2. The value of M is not important because the waveform $h(t)_I$ is normalized between +1 V and -1 V. The duration of each chirp is ≈ 500 ns. The effect of the pitch variation can be observed by noting the variation in the waveform envelopes for each case. As expected, the input chirps for each case look like a time reversal image of the respective transmission waveforms show in figure 5.2.

5.1.1.2/ Filter 2

An inverse filter $H(\omega)_{inv}$ is designed as shown in Fig. 5.4(a) using equation 5.3 where C is a multiplicative factor used to balance the units, such that the units for inverse filter response $H(\omega)_{inv}$, is V.s. In order to equalize the spectral response by suppressing the high values generated for the frequencies outside the bandwidth of interest, the inverse function is multiplied by a window $G(f)$ designed using equation 5.4.

$$H(\omega)_{inv} = \frac{C}{H(\omega)} \quad (5.3)$$

$$G(f) = \frac{1}{2} \left(\tanh \left(\left| \frac{f_n - f_1}{B_0} \right| \right) - 1 \right) \cdot \left(\tanh \left(\left| \frac{f_2 - f_n}{B_0} \right| \right) - 1 \right) \quad (5.4)$$

$$H(\omega)_{I2} = H(\omega)_{inv} \cdot G(f) \quad (5.5)$$

where f_1 and f_2 are the limiting frequencies of the bandwidth of interest which in this case are 200 MHz - 400 MHz, B_0 is an arbitrary tuning factor of the same order as the limiting frequencies of the bandwidth, used to manipulate the window in order to optimize the inverse chirp to obtain a short pulse with a high A_p value. The designed window is shown in Fig 5.4 (b). The value of the constant C is not important because the waveform $h(t)_I$ is normalized between +1 V and -1 V.

The final inverse chirp $H(\omega)_I$ is obtained using equation 5.5. The waveforms of the inverse filters for each chirp is obtained by performing an inverse Fourier transform on the inverse chirp

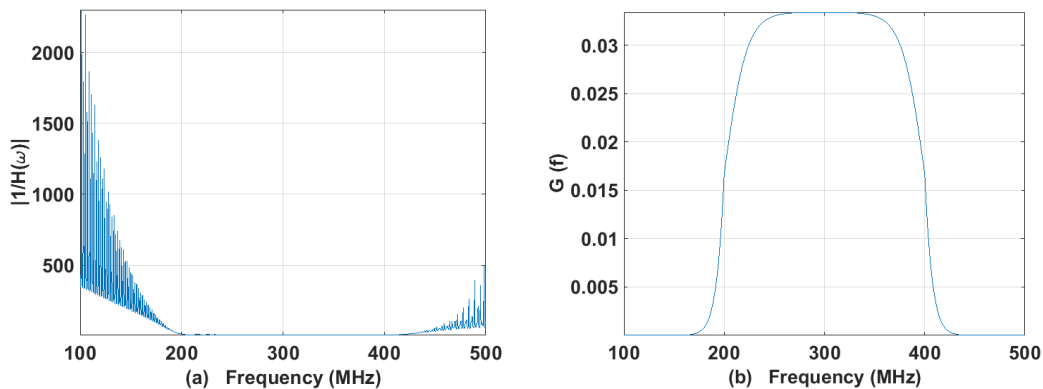


Figure 5.4: (a) A plot showing the inverse of the $H(\omega)$ function for a linear CIDT, and (b) a window function $G(f)$ obtained using equation 5.4.

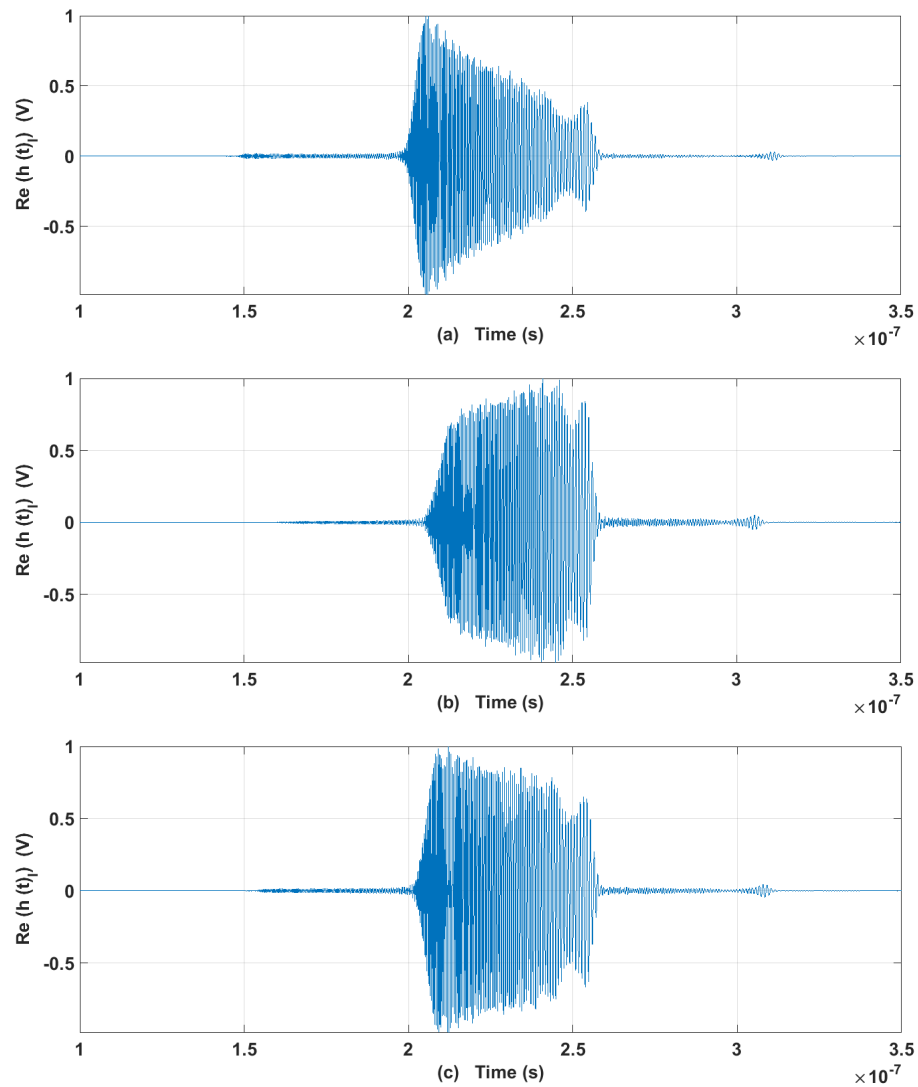


Figure 5.5: Normalized inverse chirp waveforms for filter 2, obtained for (a) a linear chirp, (b) a hyperbolic chirp and (c) a mean chirp, using a p-matrix model.

filter response. The B_0 value used to obtain the waveform shown in fig. 5.5 is $B_0 = 22.5$ MHz. Dispersion in the energy distribution for the three different chirps is clearly visible.

As explained in chapter 3, section 3.1.1, the processing gain to obtain a compressed pulse for the design is chosen to be 100 for a bandwidth of 200 MHz, which gives an interrogation signal with a duration of 500 ns as calculated in equation 3.9, as shown in figure 5.3, 5.5, and 5.6.

5.1.1.3/ Filter 3

In this case, the input chirp obtained using equation 5.2 for filter 1, is fine tuned using a window described in section 5.1.1.2, by equation 5.4. The B_0 value used for this case, to obtain the chirp waveforms shown in figure 5.6, is 22.5 MHz. The response of filter 3 is given by

$$H(\omega)_{I3} = H(\omega)_{I1} \cdot G(f) \quad (5.6)$$

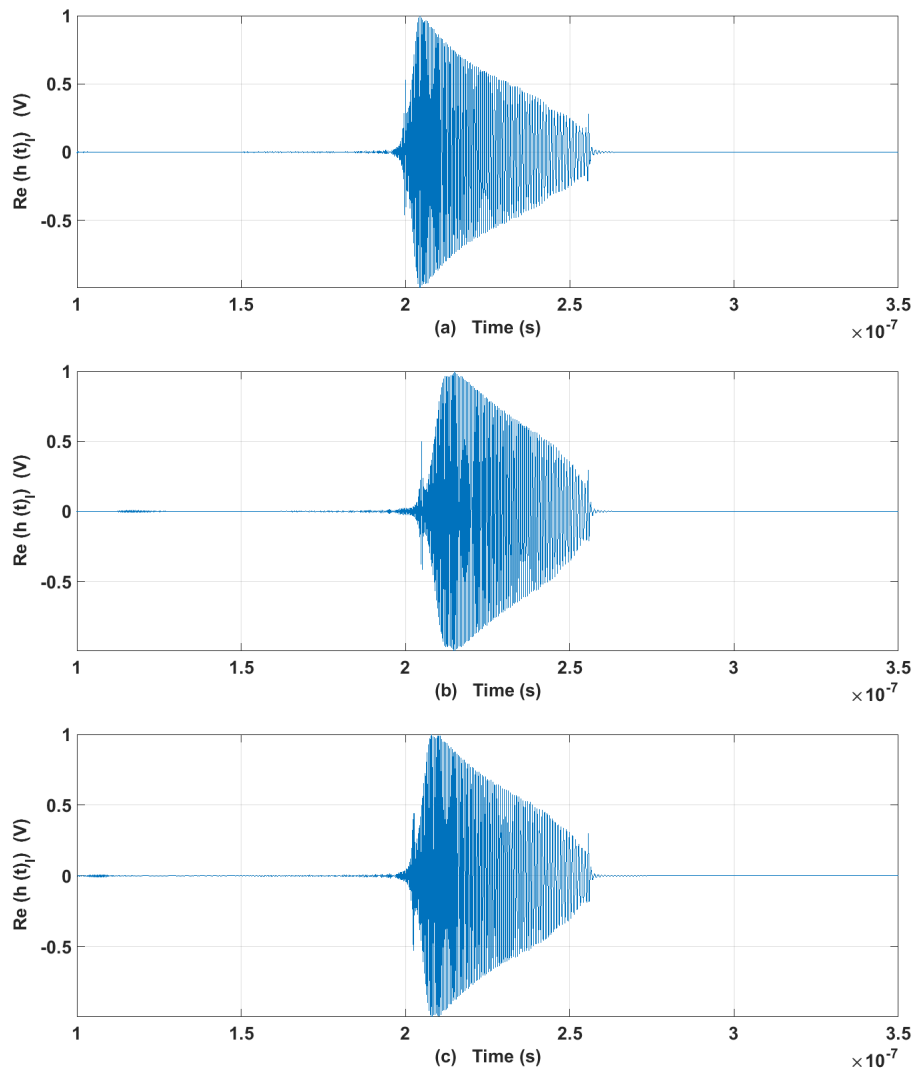


Figure 5.6: Normalized input chirp waveforms obtained for filter 3, by windowing the transmission response of filter 1 for (a) a linear chirp, (b) a hyperbolic chirp and (c) a mean chirp.

For a signal with variable frequency, the corresponding input filter required for the generation of a short pulse is necessarily dispersive and the slope of its group delay - frequency characteristic is opposite to the slope of the instantaneous frequency modulation of the response as observed from figures 5.2, 5.3, 5.5, and 5.6. The dispersive effect explains the pulse compression. In this case the high frequency components forming the beginning of the signal are retarded longer by the filter than the low frequency components arriving at the end of the signal.

For filter 1, the slope of the waveform envelope is exactly opposite of that of the waveforms shown in figure 5.2. However, that is not the case for filter 2 and filter 3 input chirps. The slope of the waveform envelope is distinctly different. For filter 2, although, the slope is opposite of that of the transmitted signal waveforms, gradual variations in the slope are observed. The energy distribution is better for the mean chirp compared to the linear and the hyperbolic chirp case, as seen in figure 5.5. For type 3, as shown in figure 5.6, the slopes and consequently, the amplitude modulation for the frequency components are fairly different. The value of $h(t)$ for the low frequencies is much lower compared that of the high frequencies. This trend described above, is observed for all the three chirp cases.

5.1.2/ Short pulse

The convolution product of the CIDT response at the last electrode giving the transmitted chirp, and the input chirp optimized for that, produce a short pulse $p(t)$, given by equation 5.7, where $m=1,2$, and 3 represent the three filter types, as shown in Figures 5.7, 5.8, and 5.9. The input chirp combines with the transmitted response and adjusts the phase of each frequency component accordingly to produce this short pulse. The width of the compressed pulse obtained is 10 ns for each chirp.

$$p(t) = \frac{1}{2\pi} \int_{-\infty}^{+\infty} H(\omega) \cdot H(\omega)_{Im} \cdot e^{i\omega t} d\omega \quad (5.7)$$

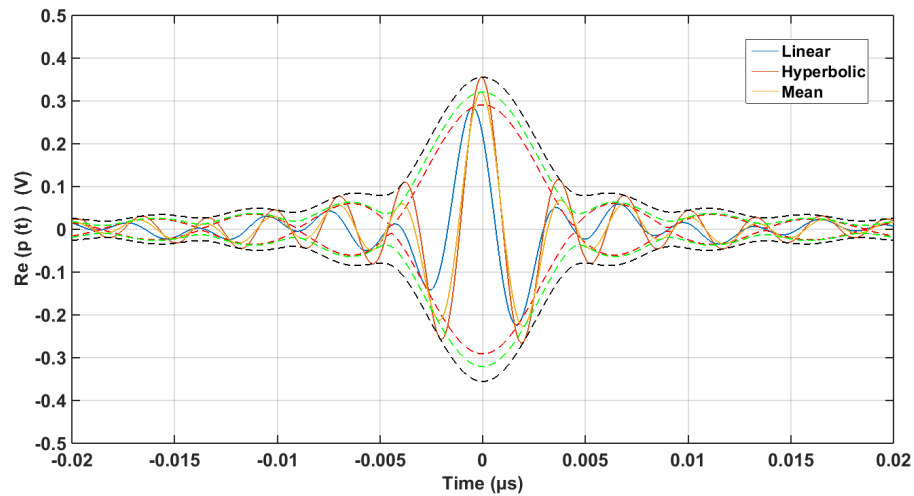


Figure 5.7: Short pulses $p(t)$, obtained for the three chirp cases, by using filter 1, when the threshold condition is applied on the input chirp waveform.

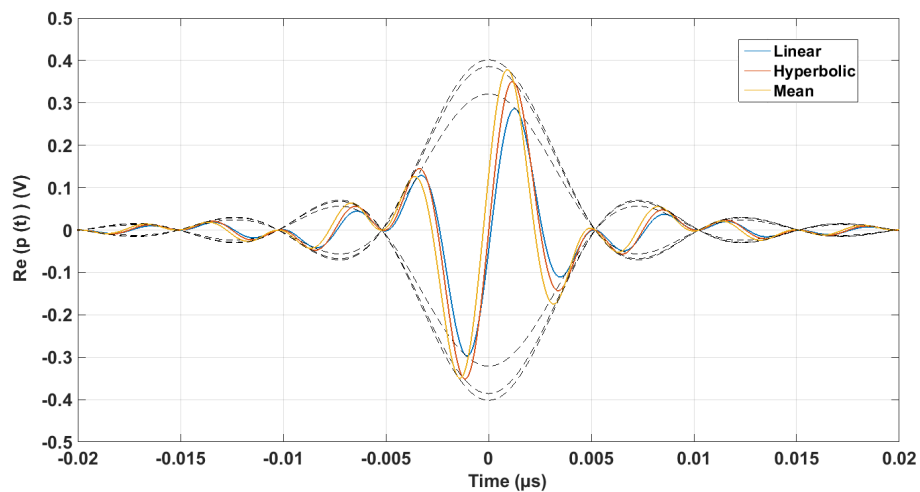


Figure 5.8: Short pulses $p(t)$, obtained for the three chirp cases, by using filter 2, when the threshold condition is applied on the input chirp waveform.

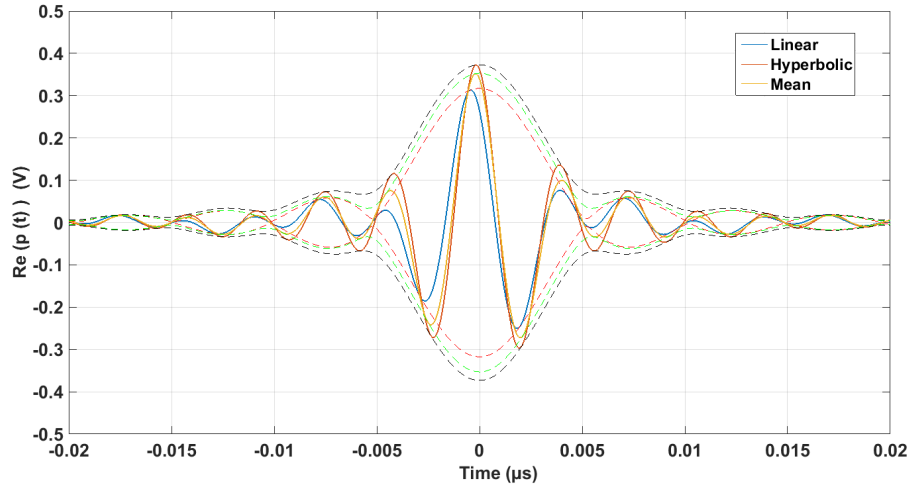


Figure 5.9: Short pulses $p(t)$, obtained for the three chirp cases, by using filter 3 when the threshold condition is applied on the input chirp waveform.

From the above equation, the unit for the pulse response $p(t)$ in time domain, is calculated to be Volts (V). The mean arrival time of the pulse is given by t_0 in equation 5.8. The peak A_p value of the short pulse is the modulus

$$t_0 = \frac{\langle t|P(t, x)|^2 \rangle_t}{\langle |P(t, x)|^2 \rangle_t} \quad (5.8)$$

$$A_p = |P(t_0)| \quad (5.9)$$

In order to obtain the maximum peak A_p value, of the short pulse, a threshold condition is applied on the input chirp waveforms corresponding to the threshold of the AWG used for the measurements of transmitted responses of the fabricated SAW devices, as described in section 5.2, to send the input chirp with the maximum amplitude possible.

Figure 5.7 shows the short pulses $p(t)$ obtained using filter 1 input chirps. The width W_p , of the pulse is ≈ 10 ns for each chirp. However, a variation in A_p , is observed for the different chirp cases. For the linear case, $A_p = 0.29$ V, for the hyperbolic case, $A_p = 0.36$ V, and for the mean chirp case, $A_p = 0.33$ V as listed in table 5.1. The short pulse produced after pulse compression, for the hyperbolic case has the maximum value for A_p . No change in the pulse width due to the pitch variation of the CIDT, is observed.

Figure 5.8 shows the short pulses $p(t)$ obtained using filter 2 chirps. The width W_p , of the pulse is ≈ 10 ns for each chirp. When the threshold condition is applied, a variation of the pulse shape compared to the previous case, as well as a change in the peak A_p value is observed for the respective chirp cases. From table 5.1, it can be concluded that in this case the short pulse for the mean chirp has the highest peak A_p value.

Figure 5.9 shows the short pulses $p(t)$ obtained using filter 3 input chirps. The width W_p , of the pulse is ≈ 10 ns for each chirp as expected. Like in the case of filter 1 chirps, a variation in the peak A_p value, is observed for the different chirp cases. After the application of the threshold condition, for the linear case, $A_p = 0.35$ V, for the hyperbolic case, $A_p = 0.37$ V, and for the mean chirp case, $A_p = 0.32$ V. The short pulse produced after pulse compression, for the hyperbolic case has the maximum value of A_p . No change in the pulse width due to

Table 5.1: A_p values obtained on application of the threshold condition, for the short pulses generated using different types of input chirps described in section 5.1.1

Input Chirp type	Linear chirp A_p (V)	Hyperbolic chirp A_p (V)	Mean Chirp A_p (V)
Filter 1	0.29	0.36	0.33
Filter 2	0.31	0.38	0.40
Filter 3	0.35	0.37	0.32

Table 5.2: Amplitude gain factor of the short pulse generated using different types of input chirps described in section 5.1.1

Amplitude gain factor (A_{g_n})	Linear chirp	Hyperbolic chirp	Mean Chirp
$\frac{A_{p2}}{A_{p1}}$	1.06	1.06	1.21
$\frac{A_{p2}}{A_{p3}}$	0.88	1.02	1.25

the pitch variation of the CIDT, is observed for this case too.

$$A_{g_n} = \frac{A_{p_m}}{A_{p_n}} \quad (5.10)$$

Here $n = 1$, and 3, and $m = 2$, A_{g_n} is the gain factor and A_{p_n} is the amplitude of the short pulse obtained using the type n input filter design.

The value of A_p for each chirp and the 3 filters are listed in table 5.1. On comparison, it is observed that the width of the short pulse is ≈ 10 ns for all the three type of input chirps (generated by filters 1, 2, and 3) for all the three chirp types (linear, hyperbolic, and mean). However, the peak A_p value of the short pulse generated by filter 2, is higher by a gain factor A_{g_n} , given by equation 5.10, compared to that of the short pulses for the other two filter types. The values for the gain factors A_{g_n} are listed in table 5.2. Hence, filter 2, that generates an inverse chirp, is chosen to generate the input chirp signals for the respective chirp cases.

5.2/ Short pulse evaluation for the Fabricated SAW devices

In this section the function representing the filtering process of the CIDT is $G(\omega) = Z_0|Y|$, where admittance $|Y|$, is in Siemens (S). The admittance measurements for the three different chirps, are shown in figure 5.10. The waveforms $g(t)$, for each chirp obtained using an inverse Fourier transform of $G(\omega)$ are shown in figure 5.11. The effect of the pitch variation for the three chirps is clearly visible in the different waveform shapes. A distinct difference in the shape of the waveforms for each chirp is observed when compared to the simulation results shown in figure 5.2. The higher frequencies have much lower value compared to what is predicted by the modelled responses for each chirp. The frequency components near the central frequencies

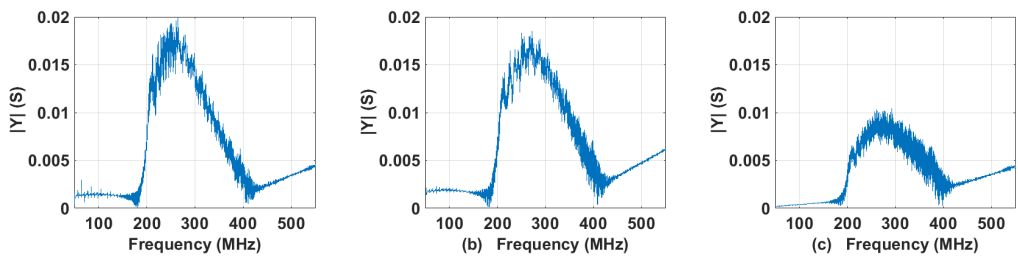


Figure 5.10: Admittance measurements for the transmission, obtained from the fabricated SAW devices with (a) A linear chirp, (b) A hyperbolic chirp and (c) A mean chirp. Chirp bandwidth is 200 MHz - 400 MHz.

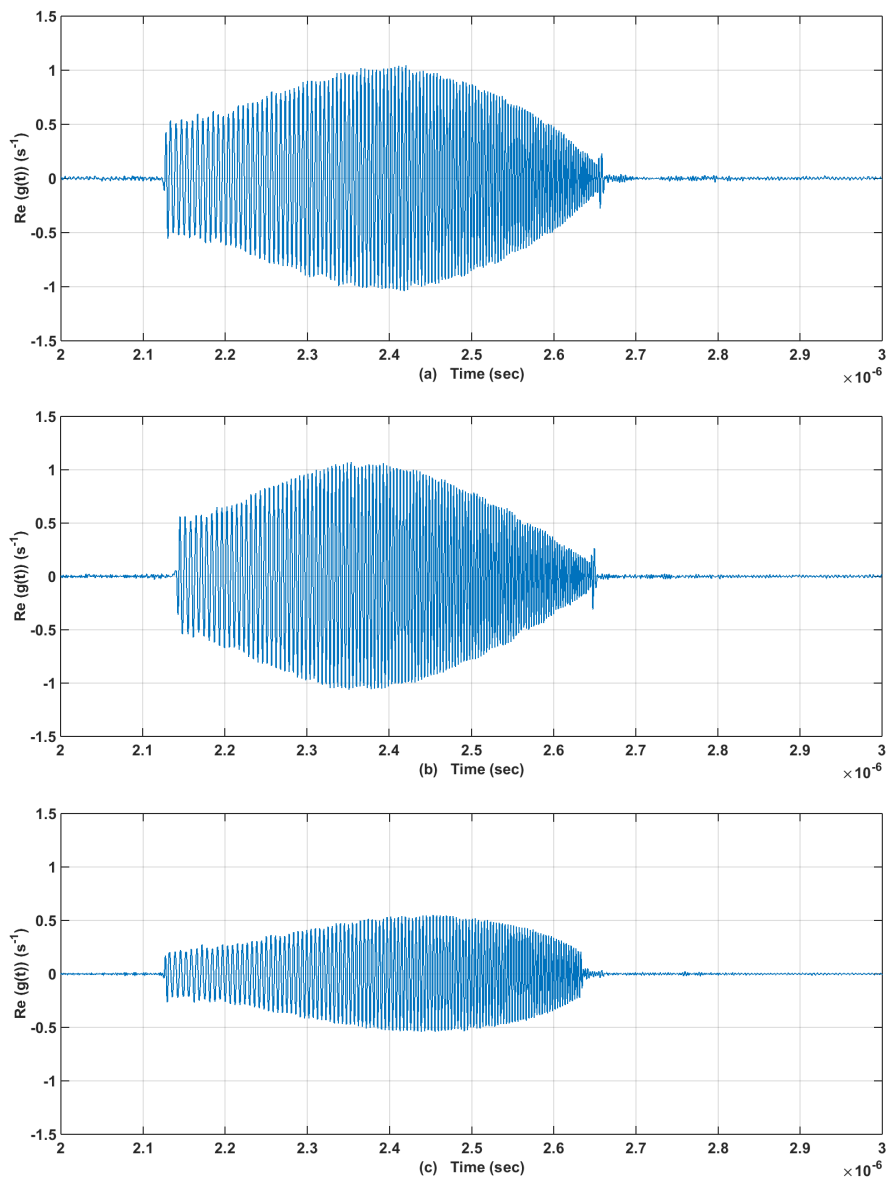


Figure 5.11: Chirp waveforms obtained for (a) a linear chirp, (b) a hyperbolic chirp and (c) a mean chirp, using the admittance measurements shown in figure 5.10.

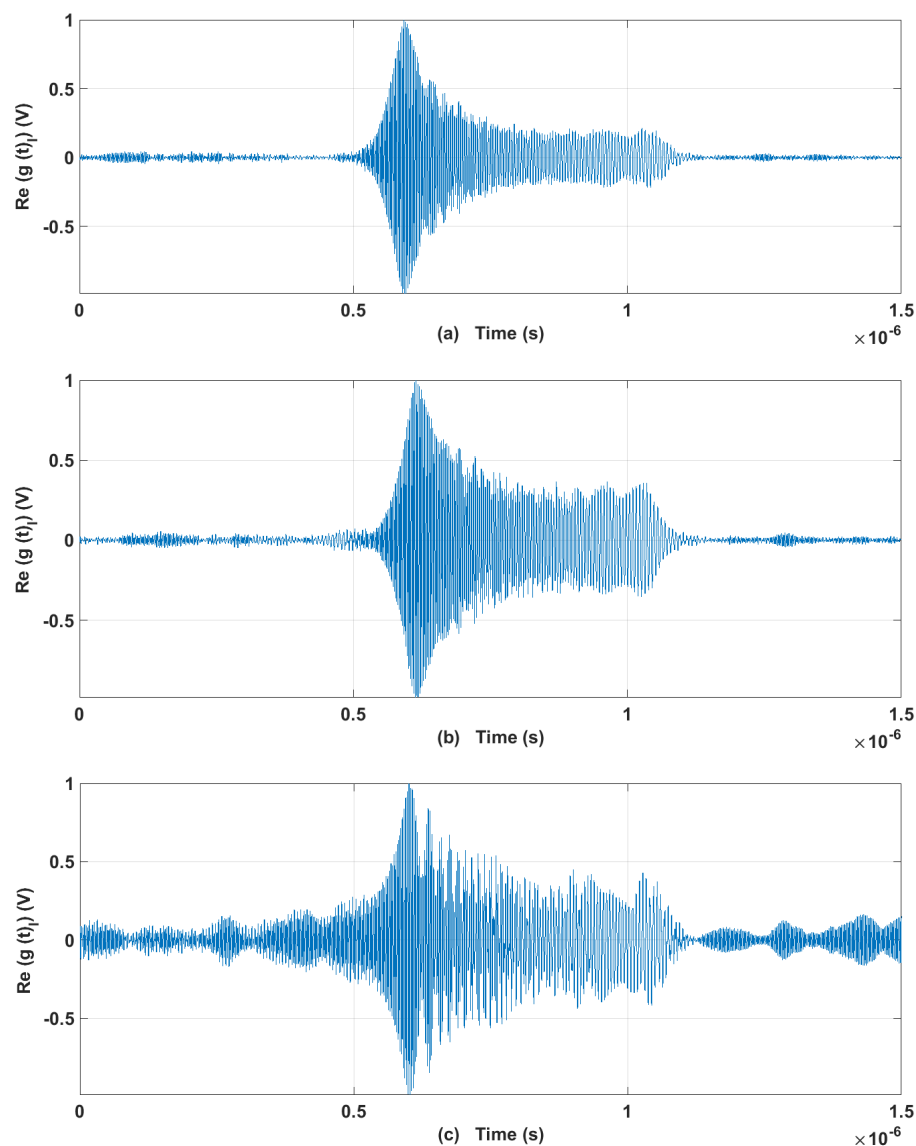


Figure 5.12: Normalized inverse chirp waveforms obtained for (a) a linear chirp, (b) a hyperbolic chirp and (c) a mean chirp, using the admittance measurements shown in figure 5.10.

show higher value compared to the frequency components closer to the limiting frequencies of the bandwidth for all the three cases, The width of the chirp envelope is ≈ 500 ns, as expected. The amplitude of the waveform obtained for the mean chirp is less than that of the waveforms of the other two chirp cases by a factor of 2.

Figure 5.12 shows the normalized inverse chirps $g(t)_I$, for the measured transmission responses of the respective SAW devices $G(\omega)_I$, with differently chirped CIDTs. These inverse chirps are designed using equations 5.3 - 5.5, as described in section 5.1.1.2. The B_0 value used to obtain the waveform shown in fig. 5.12 is $B_0 = 12.5$ MHz. The variation in the shape of the waveforms for the three different chirps is clearly visible.

For the linear chirp case, as shown in figure 5.12 (a), the variation in the value of $g(t)_I$ is fairly uniform for a large part of the chirp ($\approx 3/4$ th of the chirp duration), however it increases rapidly for high frequencies. For the hyperbolic case, as shown in figure 5.12 (b), a similar

trend is observed. However, the energy distribution is much better compared to that of the linear case. The inverse chirp for the mean chirp measurements is extremely noisy as seen in figure 5.12 (c). Signal processing was not used to suppress the noise in the inverse chirp for this case as it would create artifacts in the compressed pulse signal that could be observed as side-ripples near the short pulse in the time domain measurement.

5.2.1/ Pulse compression experiment

The objective of this experiment is to obtain pulse compression and find the optimal inverse chirp, by tuning the window used to design the inverse chirp, that produces a short pulse of a shorter duration and higher amplitude. The B_0 of the window function given in equation 5.3, is varied over a range of 12.5 MHz - 142.5 MHz to obtain a range of inverse filters for each chirped SAW device.

The inverse chirps for the respective SAW devices, obtained using their transmission measurements, are sent as input chirps through an arbitrary waveform generator (AWG; Tektronix, model AWG7122B), to the respective SAW devices, as shown in the schematic setup in figure 5.13. The short pulse signal at the output IDT is measured using an oscilloscope with a 2 GHz bandwidth, 40 GSa/s sample rate and waveform averaging value of 1024 (Agilent, model Infiniium DSO80204B). The sampling frequency used is 10 GSa/s.

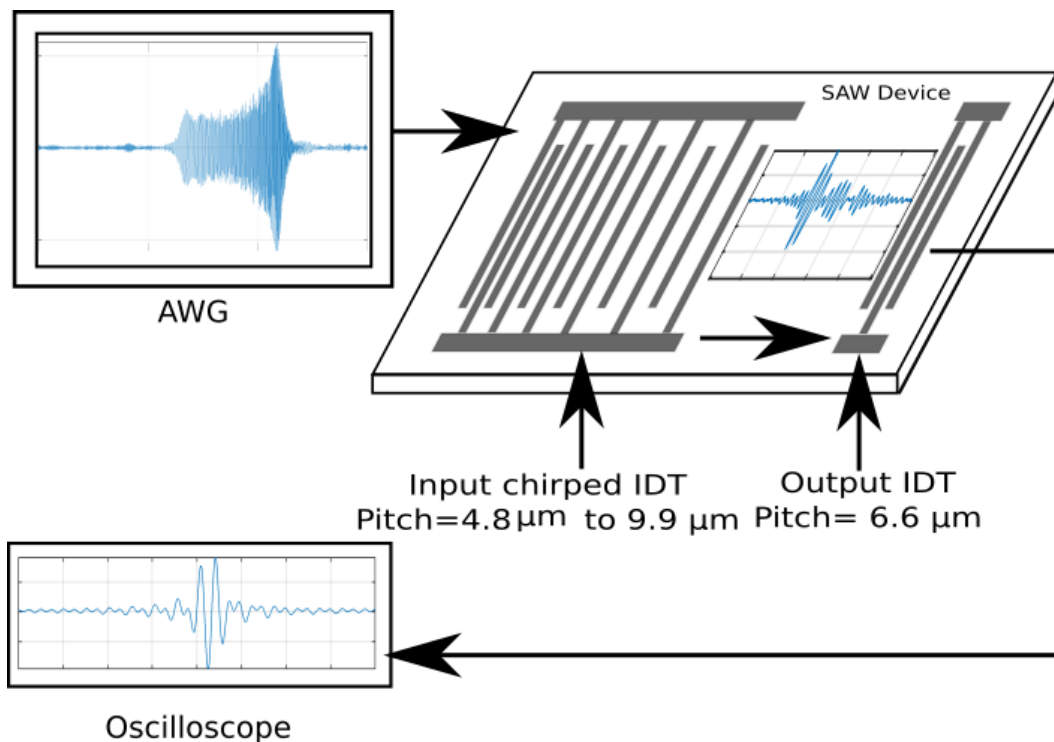


Figure 5.13: A schematic of the pulse compression experiment to measure the responses of the fabricated SAW devices.

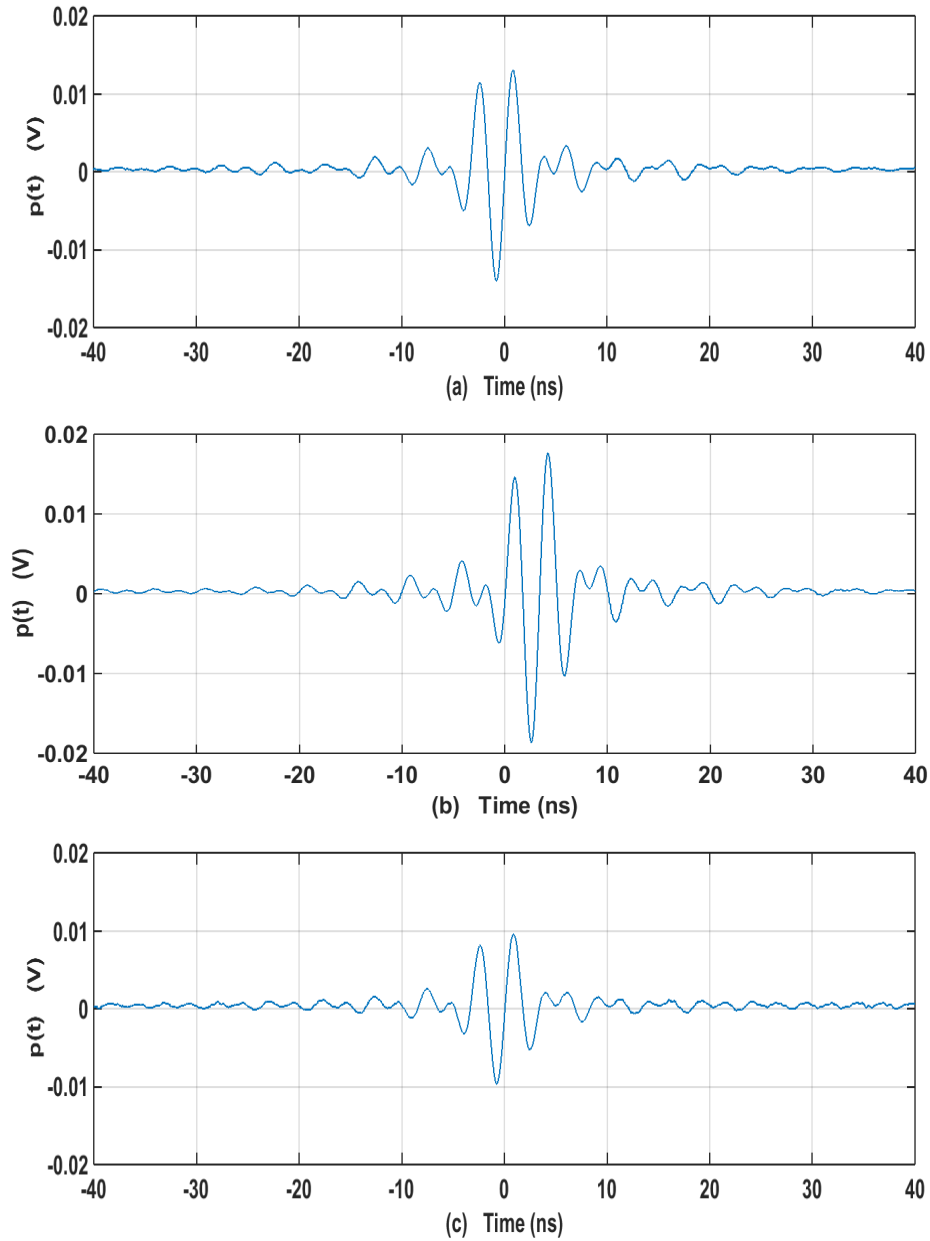


Figure 5.14: Short pulses obtained for (a) a linear chirp, (b) a hyperbolic chirp and (c) a mean chirp.

5.2.2/ Results and discussion

Figure 5.14 shows the short pulses obtained using the inverse chirps for the respective SAW devices when the B_0 value is 12.5 MHz. The pulse width measured for each case is ≈ 10 ns, in accordance with the simulated results shown in figure 5.5. The peak-to-peak value of the short pulse ($p(t)$), generated by the linearly chirped SAW device, is measured to be ≈ 0.025 V, as seen in figure 5.14 (a). For the SAW device with a mean chirped IDT, it is measured to be ≈ 0.02 V as seen in figure 5.14 (c).

However for the hyperbolic case, the peak-to-peak value is the largest compared to the other chirped cases, and it is ≈ 0.04 V, as seen in figure 5.14 (b). The B_0 value is chosen to be

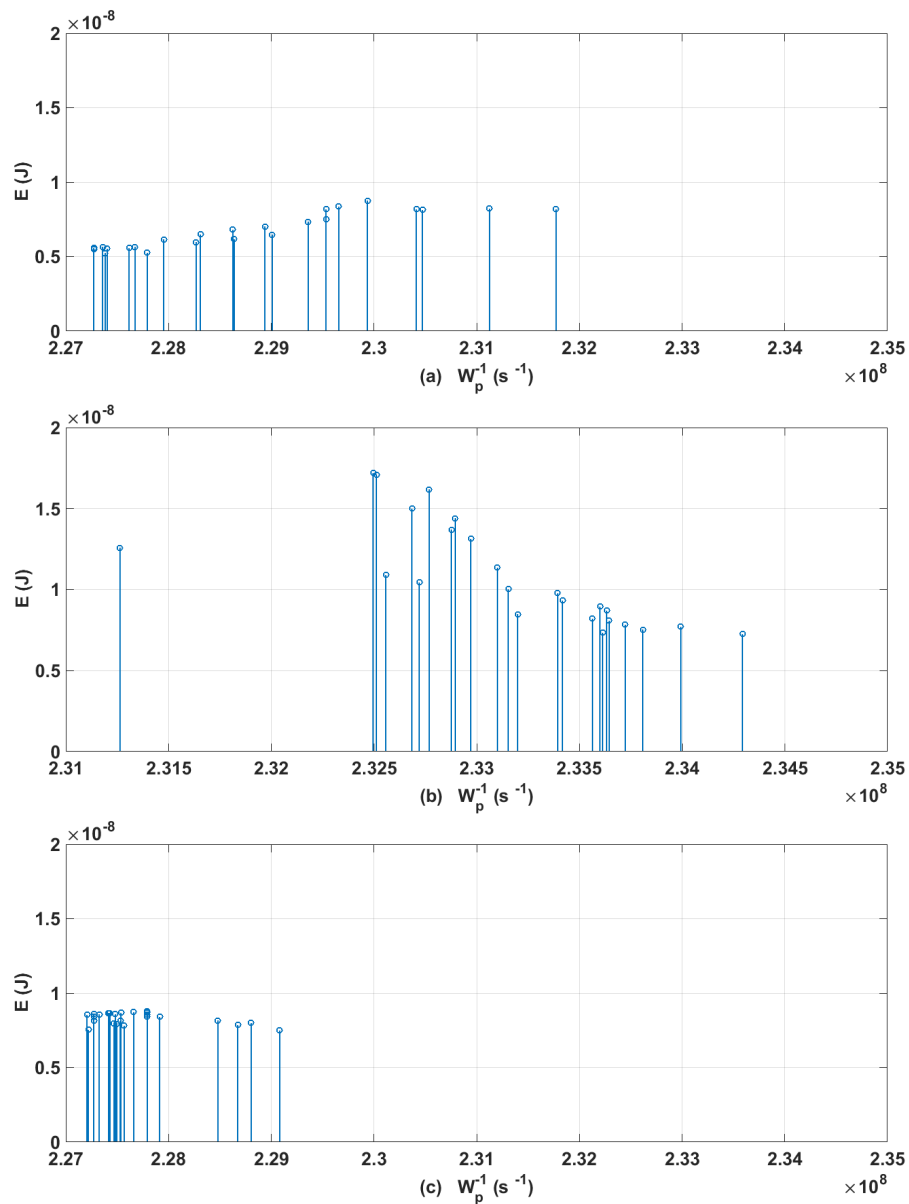


Figure 5.15: Short pulses obtained for (a) a linear chirp, (b) a hyperbolic chirp and (c) a mean chirp, for $B_0=12.5$ MHz - 142.5 MHz.

22.5 MHz as it gives the maximum value of A_p for a short pulse of ≈ 10 ns duration.

5.2.2.1/ Optimization of a Short pulse

In order to improve the pulse compression system, several techniques have been employed in the past. One of which is the use of the two parameter Pareto model [92–94]. In most design or optimization situations, a bound is placed on one of the criteria and the other is optimized within this bound. If the pulse width is fixed the total energy of the signal can be redistributed such that it produces a pulse with a higher amplitude. In our case, an optimal input signal $H(\omega)_I$ can be found to obtain the optimum performance of the fabricated SAW devices by finding a trade-off between the pulse width and the pulse amplitude.

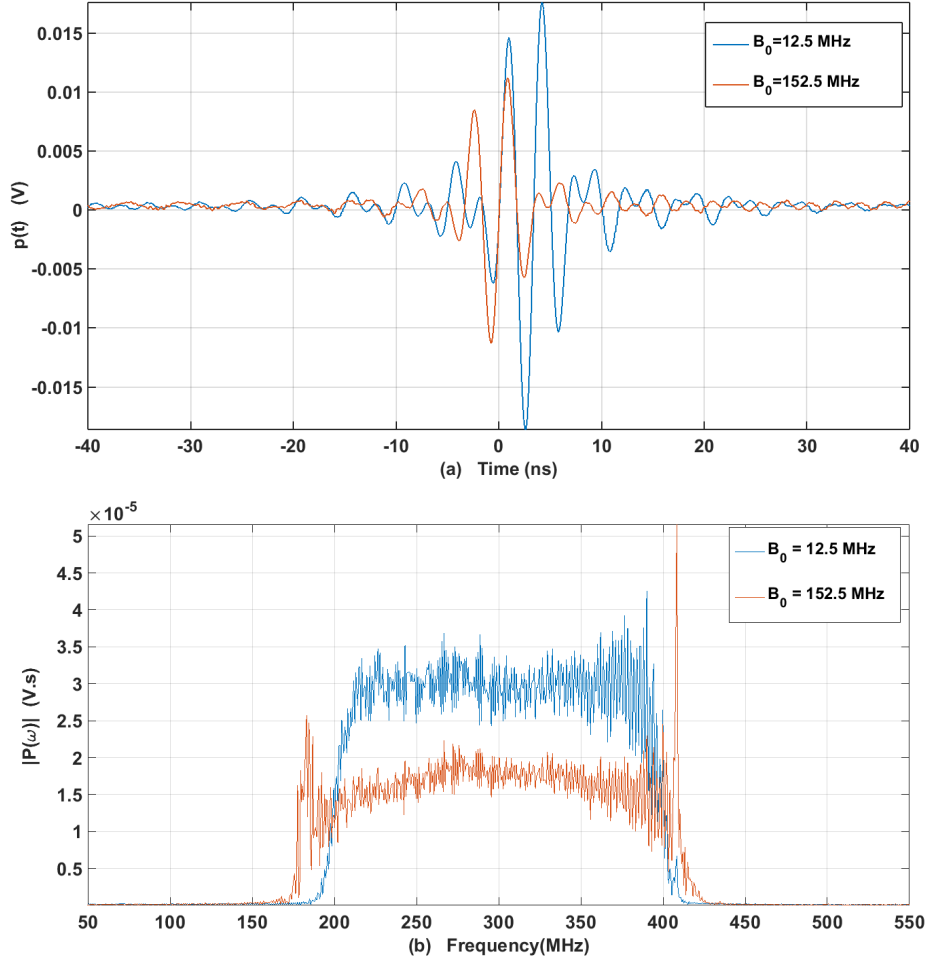


Figure 5.16: (a) Short pulses obtained for a hyperbolic chirp for $B_0 = 12.5$ MHz, 152.5 MHz and (b) The pulse amplitude $|P(\omega)|$ shown in the frequency domain.

A simple attempt is made to optimize the short pulse without implementation of complex optimization modules [92,93]. A design parameter of the inverse chirp filter is found such that it is sensitive to both, the amplitude and the pulse width of the short pulse, and affects both when varied. In our case we have chosen B_0 .

$$E = \frac{1}{Z_0} \int_{T_1}^{T_2} |p(t)|^2 dt \quad (5.11)$$

The total energy E of the pulse $p(t)$ is calculated using equation 5.11, where Z_0 is the impedance $\approx 50\Omega$, when $G(t)$ is in Volts (V). Figure 5.15 shows a plot of the optimal curve with the two interdependent quantities being, the maximum E of the pulse, and the inverse of the FWHM of the pulse (W_p^{-1}), for the SAW devices with the three different CIDTs, as the B_0 parameter for the inverse chirp filter design is varied. In case of a linear chirp as seen in Figure 5.15 (a), the curve varies such that, as the B_0 parameter increases, the pulse amplitude decreases with the decrease in the pulse width as well. This is because a variation in B_0 allows the window for the inverse chirp to be modified such that the bandwidth increases, causing the pulse width to reduce. The variation in E with respect to W_p^{-1} is irregular. However, for the maximum value of $E = 0.87 \times 10^{-8}$ J, W_p^{-1} is ≈ 2.3 s $^{-1}$ corresponding to a FWHM pulse

width of ≈ 5 ns, which in turn corresponds to a full pulse width of 10 ns. The pulse width for this particular chirp is not very sensitive to a variation in B_0 hence the curve is fairly flat.

In case of the SAW device with a hyperbolic CIDT, as seen in Figure 5.15 (b), a different trend is observed. The energy is much higher compared to the linear chirp case as seen in Figure 5.15 (a). E obtained for a pulse width of ≈ 10 ns, is 1.71×10^{-8} J, and W_p^{-1} is $\approx 2.325 \times 10^8$ s $^{-1}$. For this case the curve obtained varies exponentially. It is observed that a small gain in pulse width reduction leads to a loss in amplitude A_p . Both parameters, the amplitude A_p , and the pulse width show greater sensitivity to a variation in B_0 for this chirp type.

In case of the SAW device with a mean CIDT, as seen in Figure 5.15 (c), it is observed that the progression of the curve for a variation in the B_0 parameter is irregular for several values. Since the transmission measurements obtained for this device are noisy, the inverse filter responses generated for this case were also noisy. The value of A_p is lower compared to both, the linear chirp case as seen in Figure 5.15 (a), and the hyperbolic chirp case, as seen in Figure 5.15 (b). A_m obtained for a pulse width of ≈ 10 ns, is $\approx 0.87 \times 10^{-8}$ V 2 . For the given B_0 range the variation in W_p^{-1} is much smaller compared to the previous cases.

Figure 5.16 (a) shows two short pulses for the hyperbolic case, measured for the $B_0 = 12.5$ MHz and 152.2 MHz. When B_0 is increased to 152.2 MHz a short pulse is obtained with a full pulse width of ≈ 8 ns. It is observed that for $B_0 = 152.5$ MHz, even though we are able to achieve a shorter pulse due to an increase in the bandwidth by ≈ 25 MHz, as seen in Figure 5.16 (b), the amplitude A_p , of the pulse is much lower. This shows that as we gain in pulse width reduction, we lose in amplitude A_p , of the pulse.

5.3/ Conclusion

In this chapter, a comparison between three different filter designs, used to obtain the input chirp to be sent to the respective CIDTs using an arbitrary waveform generator, to produce a short pulse with $W_p = 5$ ns, is presented. The short pulses obtained using filter 1 and filter 3 are compared, and the pulse for the hyperbolic chirp case, for both types, is found to have the maximum amplitude A_p . Filter 2, that produces the inverse chirp, is found to be most effective as it produces a short pulse with the highest amplitude A_p , compared to the other two filter designs for the same pulse width, for all three chirp cases. Filter 2 is used to generate inverse chirps for the fabricated SAW devices. On comparison, the short pulse obtained for the hyperbolic case is found to have the highest amplitude A_p .

The B_0 parameter for tuning the window used to design the inverse chirps, is varied to find an optimal value of the short pulse such that, the SAW devices produce a short pulse with the highest amplitude A_p . The best optimal curve is obtained for the hyperbolic case. A variation in the pulse width W_p is observed for the SAW device with a hyperbolic chirp and the shortest pulse obtained is ≈ 8 ns, for a B_0 value of 152.5 MHz as seen in figure 5.16, however the amplitude $|P(t)|$ is much lower compared to that of the 10 ns pulse. No reduction in pulse width is observed for the linear and mean chirp SAW devices. Variation in the B_0 allows us to fine tune the inverse chirps, however, it is not a very effective technique to optimize the short pulse for the other two chirp cases.



CONCLUSION

Conclusion and future work

The main objective of this thesis was to conduct a preliminary study of the generation and propagation of short pulses with surface acoustic waves (SAW) and implement the chirped pulse technique (CPA) to produce shorter pulses with a high amplitude. Temporal compression of pulses has been achieved with SAW devices consisting chirped IDTs with a bandwidth of 200 MHz-400 MHz, as the dispersive element.

In this work, we have studied chirped inter-digital transducers (CIDTs) and presented a comparison between the simulation results obtained using the first order model, and the MatMixLib software that employs the p-matrix model. The design parameters for the respective CIDTs have also been described. Using the design parameters for the p-matrix simulations, SAW devices have been fabricated with different CIDTs and a detailed description of the fabrication process has been presented. The design of a reference sample with a linear frequency modulation and apodisation, used for comparative study with the fabricated devices, has been described. When the responses of the respective fabricated SAW devices are compared to the simulation results, the SAW device with the hyperbolically chirped input IDT that is equivalent to an IDT with linear frequency modulation (LFM), is found to have the best response among the three in terms of power of the signal.

We have then investigated the appearance of band gaps within the CIDTs and have demonstrated their effect on the directivity due to the variation in the CIDT design parameters. When the number of electrodes N , increases, it is observed that the band gaps formed due to strong internal reflections at the Bragg frequency become more efficient and cause the CIDTs, that are expected to be bidirectional by design and have waves exiting it on both sides with equal amplitude, to have a response stronger in one direction compared to the other. Also, when the number of electrodes increases, there is an overall increase in the total power of the response, as expected. As the height of the metal thickness of the electrodes h is increased, it is observed that the directionality is reversed beyond a particular value of h since the reflection coefficient changes sign. It is the same for the three chirp types.

In the next part of the thesis we have described a differential optical interferometer that is capable of time domain shearing and provides short pulse measurement of surface acoustic waves. The interferometer is an extended version of a Michelson interferometer implementing time-shearing. It is stabilized against low frequency noise using a PID controller actively maintaining the path length difference at a single quadrature point. Apart from high accuracy, one major advantage of using an interferometer as a measurement tool for studying SAW propagation within the device is that it allows us to measure the ultrasonic vibration by varying the position of the laser beam anywhere within the device. Short SAW pulses with a duration of 10 ns produced by an ultra-wide bandwidth chirped SAW transducer were measured and

compared with an equivalent electrical measurement and with theory. Good agreement was found and the overall waveform was well conserved. Maximum displacements of about 36 nm were observed, with a detection limit of 40 pm. Pulse compression along the chirped SAW transducer was furthermore observed experimentally.

In order to achieve a good pulse optimization, the energy distribution within the signal is required to be modulated for each frequency component. In radar systems, an optimum performance can be achieved by a trade-off between the range resolution that depends on the bandwidth of the signal, and long range detection that depends on the amplitude of the pulse, for a given pulse length. Several matched and mismatched filters have been proposed to improve pulse compression [93]. In the next part of this thesis we have compared three filter designs to generate short pulses. The inverse filter is found to be the most efficient as it produces a short pulse with the maximum amplitude. The SAW device with the hyperbolic CIDT is found to have the best response as it produces a short pulse with the maximum amplitude. We did not obtain a gain in pulse compression in terms of reduction in pulse width, however, we did optimize the pulse in terms of amplitude.

There are several distributions used for signal optimization in radar systems, like Weibull, Log-Normal and K-Distributions. The Pareto optimization is an effective and a much simpler approach as it is a two parameter model unlike the other distributions. Several models based on this have been proposed to improve the signal-to-noise ratio of filter responses by finding a trade-off between the Integrated Side lobes and the peak side lobes of a signal. Implementation of models based on Pareto optimal trade-off curves would be the next step to improve the optimization. In our case, one method could be to design a filter generating the input chirp such that by modulating a weighting parameter of the filter design, that effects both, the pulse width and the amplitude of the short pulse equally, an optimal trade-off curve can be obtained.

In the future, it would be interesting to study the effects of the band gaps within the CIDTs for higher frequency ranges and larger bandwidths, and their effect on the short pulse generated. If we increase the number of electrodes, we can generate a high amplitude short pulse but that leads to a fabrication of a longer SAW device, which may not be preferable for several applications. However, unlike for other cuts of LiNbO_3 , the reflection coefficient for LiNbO_3 YX 128° , changes sign for a certain value of electrode thickness which causes a change in directionality of the CIDTs and the band gap effect due to internal reflection in the CIDTs is stronger, thus the amplitude of the exiting wave is much larger for certain values of electrode thickness. This phenomenon can be used to design SAW devices that produce high amplitude short pulses, without compromising on the size of the device. The interferometer described in this work is a two-wave interferometer capable of time domain measurements. An acousto-optic modulator(AOM) can also be added along one of the reference arms to the existing setup to add a frequency shift, chosen carefully to avoid mixing of signals since for a wide bandwidth, it could be a problem to separate the side bands from the main one. This would allow measurements of the amplitude of the surface vibration. Multiple-wave interferometers like the Fabry-Perot interferometer could also be used to investigate short pulses for future work. On a broader perspective, this work can be considered as a preliminary step towards several prospective applications like investigation of surface wave coupling in acoustic waveguides, soliton generation and excitation of bubbles under water in micro devices.

Bibliography

- [1] Y. Sugawara, O. B. Wright, O. Matsuda, M. Takigahira, Y. Tanaka, S. Tamura, and V. E. Gusev. Watching ripples on crystals. *Phys. Rev. Lett.*, 88(18):185504, 2002.
- [2] SJ Davies, Chris Edwards, GS Taylor, and Stuart B Palmer. Laser-generated ultrasound: its properties, mechanisms and multifarious applications. *J. Phys. D: Appl. Phys.*, 26(3):329, 1993.
- [3] Donna Strickland and Gerard Mourou. Compression of amplified chirped optical pulses. *Opt. Commun.*, 56(3):219–221, 1985.
- [4] George S Kliros and Elias K Pilakoutas. Stretching of short pulses through transmission in non-linear photonic crystal fibers. In *Telecommunications Forum Telfor (TELFOR), 2014 22nd*, pages 613–616. IEEE, 2014.
- [5] R. L. Fork, O.E. Martinez, and J.P. Gordon. Negative dispersion using pairs of prisms. *Opt. Lett.*, 9(5):150–152, 1984.
- [6] François Salin, Jeff Squier, and Gérard Mourou. Large temporal stretching of ultrashort pulses. *Appl. Opt.*, 31(9):1225–1228, 1992.
- [7] Vincent Laude, Davy Gérard, Naima Khelifaoui, Carlos F Jerez-Hanckes, Sarah Benchabane, and Abdelkrim Khelif. Subwavelength focusing of surface acoustic waves generated by an annular interdigital transducer. *Applied Physics Letters*, 92(9):094104, 2008.
- [8] J-P Monchalain. Optical detection of ultrasound. *IEEE Trans. Ultrason., Ferroelec., Freq. Control*, 33:485–499, 1986.
- [9] Kimmo Kokkonen et al. *Imaging of Surface Vibrations Using Heterodyne Interferometry*. PhD thesis, Aalto University, 2014.
- [10] Chien-Ming Wu and Richard D Deslattes. Analytical modeling of the periodic nonlinearity in heterodyne interferometry. *Appl. Opt.*, 37(28):6696–6700, 1998.
- [11] Kimmo Kokkonen and Matti Kaivola. Scanning heterodyne laser interferometer for phase-sensitive absolute-amplitude measurements of surface vibrations. *Applied Physics Letters*, 92(6):063502, 2008.
- [12] Richard O Claus and Tyson M Turner. Dual differential interferometer, 1985. US Patent 4,512,661.
- [13] H-N Lin, RJ Stoner, HJ Maris, and J Tauc. Phonon attenuation and velocity measurements in transparent materials by picosecond acoustic interferometry. *J. Appl. Phys.*, 69(7):3816–3822, 1991.
- [14] X Jia, Ch Matteï, and G Quentin. Analysis of optical interferometric measurements of guided acoustic waves in transparent solid media. *J. Appl. Phys.*, 77(11):5528–5537, 1995.

- [15] P-A Mante, A Devos, and A Le Louarn. Generation of terahertz acoustic waves in semiconductor quantum dots using femtosecond laser pulses. *Phys. Rev. B*, 81(11):113305, 2010.
- [16] Jouni V Knuuttila, Pasi T. Tikka, and Martti M Salomaa. Scanning Michelson interferometer for imaging surface acoustic wave fields. *Opt. Lett.*, 25(9):613–615, 2000.
- [17] Meindert A. van Dijk, Markus Lippitz, and Michel Orrit. Detection of acoustic oscillations of single gold nanospheres by time-resolved interferometry. *Phys. Rev. Lett.*, 95(26):267406, 2005.
- [18] MG Cain, M Stewart, and M Downs. Characterisation of thin film piezoelectric materials by differential interferometric techniques. *NSTI-Nanotech 2006*, 2, 2006.
- [19] M Çelik, E Şahin, T Yandayan, R Hamid, A Akgöz, B Özgür, M Çetintaş, and A Demir. Application of the differential Fabry–Perot interferometer in angle metrology. *Measurement Science and Technology*, 27(3):035201, 2016.
- [20] C Harvey Palmer and Robert E Green Jr. Optical probing of acoustic emission waves. In *Nondestructive evaluation of materials*, pages 347–378. Springer, 1979.
- [21] JD Aussel, A Le Brun, and JC Baboux. Generating acoustic waves by laser: theoretical and experimental study of the emission source. *Ultrason.*, 26(5):245–255, 1988.
- [22] J-P Monchalin, R Heon, and N Muzak. Evaluation of ultrasonic inspection procedures by field mapping with an optical probe. *Canadian Metallurgical Quarterly*, 2013.
- [23] Evert Jan Post. Sagnac effect. *Reviews of Modern Physics*, 39(2):475, 1967.
- [24] Tobias Eberle, Sebastian Steinlechner, Jöran Bauchrowitz, Vitus Händchen, Henning Vahlbruch, Moritz Mehmet, Helge Müller-Ebhardt, and Roman Schnabel. Quantum enhancement of the zero-area Sagnac interferometer topology for gravitational wave detection. *Physical review letters*, 104(25):251102, 2010.
- [25] Peter T Beyersdorf, MM Fejer, and RL Byer. Polarization Sagnac interferometer with postmodulation for gravitational-wave detection. *Opt. Lett.*, 24(16):1112–1114, 1999.
- [26] R. Anderson, H. R. Bilger, and G. E. Stedman. "Sagnac" effect: A century of Earth-rotated interferometers. *American Journal of Physics*, 62:975–985, November 1994.
- [27] Ken-Ya Hashimoto, Keiskue Kashiwa, Nan Wu, Tatsuya Omori, Masatsune Yamaguchi, Osamu Takano, Sakae Meguro, and Koichi Akahane. A laser probe based on a Sagnac interferometer with fast mechanical scan for RF surface and bulk acoustic wave devices. *IEEE Trans. Ultrason., Ferroelec., Freq. Control*, 58(1):187–194, 2011.
- [28] Y Sugawara, OB Wright, and O Matsuda. Real-time imaging of surface acoustic waves in thin films and microstructures on opaque substrates. *Review of scientific instruments*, 74(1):519–522, 2003.
- [29] YI Sugawara, OB Wright, O Matsuda, M Takigahira, YI Tanaka, S Tamura, and VE Gusev. Watching ripples on crystals. *Phys. Rev. Lett.*, 88(18):185504, 2002.
- [30] Lord Rayleigh. On waves propagated along the plane surface of an elastic solid. *Proceedings of the London Mathematical Society*, 1(1):4–11, 1885.

- [31] DR Morgan. Surface acoustic wave devices and applications: 1. Introductory review. *Ultrasonics*, 11(3):121–131, 1973.
- [32] Zhangliang Xu and Yong J Yuan. Implementation of guiding layers of surface acoustic wave devices: A review. *Biosensors and Bioelectronics*, 99:500–512, 2018.
- [33] Thierry Aubert, Omar Elmazria, Badreddine Assouar, Laurent Bouvot, Michel Hehn, Sylvain Weber, Mourad Oudich, and Damien Genève. Behavior of platinum/tantalum as interdigital transducers for SAW devices in high-temperature environments. *IEEE Trans. Ultrason., Ferroelec., Freq. Control*, 58(3), 2011.
- [34] Thierry Aubert, Omar Elmazria, Badreddine Assouar, Eloi Blampain, Ahmad Hamdan, Damien Genève, and Sylvain Weber. Investigations on AlN/sapphire piezoelectric bilayer structure for high-temperature SAW applications. *IEEE Trans. Ultrason., Ferroelec., Freq. Control*, 59(5):999–1005, 2012.
- [35] Abdelkrim Talbi, Frederic Sarry, Laurent Le Brizoual, Omar Elmazria, and Patrick Alnot. Sezawa mode SAW pressure sensors based on ZnO/Si structure. *IEEE Trans. Ultrason., Ferroelec., Freq. Control*, 51(11):1421–1426, 2004.
- [36] Thierry Aubert, MB Assouar, Ouarda Legrani, Omar Elmazria, Coriolan Tiusan, and Sylvie Robert. Highly textured growth of AlN films on sapphire by magnetron sputtering for high temperature surface acoustic wave applications. *Journal of Vacuum Science & Technology A: Vacuum, Surfaces, and Films*, 29(2):021010, 2011.
- [37] Matteo Agostini, Gina Greco, and Marco Cecchini. A Rayleigh surface acoustic wave (r-SAW) resonator biosensor based on positive and negative reflectors with sub-nanomolar limit of detection. *Sensors and Actuators B: Chemical*, 254:1–7, 2018.
- [38] Matthias Weiß, Andreas L Hörner, Eugenio Zallo, Paola Atkinson, Armando Rastelli, Oliver G Schmidt, Achim Wixforth, and Hubert J Krenner. Multiharmonic Frequency-Chirped Transducers for Surface-Acoustic-Wave Optomechanics. *Physical Review Applied*, 9(1):014004, 2018.
- [39] Thierry Aubert, Omar Elmazria, Badreddine Assouar, Laurent Bouvot, and Mourad Oudich. Surface acoustic wave devices based on AlN/sapphire structure for high temperature applications. *Applied Physics Letters*, 96(20):203503, 2010.
- [40] Julien Deboucq, Marc Duquennoy, Mohammadi Ouafrouh, Frédéric Jenot, Julien Carlier, and Mohamed Ourak. Development of interdigital transducer sensors for non-destructive characterization of thin films using high frequency Rayleigh waves. *Review of Scientific Instruments*, 82(6):064905, 2011.
- [41] Yancheng Wang, Dai Xue, and Deqing Mei. Patterned microstructure array fabrication by using a novel standing surface acoustic wave device. *Journal of Micro and Nano-Manufacturing*, 6(2):021002, 2018.
- [42] Thierry Aubert, Jochen Bardong, Ouarda Legrani, Omar Elmazria, M Badreddine Assouar, Gudrun Bruckner, and Abdelkrim Talbi. In situ high-temperature characterization of AlN-based surface acoustic wave devices. *J. Appl. Phys.*, 114(1):014505, 2013.
- [43] Philippe Kirsch, Mohamed B Assouar, Omar Elmazria, M El Hakiki, Vincent Mortet, and Patrick Alnot. Combination of e-beam lithography and of high velocity AlN/diamond-layered structure for SAW filters in X band. *IEEE Trans. Ultrason., Ferroelec., Freq. Control*, 54(7), 2007.

- [44] B Vincent, Jan-Kristian Krüger, Omar Elmazria, L Bouvot, Julia Mainka, Roland Sanctuary, Didier Rouxel, and Patrick Alnot. Imaging of microwave-induced acoustic fields in LiNbO₃ by high-performance Brillouin microscopy. *Journal of Physics D: Applied Physics*, 38(12):2026, 2005.
- [45] Kanwar J Singh, Omar Elmazria, Frederic Sarry, Pascal Nicolay, Kamal Ghoumid, Brahim Belgacem, Denis Mercier, and Julien Bounouar. Enhanced sensitivity of SAW-based pirani vacuum pressure sensor. *IEEE Sensors Journal*, 11(6):1458–1464, 2011.
- [46] Omar Elmazria and Thierry Aubert. Wireless SAW sensor for high temperature applications: Material point of view. In *Smart Sensors, Actuators, and MEMS V*, volume 8066, page 806602. International Society for Optics and Photonics, 2011.
- [47] Dame Fall, Marc Duquennoy, Mohammadi Ouaftouh, Bogdan Piwakowski, and Frederic Jenot. Effective and rapid technique for temporal response modeling of surface acoustic wave interdigital transducers. *Ultrasonics*, 82:371–378, 2018.
- [48] Hiroaki Sakamoto, Hiroki Kitanishi, Satoshi Amaya, Tsunemasa Saiki, Yuichi Utsumi, and Shin-ichiro Suye. Development of a high-sensitive electrochemical detector with micro-stirrer driven by surface acoustic waves. *Sensors and Actuators B: Chemical*, 2018.
- [49] Chunbae Lim, Wen Wang, Sangsik Yang, and Keekeun Lee. Development of SAW-based multi-gas sensor for simultaneous detection of CO₂ and NO₂. *Sensors and Actuators B: Chemical*, 154(1):9–16, 2011.
- [50] Pierre Barbo. *Pierre Curie (1859-1906): pour une biographie intellectuelle*. Belin, 1999.
- [51] Gabriel Lippmann. Principe de la conservation de l'électricité, ou second principe de la théorie des phénomènes électriques. *Journal de Physique Théorique et Appliquée*, 10(1):381–394, 1881.
- [52] Guojun Wang. *Piezoelectric energy harvesting utilizing human locomotion*. PhD thesis, University of Minnesota, 2010.
- [53] Vincent Laude. Ondes élastiques guidées. <http://members.femto-st.fr/sites/femto-st.fr.vincent-laude/files/content/spim/og2.pdf>, 2016. Accessed: 2017-09-30.
- [54] Colin Campbell. *Surface acoustic wave devices and their signal processing applications*. Elsevier, 2012.
- [55] D. P. Morgan. *Surface-wave devices for signal processing*. Elsevier, 1985.
- [56] Daniel Royer and Eugene Dieulesaint. *Elastic waves in solids II: generation, acousto-optic interaction, applications*. Springer Science & Business Media, 1999.
- [57] RM White and FW Voltmer. Direct piezoelectric coupling to surface elastic waves. *Appl. Phys. Lett.*, 7(12):314–316, 1965.
- [58] Clinton S Hartmann, Delamar T Bell, and Ronald C Rosenfeld. Impulse model design of acoustic surface-wave filters. *IEEE Transactions on Microwave Theory and Techniques*, 21(4):162–175, 1973.
- [59] W Richard Smith, Henry M Gerard, Jeffrey H Collins, Thomas M Reeder, and Herbert J Shaw. Analysis of interdigital surface wave transducers by use of an equivalent circuit model. *IEEE Transactions on Microwave Theory and Techniques*, 17(11):856–864, 1969.

- [60] WC Wilson and GM Atkinson. *A Comparison of Surface Acoustic Wave Modeling Methods*, chapter 5. Nano Science and Technology Institute, 2009.
- [61] Ken-ya Hashimoto and Ken-Ya Hashimoto. *Surface acoustic wave devices in telecommunications*. Springer, 2000.
- [62] PV Wright. A new generalized modeling of SAW transducers and gratings. In *Frequency Control, 1989., Proceedings of the 43rd Annual Symposium on*, pages 596–605. IEEE, 1989.
- [63] BP Abbott, CS Hartmann, and DC Malocha. A coupling-of-modes analysis of chirped transducers containing reflective electrode geometries. In *Ultrasonics Symposium, 1989. Proceedings., IEEE 1989*, pages 129–134. IEEE, 1989.
- [64] CS Hartmann and BP Abbott. Overview of design challenges for single phase unidirectional SAW filters. In *Ultrasonics Symposium, 1989. Proceedings., IEEE 1989*, pages 79–89. IEEE, 1989.
- [65] Ali-Reza Baghai-Wadji, Siegfried Selberherr, and Franz J Seifert. *On the calculation of charge, electrostatic potential and capacitance in generalized finite SAW structures*. na, 1984.
- [66] Bernd Fleischmann and Halvor Skeie. Higher harmonic surface transverse wave filters. In *Ultrasonics Symposium, 1989. Proceedings., IEEE 1989*, pages 235–239. IEEE, 1989.
- [67] KC Wagner and O Manner. A fast green's function method for calculating bulk wave frequency responses from SAW frequency responses. In *Ultrasonics Symposium, 1990. Proceedings., IEEE 1990*, pages 411–415. IEEE, 1990.
- [68] LA Coldren and RL Rosenberg. Scattering matrix approach to SAW resonators. In *1976 Ultrasonics Symposium*, pages 266–271. IEEE, 1976.
- [69] R. Lardat. Pertes Ohmiques et Matrice Mixte, 2001. Internal report, Thales Microsonics.
- [70] C. De Sena. Simulation de dispositifs à ondes électro-acoustiques de surface par la méthode de la matrice mixte, 2001. Internal report, Thales Microsonics.
- [71] JM Hodé, J Desbois, P Difilie, M Solal, and P Ventura. SPUDT-based filters: Design principles and optimization. In *Ultrasonics Symposium, 1995. Proceedings., 1995 IEEE*, volume 1, pages 39–50. IEEE, 1995.
- [72] Yan Fusero. *Etude théorique et expérimentale de dispositifs à ondes de surface à haute vitesse et fort couplage : application aux filtres télécom haute fréquence*. PhD thesis, Université de Franche-Comté, 2001.
- [73] Marvin N Cohen. Pulse compression in radar systems. *Principles of Modern Radar*, pages 465–501, 1987.
- [74] Marc Lamothe. *Capteurs à ondes élastiques de surface à codage spectral Ultra Large Bande*. PhD thesis, Besançon, 2014.
- [75] K Kitamura, JK Yamamoto, N Iyi, S Kirnura, and T Hayashi. Stoichiometric LiNbO₃ single crystal growth by double crucible Czochralski method using automatic powder supply system. *Journal of crystal growth*, 116(3-4):327–332, 1992.

- [76] S Seckin Senlik, Askin Kocabas, and Atilla Aydinli. Grating based plasmonic band gap cavities. *Opt. Express*, 17(18):15541–15549, 2009.
- [77] Th Pastureauud. Evaluation of the P-matrix parameters frequency variation using periodic FEM/BEM analysis [SAW device simulation]. In *Ultrasonics Symposium, 2004 IEEE*, volume 1, pages 80–84. IEEE, 2004.
- [78] David Morgan. *Surface acoustic wave filters: With applications to electronic communications and signal processing*. Academic Press, 2010.
- [79] Anurupa Shaw, Damien Teyssieux, and Vincent Laude. A differential optical interferometer for measuring short pulses of surface acoustic waves. *Ultrasonics*, 80:72–77, 2017.
- [80] Clinton S Hartmann. Weighting interdigital surface wave transducers by selective withdrawal of electrodes. In *1973 Ultrasonics Symposium*, pages 423–426. IEEE, 1973.
- [81] AJ Slobodnik, KR Laker, TL Szabo, WJ Kearns, and GA Roberts. Low sidelobe SAW filters using overlap and withdrawal weighted transducers. In *Ultrasonics Symposium, 1977*, pages 757–762. IEEE, 1977.
- [82] JE Graebner, BP Barber, PL Gammel, DS Greywall, and S Gopani. Dynamic visualization of subangstrom high-frequency surface vibrations. *Appl. Phys. Lett.*, 78(2):159–161, 2001.
- [83] Lauri Lipiäinen, Kimmo Kokkonen, and Matti Kaivola. Phase sensitive absolute amplitude detection of surface vibrations using homodyne interferometry without active stabilization. *J. Appl. Phys.*, 108(11):114510, 2010.
- [84] D. Royer and O. Casula. A sensitive ultrasonics method for measuring transient motions of a surface. *Appl. Phys. Lett.*, 67:3248–3250, 1995.
- [85] Pascal Vairac and Bernard Cretin. New structures for heterodyne interferometric probes using double-pass. *Opt. Commun.*, 132(1-2):19 – 23, 1996.
- [86] Hanne Martinussen, Astrid Aksnes, and Helge E Engan. Wide frequency range measurements of absolute phase and amplitude of vibrations in micro- and nanostructures by optical interferometry. *Opt. Express*, 15(18):11370–11384, 2007.
- [87] K. Kokkonen, M. Kaivola, S. Benchabane, A. Khelif, and V. Laude. Scattering of surface acoustic waves by a phononic crystal revealed by heterodyne interferometry. *Appl. Phys. Lett.*, 91:083517, 2007.
- [88] Kimmo Kokkonen and Matti Kaivola. Scanning heterodyne laser interferometer for phase-sensitive absolute-amplitude measurements of surface vibrations. *Appl. Phys. Lett.*, 92(6):063502, 2008.
- [89] David H Hurley and Oliver B Wright. Detection of ultrafast phenomena by use of a modified Sagnac interferometer. *Opt. Lett.*, 24(18):1305–1307, 1999.
- [90] Takehiro Tachizaki, Toshihiro Muroya, Osamu Matsuda, Yoshihiro Sugawara, David H Hurley, and Oliver B Wright. Scanning ultrafast Sagnac interferometry for imaging two-dimensional surface wave propagation. *Rev. Sci. Instrum.*, 77(4):043713, 2006.
- [91] Rémi Marchal. *Métamatériaux acoustiques actifs*. PhD thesis, Paris 6, 2014.

- [92] Matthew Fellows, Charles Baylis, Lawrence Cohen, and Robert J Marks II. Real-time load impedance optimization for radar spectral mask compliance and power efficiency. *IEEE Transactions on Aerospace and Electronic Systems*, 51(1):591–599, 2015.
- [93] Vikas Baghel, Ganapati Panda, P Srihari, K Rajarajeswari, and Babita Majhi. An efficient multi-objective pulse radar compression technique using RBF and NSGA-II. In *Nature & Biologically Inspired Computing, 2009. NaBIC 2009. World Congress on*, pages 1291–1296. IEEE, 2009.
- [94] Merrill I Skolnik. Introduction to radar. *Radar Handbook*, 2, 1962.

List of Figures

1.1	A Schematic illustration of the chirped pulse amplification technique.	4
2.1	Schematic of a homodyne Michelson interferometer	6
2.2	Schematic of a heterodyne interferometer	7
2.3	A Schematic of a differential interferometer proposed by Palmer and green [20] .	9
2.4	Schematic of a Sagnac interferometer	11
2.5	Unit Cell of a piezoelectric material with the center ion in black, (a) when the material is not electrically or mechanically excited, and (b) when the material is either mechanically stressed to produce an electric field or is excited by an electric field and physically deformed [52].	12
2.6	A pictorial representation (not to scale) of SAW motion on the surface of an elastic solid. Although the illustration relates to a piezoelectric solid, this is not a requirement for SAW propagation [54].	14
2.7	A schematic of a basic saw device [55].	15
2.8	A schematic showing voltage applied across the two comb-shaped electrodes produces stresses near the solid surface [56].	15
2.9	A Schematic of a surface acoustic wave device for generating a short pulse where p is the pitch of the IDT and a is the acoustic aperture.	16
2.10	A schematic of SAW devices with (a) a linear up-chirp CIDT and (b)a linear down-chirp CIDT [54]	17
2.11	A schematic of a first order model of an IDT in which the IDT is modelled by an array of discrete sources at the centres of interdigital intervals, with amplitudes proportional to the finger overlap w [56].	18
2.12	A Schematic representation of a single period transducer with the acoustic and electric ports.	22
2.13	Plots showing a variation in (a) the SAW velocity, (b) $ \Delta $ and (c) the directivity ($^\circ$), for a variation in $\frac{h}{\lambda}$ (%), for LiNbO ₃ with cut(YXI) 128 $^\circ$	25
2.14	Plots showing a variation in (a) the SAW velocity, (b) $ \Delta $ and (c) directivity ($^\circ$), for a variation in $\frac{h}{\lambda}$ (%), for LiNbO ₃ with cut(YZ).	26
2.15	Measurement of the transmitted signal of the reference SAW device [74] using a network analyser.	26
3.1	Modulus of the spectral amplitude (in arbitrary units) for (a) a linear chirp, (b) a hyperbolic chirp and (c) a mean chirp, obtained using a delta function model.	35

3.2	Waveforms (amplitude in arbitrary units) obtained for a (a) a linear chirp, (b) a hyperbolic chirp and (c) a mean chirp, obtained using a delta function model.	35
3.3	Group delay of the CIDT response obtained for a (a) a linear chirp, (b) a hyperbolic chirp and (c) a mean chirp, obtained using a delta function model.	35
3.4	Modulus of the spectral amplitude for (a) a linear chirp, (b) a hyperbolic chirp and (c) a mean chirp, obtained using a p-matrix model.	37
3.5	Waveforms obtained for (a) a linear chirp, (b) a hyperbolic chirp and (c) a mean chirp, using a p-matrix model.	37
3.6	Group delay obtained for (a) a linear chirp, (b) a hyperbolic chirp and (c) a mean chirp, using a p-matrix model.	37
3.7	(a) S11 measurement (b) S21 measurement (c) admittance measurement and (d) group delay measurement of the reference sample	38
3.8	(a) S11 measurement (b) S21 measurement (c) admittance measurement and (d) group delay measurement of the reference sample with a metal plate.	38
3.9	A schematic of the lift-off process that is used for fabricating the SAW devices where layer (1) is the substrate (LiNbO_3), layer (2) is the photo resist and layer (3) is the metal (aluminium) deposited on the substrate. Steps of the lift-off process : (I) substrate prepared for lithography, (II) photoresist added on the substrate, (III) the SAW design deposited using photo-lithography with a negative mask, (IV) metal deposited by evaporation, and (V) lift-off completed by cleaning the resist and removing the unwanted metal deposited on the substrate.	40
3.10	SEM images showing the photoresist profile of the designed electrodes at the end of the lithography process.	41
3.11	SEM images of a linearly chirped input IDT showing (a) the minimum pitch, (b) the maximum pitch, and (c) a SEM image with the pitch measurement of the output IDT.	42
3.12	(a) An image of a fabricated SAW device with a hyperbolic chirp IDT after dicing and (b) a picture of the SAW device wire-bonded on a PCB.	43
3.13	(a) S11 measurement and (b) S21 measurement of the SAW device with a linearly chirped IDT fabricated using the specification mentioned in Table. 3.3. The chirp bandwidth is 200 MHz - 400 MHz.	43
3.14	(a) S11 measurement and (b) S21 measurement of the SAW device with a hyperbolically chirped IDT fabricated using the specification mentioned in Table. 3.3. The chirp bandwidth is 200 MHz - 400 MHz.	44
3.15	(a) S11 measurement and (b) S21 measurement of the SAW device with a mean chirped IDT fabricated using the specification mentioned in Table. 3.3. The chirp bandwidth is 200 MHz - 400 MHz.	44
3.16	A comparison between the (a) conductance and (b) susceptance of the SAW device responses with the three differently chirped IDTs, fabricated using the specification mentioned in Table. 3.3. The chirp bandwidth is 200 MHz - 400 MHz.	44

3.17	Admittance measurements for the transmission, obtained from the fabricated SAW devices with (a) a linear chirp, (b) a hyperbolic chirp and (c) a mean chirp. The chirp bandwidth is 200 MHz - 400 MHz.	45
3.18	Group delay measurements, obtained from the fabricated SAW devices with (a) a linear chirp, (b) a hyperbolic chirp and (c) a mean chirp. Chirp bandwidth is 200 MHz - 400 MHz.	45
3.19	Appearance of band gaps for a (a) single period IDT and (b) chirped IDT. (a) shows the dispersion relation of the Rayleigh wave in the periodic grating with the wavenumber k . (b) shows the variation of the band gap frequency range with the position within the CIDT.	46
3.20	The power response at each electrode within the IDT with 500 electrodes (el) for a pitch $p = 6.4 \mu\text{m}$ in (a) linear scale (b) log scale.	47
3.21	The power response at each electrode within the IDT with 1000 electrodes (el) for a pitch $p = 6.4 \mu\text{m}$ in (a) linear scale (b) log scale.	48
3.22	The power response at each electrode within the IDT with 2000 electrodes (el) for a pitch $p = 6.4 \mu\text{m}$ in (a) linear scale (b) log scale.	48
3.23	The power response at each electrode within the IDT with 3000 electrodes (el) for a pitch $p = 6.4 \mu\text{m}$ in (a) linear scale (b) log scale.	48
3.24	The power response at each electrode within the IDT with 5000 electrodes (el) for a pitch $p = 6.4 \mu\text{m}$ in (a) linear scale (b) log scale.	49
3.25	3D plots of the power response at each electrode within the CIDTs with 300 electrodes generating (a) linear (b) hyperbolic and (c) mean chirps respectively.	50
3.26	3D plots of the power response at each electrode within the CIDTs with 3000 electrodes generating (a) linear (b) hyperbolic and (c) mean chirps respectively.	51
3.27	Plots of the power response of the waves exiting on the left and the right of the down chirped IDT with 300 electrodes generating (a) linear (b) hyperbolic and (c) mean chirps respectively.	52
3.28	Plots of the power response of the waves exiting on the left and the right of the down chirped IDT with 3000 electrodes generating (a) linear (b) hyperbolic and (c) mean chirps respectively.	53
3.29	3D plots of the power response at each electrode within the up-chirped CIDTs with 300 electrodes, designed using the p-matrix model, corresponding the fabricated devices, generating (a) linear (b) hyperbolic and (c) mean chirps respectively.	54
3.30	3D plots of the power response at each electrode within the up-chirped CIDTs with 3000 electrodes, designed using the p-matrix model, corresponding the fabricated devices, generating (a) linear (b) hyperbolic and (c) mean chirps respectively.	55
3.31	Plots of the power response of the waves exiting on the left and the right of the up chirped IDT with 300 electrodes generating (a) linear (b) hyperbolic and (c) mean chirps respectively.	56

- 3.32 Plots of the power response of the waves exiting on the left and the right of the up chirped IDT with 3000 electrodes generating (a) linear (b) hyperbolic and (c) mean chirps respectively. 57
- 3.33 (a) Normalized signal response at the center of an down-chirped CIDT shown in figure 3.26 (a), simulated using the p-matrix model and (b) plot of the SAW device response measured using a differential interferometer [79], showing the existence of a band gap at around 350 MHz. 58
- 3.34 Plots of the power response of the waves exiting on both sides of the CIDTs with 300 electrodes generating a linear down-chirp for metallization height (a) $h= 50$ nm (b) $h= 200$ nm and (c) $h= 500$ nm. 59
- 3.35 A 3D plot of the power response at each electrode within the CIDTs with 300 electrodes generating a linear down-chirp for metallization height $h= 1000$ nm. 60
- 3.36 Plots of the power response of the waves exiting on both sides of the CIDTs with 300 electrodes generating a linear up-chirp for metallization height (a) $h= 50$ nm (b) $h= 200$ nm and (c) $h= 500$ nm. 61
- 3.37 A 3D plot of the power response at each electrode within the CIDTs with 300 electrodes generating a linear up-chirp for metallization height $h= 1000$ nm. . . 62
- 3.38 Plot showing a variation in (a) the reflection (%), i.e. $|\Delta|$, and (b) the directivity, as the $\frac{h}{\lambda}$ parameter changes. The metallization ratio used $\frac{a}{p} = 0.5$ 62
- 4.1 Schematic representation of three optical interferometers for the measurement of surface acoustic wave short pulses. (a) Michelson interferometer with the vibrating sample inside one arm of the interferometer. (b) Sagnac interferometer with the vibrating sample inside the loop. (c) Time-shearing, or time-delay, differential interferometer with the vibrating sample before the interferometer [79]. PBS: polarizing beam splitter, HWP: half wave plate, QWP: quarter wave plate, PID: proportional – integral – derivative controller. 66
- 4.2 (a) The beam profile of the elliptical beam at the exit of the laser. (b) The circular beam profile at the exit of the differential interferometer setup. 67
- 4.3 (a) Schematic of the short-pulse surface acoustic wave experiment. IDT: interdigital transducer. (b) Close view at the sample mounting. (c) Photograph of the differential interferometer setup with elements indicated following the schematic in Figure 4.1(c), [79]. 69
- 4.4 (a) Spectrum of the input chirp signal generated by the arbitrary waveform generator. (b) Theoretical shortest pulse, as obtained by Fourier transforming the spectrum of the input chirp signal assuming constant spectral phase. The full-width at half-maximum (FWHM) is 10 ns [79]. 71
- 4.5 (a) Electrical measurement and (b)interferometer measurement, at the location of the output interdigital transducer [79]. 72
- 4.6 (a) S12 measurement of the SAW device obtained using a network analyser and (b)A frequency domain representation of the electrical and interferometric measurements shown in Fig. 4.5 73

4.7	A plot showing the total voltage span of the interferometer obtained by varying the path difference between the beams along the two reference arms using a phased mirror.	74
4.8	Dependence of the pulse measurement with the time-delay Δt . (a) Plot of $\Delta u(x, t)$ at a given position as a function of Δt , for a 10-ns Gaussian pulse. (b) Experimental result as a function of Δt obtained by changing the path length difference in the interferometer [79].	76
4.9	Measurement of the SAW pulse at various positions along the chirped interdigital transducer [79].	77
5.1	$ H(\omega) $ for (a) a linear chirp, (b) a hyperbolic chirp and (c) a mean chirp, obtained using a p-matrix model.	79
5.2	Normalized waveforms obtained for (a) a linear chirp, (b) a hyperbolic chirp and (c) a mean chirp, by performing an inverse Fourier transform on the responses calculated using a p-matrix model as shown in figure 5.1.	80
5.3	Normalized input chirp waveforms obtained by performing an inverse Fourier transform on the response of filter 1 ($H(\omega)_{I1}$) for (a) a linear chirp, (b) a hyperbolic chirp and (c) a mean chirp, obtained using a p-matrix model.	81
5.4	(a) A plot showing the inverse of the $H(\omega)$ function for a linear CIDT, and (b) a window function $G(f)$ obtained using equation 5.4.	82
5.5	Normalized inverse chirp waveforms for filter 2, obtained for (a) a linear chirp, (b) a hyperbolic chirp and (c) a mean chirp, using a p-matrix model.	83
5.6	Normalized input chirp waveforms obtained for filter 3, by windowing the transmission response of filter 1 for (a) a linear chirp, (b) a hyperbolic chirp and (c) a mean chirp.	84
5.7	Short pulses $p(t)$, obtained for the three chirp cases, by using filter 1, when the threshold condition is applied on the input chirp waveform.	85
5.8	Short pulses $p(t)$, obtained for the three chirp cases, by using filter 2, when the threshold condition is applied on the input chirp waveform.	85
5.9	Short pulses $p(t)$, obtained for the three chirp cases, by using filter 3 when the threshold condition is applied on the input chirp waveform.	86
5.10	Admittance measurements for the transmission, obtained from the fabricated SAW devices with (a) A linear chirp, (b) A hyperbolic chirp and (c) A mean chirp. Chirp bandwidth is 200 MHz - 400 MHz.	88
5.11	Chirp waveforms obtained for (a) a linear chirp, (b) a hyperbolic chirp and (c) a mean chirp, using the admittance measurements shown in figure 5.10.	88
5.12	Normalized inverse chirp waveforms obtained for (a) a linear chirp, (b) a hyperbolic chirp and (c) a mean chirp, using the admittance measurements shown in figure 5.10.	89
5.13	A schematic of the pulse compression experiment to measure the responses of the fabricated SAW devices.	90
5.14	Short pulses obtained for (a) a linear chirp, (b) a hyperbolic chirp and (c) a mean chirp.	91

5.15 Short pulses obtained for (a) a linear chirp, (b) a hyperbolic chirp and (c) a mean chirp, for $B_0=12.5$ MHz - 142.5 MHz. 92

5.16 (a) Short pulses obtained for a hyperbolic chirp for $B_0 = 12.5$ MHz, 152.5 MHz and (b)The pulse amplitude $|P(\omega)|$ shown in the frequency domain. 93

List of Tables

2.1	Piezoelectric materials used for SAW generation, where <i>SAW</i> is surface acoustic wave, <i>R</i> is Rayleigh wave, <i>PSAW</i> is the pseudo SAW waves and <i>BG</i> is the Bleustein-Gulyaev wave [53].	13
3.1	Reference SAW device specifications.	39
3.2	Specifications of the Lithography process	41
3.3	Design parameters used for the fabricated SAW devices.	42
3.4	The $\frac{h}{\lambda}$ values for different heights (<i>h</i>) used to study the variation in the directivity of the CIDTs	62
4.1	Amplitude measurements of the chirp with different attenuations for SNR estimations.	74
4.2	SNR and displacement calculations using measurement values from Table. 4.1.	75
4.3	Amplitude measurements at the output of every optical component of the interferometer.	75
5.1	A_p values obtained on application of the threshold condition, for the short pulses generated using different types of input chirps described in section 5.1.1	87
5.2	Amplitude gain factor of the short pulse generated using different types of input chirps described in section 5.1.1	87

Title: Generation of short pulses of surface acoustic waves on a piezoelectric material

Keywords: Surface acoustic wave (SAW), Interferometry, Chirped interdigital transducer, Pulse compression

Abstract: Generation of short pulses with surface acoustic waves (SAW) is studied, in analogy with the principle of chirped pulse amplification (CPA) used to produce ultrashort laser pulses. Temporal compression of pulses is generally achieved with dispersive elements. A SAW transducer emitting short SAW pulses is used as a dispersive element in this work. A comparative study of chirped inter digital transducers (CIDTs) using the first order model and the p-matrix model is presented. SAW devices are designed and fabricated using the simulation results and the effect of the varying pitch of the CIDTs on the response is studied. Appearance of band gaps due to internal reflections within the CIDTs and its effect on the directionality of the CIDTs are in particular found and studied. A stabilized time-domain differential optical interferometer is then proposed in order to characterize short pulses, with the surface acoustic wave (SAW) sample placed outside the interferometer. Experiments are conducted with surface acoustic waves excited by a chirped inter-digital transducer on a piezoelectric lithium niobate

substrate having an operational bandwidth covering the 200 MHz – 400 MHz frequency range and producing 10 ns pulses with 36 nm maximum out-of-plane displacement. The interferometric response is compared with a direct electrical measurement obtained with a receiving wide bandwidth inter-digital transducer and good correspondence is observed. The effects of varying the path difference of the interferometer and the measurement position on the surface are discussed. Pulse compression along the chirped inter-digital transducer is observed experimentally. Finally, a comparative study of different filter designs for generating short pulses is presented with an objective to find a design to produce the optimal pulse which is short in width and high in amplitude, for a given dispersive element. The inverse filter is found to be the most efficient as it produces a short pulse with the highest amplitude. To optimize the pulse compression for the fabricated devices, experiments are conducted to find the optimal trade-off curve for each chirp case.

Titre: Génération d'impulsions brèves d'ondes acoustiques de surface sur un matériau piézoélectrique

Mots clés : Ondes acoustiques de surface, Interférométrie, Transducteur interdigité, Compression d'impulsion

Résumé : La génération d'impulsions courtes d'ondes acoustiques de surface est étudiée, en s'inspirant du principe de l'amplification des impulsions chirpées qui est utilisée pour la génération d'impulsions laser ultrabrèves. La compression temporelle des impulsions est généralement réalisée à l'aide d'éléments dispersifs. Dans ce travail, un transducteur à ondes acoustiques de surface pouvant émettre des impulsions brèves est utilisé comme élément dispersif. Une étude comparative des transducteurs à peignes interdigités chirpés est menée avec un modèle du premier ordre et un modèle dit de matrice mixte. Des dispositifs à ondes acoustiques de surface sont conçus et réalisés à partir des résultats de simulation numérique. La façon de distribuer la période dans le transducteur est étudiée. L'apparition de bandes interdites dues aux réflexions internes dans le transducteur chirpé et son effet sur l'émission directionnelle des ondes surface sont en particulier observées et étudiées. Un interféromètre optique différentiel dans le domaine temporel et stabilisé est ensuite proposé afin de caractériser les impulsions brèves. Le transducteur à ondes acoustiques de surface est placé à l'extérieur de l'interféromètre. Des expériences

sont conduites avec un transducteur à peignes interdigités chirpé ayant une bande opérationnelle couvrant la gamme de fréquences 200 MHz – 400 MHz et produisant des impulsions de 10 ns avec un déplacement hors-plan maximal de 36 nm. La réponse interférométrique est comparée à une mesure électrique directe obtenue à l'aide d'un transducteur de réception large bande ; une bonne correspondance des deux mesures est observée. Les influences de la différence de chemin optique dans l'interféromètre et du choix du point d'observation sur la surface sont discutées. La compression de l'impulsion le long du transducteur chirpé est observée expérimentalement. Finalement, une étude comparative de différents filtres de compression temporelle est présentée, dans l'objectif d'obtenir des impulsions optimales à la fois courtes temporellement et de forte intensité, pour un élément dispersif donné. Le filtre inverse est identifié comme le plus efficace et nous permet de produire les impulsions de plus grande amplitude. Afin d'optimiser la compression de l'impulsion pour les dispositifs fabriqués, des expériences sont conduites pour trouver les courbes de compromis optimal dans chaque cas de modulation de la période du transducteur.